Title
High-frequency electrodynamics of cuprate superconductors

Author
Mallozi, Richard P.

Publication Date
1998-10-01

LBNL-42349

ERNEST ORLANDO LAWRENCE
BERKELEY NATIONAL LABORATORY

High-Frequency Electrodynamics of Cuprate Superconductors

Richard P. Mallozzi

Materials Sciences Division

October 1998

Ph.D. Thesis

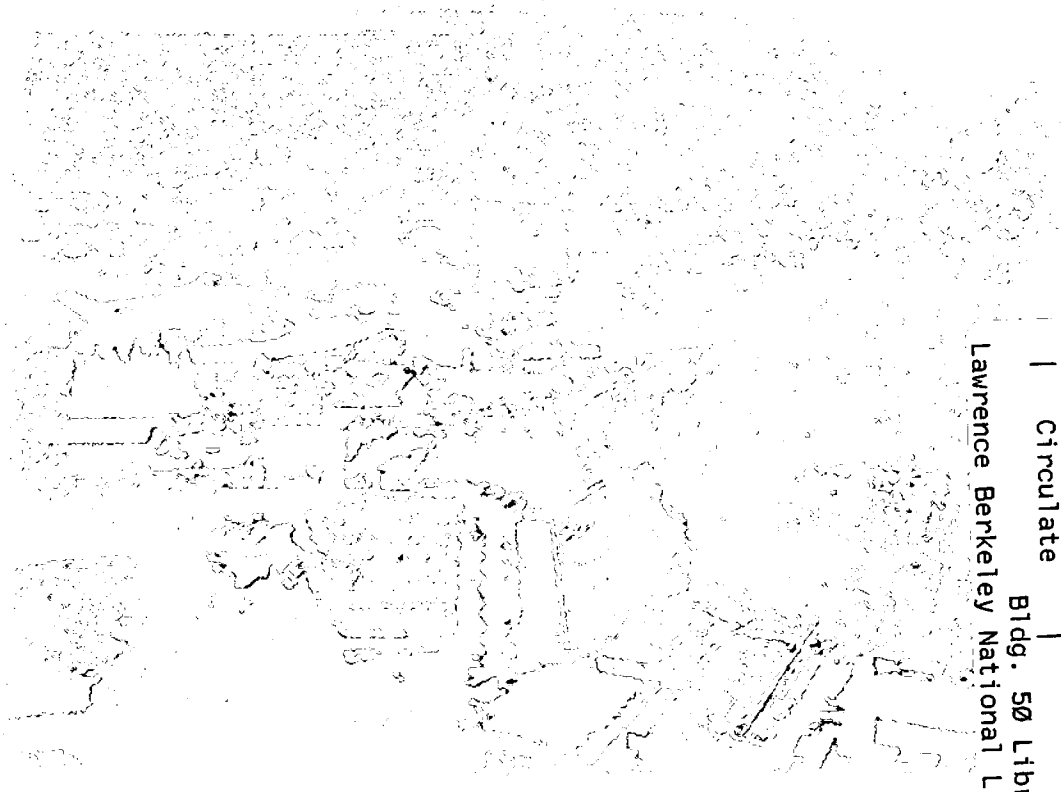

DISCLAIMER

LBNL-42349

High-Frequency Electrodynamics of Cuprate Superconductors

Richard F. Mallozzi
Ph.D. Thesis

Department of Physics
University of California, Berkeley

and

Materials Sciences Division
Ernest Orlando Lawrence Berkeley National Laboratory
University of California
Berkeley, CA 94720

October 1998

This work was supported by the Director, Office of Energy Research, Office of Basic Energy Sciences, Materials Sciences Division, of the U.S. Department of Energy under Contract No. DE-AC03-76SF00098, and National Science Foundation Grant No. FD95-10353.

High-Frequency Electrodynamics of Cuprate Superconductors

by

Richard P. Mallozzi

B.A. (Harvard University) 1991
M.S. (University of California at Berkeley) 1994

A dissertation submitted in partial satisfaction of the
requirements for the degree of
Doctor of Philosophy

in

Physics

in the

GRADUATE DIVISION
of the
UNIVERSITY of CALIFORNIA at BERKELEY

Committee in charge:

Joseph Orenstein, Chair
Daniel Rokhsar
Jeff Bokor

1998

High-Frequency Electrodynamics of Cuprate Superconductors

by

Richard P. Mallozzi

Abstract

High-Frequency Electrodynamics of Cuprate Superconductors

by

Richard P. Mallozzi

Doctor of Philosophy in Physics

University of California at Berkeley

Joseph Orenstein, Chair

Over the last decade a great deal of effort has been devoted to determining the excitation structure of the high-temperature (cuprate) superconductors. Recently, consensus has been established that the energy gap has 'd-wave' rather than 's-wave' symmetry. Comparatively small effort has gone toward explicating the macroscopic consequences of such a gap structure. In this thesis we explore the electrodynamic consequences of the d-wave energy gap.

Using coherent terahertz spectroscopy, we study the conductivity of thin films of the superconductor $Bi_2Sr_2CaCu_2O_8$ (BSCCO) in the frequency range 100-800 GHz, from 5 to 300 Kelvin, and in magnetic fields up to 7 Tesla. We show that the high-frequency vortex dynamics can be quantitatively described by a theory based on electrodynamics inherent to d-wave superconductors. A key experimental result is the observation of $H^{1/2}$ variation of the imaginary part of the conductivity over a wide range of frequency and temperature.

Using only parameters available form zero-field measurements of angle-resolved photoemission and the complex conductivity, the d-wave theory provides a quantitative description of the vortex state of BSCCO.

In addition, we have studied the unusual dissipation of the BSCCO superconductors for various levels of doping. We highlight a number of anomalous properties, particularly a large residual conductivity at low temperatures in the optimally-doped system that is not present in the underdoped system. Finally, we demonstrate a new technique for probing the c-axis properties of thin films and use it to make the first observation of the c-axis plasma resonance in the BSCCO system.

Contents

List of Figures

Acknowledgements

I have many colleagues, friends, and family members to thank for their involvement and support in my graduate school life. First, my advisor Joe Orenstein, from whom I have learned much about, among other things, physics, research, and golf (not necessarily in that order!). When I joined his research group, I had no idea what a fortunate choice that would turn out to be. I would like to thank my parents for 'everything;' I can't do justice to their role with a simple list. My sisters Lisa and Julie , brother Alex, brother-in-law Eddie, (and niece Christina!) provided support and helped me maintain perspective on life here.

I owe gratitude to a number of colleagues and members of the Berkeley physics community. Most of the research I did was made possible by a fruitful collaboration with Jim Eckstein and Ivan Bozovic. I also enjoyed collaborations with Gene Dantsker, Simon Verghese, Edward Budiarto, and Frank Hegmann. Among the Berkeley community, Professor Dan Rokhsar played a large role in my early graduate career and has always made himself available since. Anne Takizawa has been a great friend and an incredible help in handling all of the issues that come up in a graduate student's life. I believe she is one of the greatest assets of the Berkeley physics department. Donna Sakima has efficiently helped me out of many administrateive jams that I seem to get in to.

Friends and coworkers at LBNL have made it a great place to work. Fellow group members John Corson and Gino Segrè are a never-ending fountain of entertaining discussions and antics. They have opened my eyes to many new things and been valuable 'research buddies.' Jen Glass is a close friend and partner in crime. Many cyber aliens have met their deaths at our hands. Peter Kner, Dave Klein, Neil Frommer, and Andy Schumacher

have been key components of the frequent 'slacker vortices' that nucleate around the lab. I have enjoyed and learned from many discussions with Steve Dodge. Former group members Beth Parks, Chandu Karadi, and Steve Spielman have been both valuable resources and fun people to have visit. Ronnie Spitzer and kids Daniel and Jeffrey Orenstein have brought a lot of entertainment to the lab and the driving range.

Friends outside the lab have given me a life beyond physics. My close friend and roommate Ken Clubok has been a major influence and source of countless hours of entertainment. Sarah Herr is a supportive and unwavering friend that has tied our social circle together for many years. She and the rest of the Herr family, Dick, Valerie, and Jane, have been like a family of my own. I have joined them for countless dinners and holidays, and even lived in their house over various periods. Kasra Khazeni is the only person who always seems to see things the way I do (only more so!). We have spent many hours together doing physics, yacking, and trying to find a restaurant where he can still eat. Leon Hsu is going into the Slot. John Rodriguez is going to help put him there. Mitch Koch is a good friend, golf partner, and window to the after-grad-school world. Dave Blackston is a longtime friend (and sometime roommate) with a penchant for moving places a couple of years before I do. Michael Bender and Tamara Voss are witty and brilliant friends that I wish had been in Berkeley all these years. Andrew Schechter, Sarah Kline, Bill Ashmanskas, Kirsten Parkinson, and Geoff Pike have been the steady core of the transplanted Harvard social circle.

Finally, I would like to thank Dr. John and Alice Kraus, with whom I had the good fortune to be neighbors while growing up in Delaware, Ohio. Dr. Kraus has always

been an inspiration to me, partly for his vast scientific achievements, but mostly for the sheer pleasure he takes in practicing and playing with science. I hope my own enthusiasm for the field stays with me the way his has.

This work was supported under NSF Grant No. FD95-10353 and by the Director, Office of Energy Research, Office of Basic Energy Sciences, Materials Sciences Division, of the U.S. Department of Energy under Contract No. DE-AC-03-76SF00098.

Chapter 1

Introduction

The phenomenon of superconductivity has fascinated physicists for almost ninety years. It is perhaps the most dramatic manifestation of quantum physics ever observed. The discovery in the late 1980's [1] of superconducting compounds with transition temperatures above 100 Kelvin brought the field once again to the limelight of solid state physics. These new materials – the cuprate superconductors – have a novel electron pairing mechanism that differs fundamentally from that of conventional superconductors. Although much progress has been made in the last decade, high-temperature superconductivity is still considered by many to be the largest unsolved problem in condensed matter physics.

The excitation spectrum of the cuprate superconductors has a structure not seen in conventional superconductors. It is referred to as a d-wave energy gap; the conventional superconductors have an s-wave gap structure. This unusual spectrum provides both a clue to the underlying mechanism of cuprate superconductivity and a new feature whose consequences are only beginning to be understood. The work in this thesis clarifies the role

of the d-wave gap structure in one of the more fundamental and important properties of superconductors, the electrodynamic response. It divides into two main parts: the response of the vortex state, and the dissipative properties in zero magnetic field.

The response of the vortex state has been widely assumed to be dominated by vortex motion. In chapter 3 we discuss some of the vortex dynamics theories and compare them to our data. We then discuss an alternative model based on the intrinsically nonlinear electrodynamic response predicted for d-wave superconductors and show how this can quantitatively account for the high-frequency response.

In chapter 4 we discuss another manifestation of d-wave electrodynamics, the unusual dissipation in the superconducting state. This fundamental question remains very poorly understood. Though the compounds YBCO and BSCCO have similar energy gap structure, the dissipation in BSCCO shows interesting differences from YBCO in its temperature and carrier concentration dependence. Understanding this issue is central to both practical applications and to a thorough understanding of the electrodynamic response of high-temperature superconductors.

Chapter 5 discusses a new type of measurement we are developing for probing along the c-axis of thin films. We have applied terahertz spectroscopy in a novel geometry in an attempt to observe the plasma resonance along the c-axis. This measurement remains somewhat poorly understood, but has potential to provide information unavailable by other means.

1.1 Optical probes

The experimental technique used in this study is terahertz time-domain spectroscopy: This technique bridges an important gap in the electromagnetic spectrum between microwave and infrared techniques. The frequency range available in our setup is from 100-800 GHz ($3-27$ cm^{-1}, $.4-3.3$ meV, $5-40$ Kelvin). Recent advances in the field have pushed the limits of the technique to above four terahertz [2, 3, 4].

Microwave measurements have been the traditional venue for the study of vortex motion. With photon energies well below the energy gap and the quasiparticle scattering rate, the technique is a powerful probe of the superconducting electrons. Furthermore, the characteristic energy scales associated with vortex motion fall into the microwave regime. Most models of vortex motion have been compared only with microwave measurements.

Infrared measurements, by contrast, use photons with energy that run from about the gap energy ($\sim$ 25meVforcuprates) up to a few electron volts. At these energy scales the probe is comparatively less sensitive to the superconducting electron dynamics, but provides an excellent view of larger-scale shifts in the spectral weight.

Terahertz spectroscopy combines beneficial elements from both techniques, as well as providing a few more. With photon energies smaller than the gap, it is sensitive to the superconducting electron dynamics. At the same time, some characteristic energy scales of the quasiparticles fall into this regime – such as the scattering rate. Thus the spectroscopy views parts of the spectrum where important shifts in the spectral weight occur.

Another important attribute of the terahertz technique is the coherence of the measurement. Unlike conventional infrared techniques, terahertz measurements are sensitive to

both the magnitude and the phase of the electromagnetic radiation. Thus the complete complex response functions can be directly determined without additional assumptions or measurements. This is not true of either microwave or infrared techniques. Conventional FTIR spectroscopy requires Kramers-Kronig analysis to determine the complete response functions, while microwave cavity techniques require measurement of a reference sample that is cut to the same geometrical proportions as the sample under study. They also require an estimate of the penetration length of the superconducting sample for the data analysis. There is, however, a price for the simplicity of the terahertz spectroscopy. The technique is far more sensitive in the transmission geometry than it is in reflection, so the best terahertz measurements are restricted to thin films rather than bulk crystals.

1.2 Electrodynamic Response of Metals and Superconductors

The electrodynamic response of metals can be characterized in terms of the conductivity tensor of the material, defined as the relation between the electric field and the current: $\mathbf{J}(\omega) = \sigma(\omega) \cdot \mathbf{E}(\omega)$. For simplicity in this discussion, we will take σ to be a complex scalar, such as for an isotropic material. The conductivity is complex ($\sigma = \sigma_1 + i\sigma_2$) because $\mathbf{J}$ and $\mathbf{E}$ are not necessarily in phase with each other. The real part, σ_1, is the dissipative response while the imaginary part, σ_2, is the inductive or out-of-phase response.

1.2.1 Conductivity Sum Rule

An extremely powerful concept in understanding the electrodynamic response of materials is the conductivity sum rule. The rule constrains the area under the $\sigma_1(\omega)$ function

to be proportional to the number density of carriers n:

$$\int_0^\infty \sigma_1(\omega)d\omega = \frac{\pi n e^2}{2m}. \tag{1.1}$$

The area under the $\sigma_1(\omega)$ curve is referred to as the *spectral weight*. Thus, regardless of changes in the external condition of the system, such as temperature, pressure, or applied magnetic field, the spectral weight remains constant. For example, when a material goes superconducting, there is a depression of spectral weight at frequencies below the gap energy. This spectral weight appears in a delta-function at $\omega = 0$.

1.2.2 Drude Model

In most metals, the electronic conductivity is well-described with the Drude model. The Drude result comes out of Boltzmann transport theory in the relaxation time approximation, with an energy and momentum-independent scattering time. A simple, classical derivation comes from writing down the equation of motion for an electron in an electric field, with a scattering term that destroys the momentum in a time τ. The result for the conductivity is a Lorentzian:

$$\sigma(\omega) = \frac{ne^2}{m}\frac{\tau}{1 - i\omega\tau}. \tag{1.2}$$

The factor out front is simply the spectral weight without the $\pi/2$. Figure 1.1 shows the real and imaginary parts of the Drude conductivity. The width of the peak in σ_1 is given by $1/\tau$. The imaginary part of σ starts off linear in ω at low frequency ($\omega\tau \ll 1$), and then turns over to a $1/\omega$ dependence at high frequency ($\omega\tau \gg 1$).

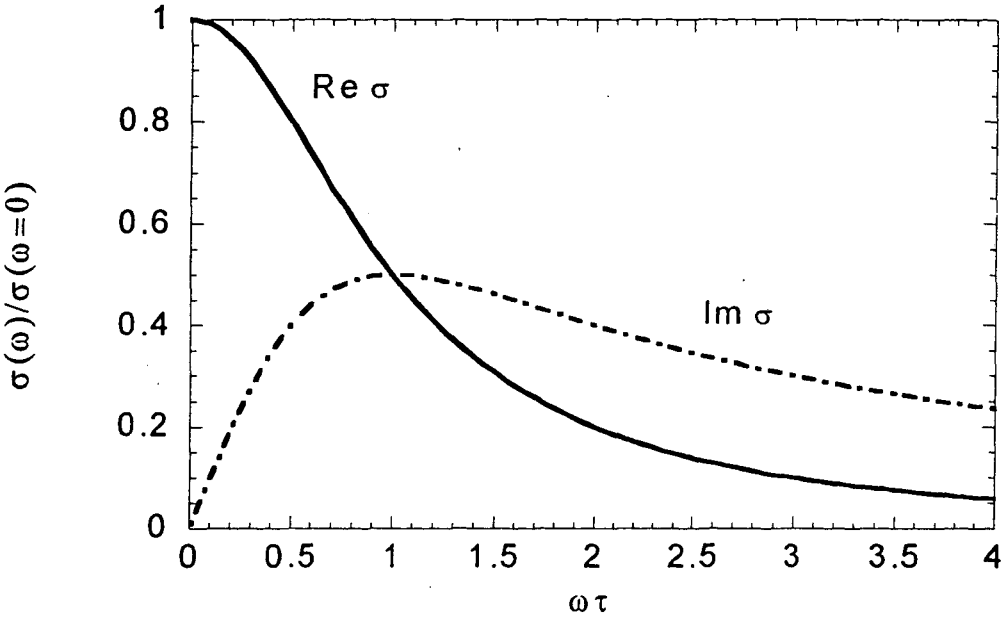

Figure 1.1: Drude conductivity, real and imaginary parts

1.2.3 Conductivity of a Superconductor

The conductivity of a superconductor in the clean limit ($\hbar/\tau < \Delta$) can be described with a *two-fluid* model, in which the transport comes from two channels: the superconducting electrons, and the normal electrons (quasiparticles). The conductivity is then the sum of the contribution from each part: $\sigma = \sigma_s + \sigma_n$, where σ_s is the contribution from the superconducting electrons and σ_n is the contribution from the normal electrons.

The contribution of the normal electrons is typically modeled with a Drude form (eq 1.2) or a generalization of the form [5]. Instead of the *total* spectral weight factor (n/m) out front in eq. 1.2 is the spectral weight that is in the quasiparticle channel n_n/m. Here n_n is the number density of normal electrons. The contribution from the superconducting

electrons (for frequencies much less than the energy gap Δ) is accurately described by a Drude form with $\tau \rightarrow \infty$: $\sigma_s = (n_s e^2/m)[\frac{\pi}{2}\delta(\omega) + i/\omega]$. Hence the complete conductivity is given by

$$\sigma(\omega) = \frac{n_s e^2}{m}[\frac{\pi}{2}\delta(\omega) + i/\omega] + \frac{n_n e^2}{m}\frac{\tau_n}{1 - i\omega\tau_n} \tag{1.3}$$

In the clean limit for a superconductor there is a constraint that $n_s + n_n = n_{total}$, where n_{total} is the total carrier density. This is nothing more than conservation of spectral weight, and a more sophisticated language would not mention carrier densities. The carrier density is not a well-defined physical quantity; the quantity that has experimental relevance is the ratio n/m, which is basically the spectral weight.

A useful result to keep in mind is that for frequencies small compared to the quasiparticle scattering rate $1/\tau_n$, the quasiparticle contribution is mostly real. Well below T_c, when $n_s \ll n_n$, the conductivity is dominated by the superconducting electrons. It is almost entirely imaginary and proportional to $1/\omega$. The coefficient of the $1/\omega$ term gives the spectral weight in the superconducting channel. This property plays a crucial role in much of our analysis.

1.3 *D*-wave superconductivity

Phenomenological description of superconductivity is based on the idea of an *order parameter*[6]. The order parameter $\Psi(r)$ (or $\Psi(k)$ in k space) is a complex scalar which behaves as the wave function of a Cooper pair. The magnitude of Ψ is proportional to the energy gap. Ψ obeys the Ginzburg-Landau equations, which resemble the Schroedinger equation except for some nonlinear terms.

If Ψ has the full symmetry of the underlying lattice, then it is referred to as s-wave. The conventional superconductors are all s-wave. Recent years have brought much debate about the order parameter symmetry in the cuprates; it is now widely agreed that it has d-wave symmetry. The order parameter symmetry places serious constraints on possible mechanisms for the pairing interaction.

Our interest here is in the consequences of d-wave order parameter symmetry. The essential characteristic of a d-wave order parameter is the presence of nodes in the energy gap. The d-wave gap is chacterized with the form $\Delta(\mathrm{k}) = \Delta_0|cos\ k_x - cos\ k_y|$. Figure 1.2 depicts the magnitude of the energy gap around a circular Fermi surface for s-wave and d-wave order parameters. The magnitude of the gap is represented by the distance of the dashed line from the Fermi surface (solid line). The d-wave gap has four points where the gap disappears entirely. Near these nodes, the gap is a linear function of the angle away from the node.

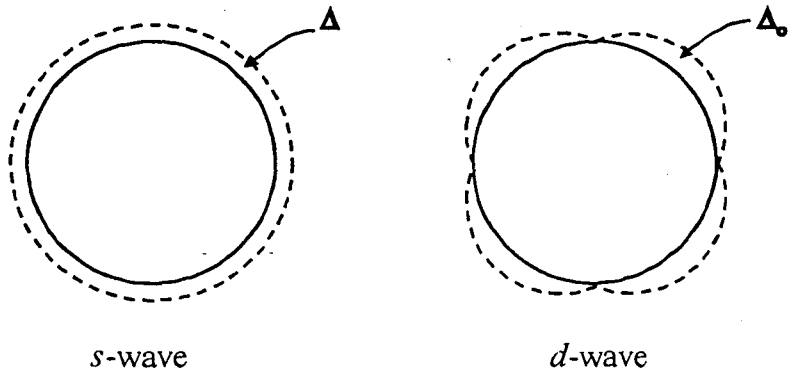

Figure 1.2: Energy gap for s-wave and d-wave superconductors

The presence of the nodes completely changes the density of states of the quasi-

particles, or normal electrons. S-wave superconductors have no quasiparticle states below the gap energy Δ. In a d-wave superconductor there are quasiparticle states near the nodes with arbitrarily low energies, leading to a density of states that is linear in energy [7]. The density of states for an s-wave and d-wave superconductor is shown in figure 1.3, normalized to the normal-state density of states. One of the central themes in this thesis will be understanding the electrodynamic consequences of this d-wave density of states.

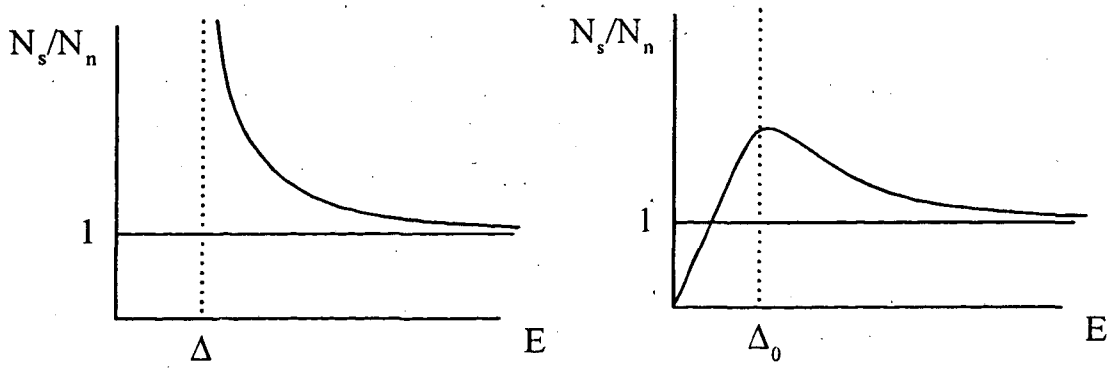

Figure 1.3: Density of states for an s-wave and d-wave superconductor

Chapter 2

Terahertz Spectroscopy

2.1 Overview

Terahertz spectroscopy is a technique for producing and detecting coherent electromagnetic radiation in the far-infrared spectrum. As a spectroscopic tool, it complements conventional techniques, such as Fourier Transform Infrared spectroscopy (FTIR). It covers a part of the spectrum ($\nu = 100 - 1000$ GHz) that is outside the reliable range of FTIR. It also has a number of advantages over FTIR. The terahertz source is extremely bright, reaching effective source temperatures of 3.5 million degrees Kelvin[9]. For comparison, a typical mercury arc lamp used in FTIR spectroscopy has a source temperature of a few thousand degrees. Another advantage is the simplicity of the technique: in a singe measurement lasting one to two minutes, one obtains a broadband measurement of the real and imaginary dielectric functions of a thin film sample, with sufficient signal-to-noise for reliable study of films that transmit only 10^{-4} of the incident energy. Thorough discussions of the technique are available elsewhere[9, 10, 11] so this treatment will emphasize issues

associated with the application of terahertz spectroscopy to thin films.

2.2 Source and Detector

One of the elegant aspects of the terahertz technique is that the processes for generation and detection of the radiation are inverses of each other, done with identical devices. The terahertz source and detector is based on a device called the Auston switch[12]. The Auston switch consists of metallic electrodes deposited on a photoconductive material, such as GaAs or Si. Figure 2.1 is a schematic of such a device. Under 'dark' conditions,

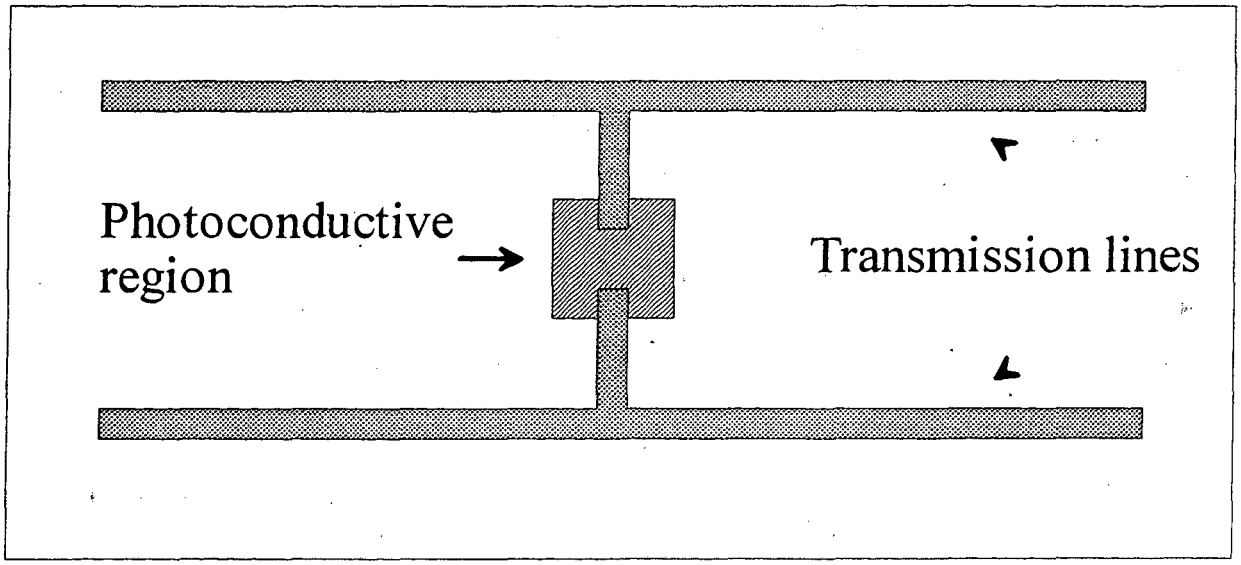

Figure 2.1: Photoconductive switch used as a generating antenna

in which no laser shines on the photoconductive region, the switch is off and very little current can flow. When the photoconductive material is irradiated with a short laser pulse (100 fs), carriers are excited across the energy gap, lowering the resistance by a factor of roughly 10^5 from a typical dark resistivity of 30 MΩ. The switch remains 'on' until the

carriers recombine, which happens over a time scale of the carrier recombination time τ_r. As will be discussed later, it is desirable to have τ_r as short as possible. To achieve this, one introduces defects into the material to capture the carriers. In silicon, these defects are introduced by heavy ion irradiation; in GaAs, the defects are introduced by growing the material at low temperatures. Typical values for the carrier recombination times are from 200-1000 fs.

To operate the Auston switch as a source for free-space radiation, the device is made part of a radiative dipole structure. In figure 2.1 the Auston switch is embedded in a transmission line and a bias voltage is applied across the electrodes. The structure is grown on a sapphire substrate. The 100 fs titanium-sapphire laser pulse strikes the photoconductive material, turning on the switch and leading to a rapidly rising current. The current then decays exponentially with a time constant τ_r, which is generally significantly longer than the rise time of the current. The current *vs.* time profile is depicted in Fig. 2.2.

Since radiation is emitted according to $E \propto \partial J/\partial t$, most of the energy in the terahertz pulse comes from the rising part of the current pattern. Understanding the frequency limitations of these emitters requires a brief look at the phenomenology of the current response.

The current as a function of time is a convolution of the laser intensity, $L(t)$, with a response function of the photoconductor, $S(t)$. The response $S(t)$ is governed by two factors[13, 14]: 1) the carriers, once created by the laser pulse, recombine with time constant τ_r, and 2) the carriers undergo scattering that is independent of the recombinative

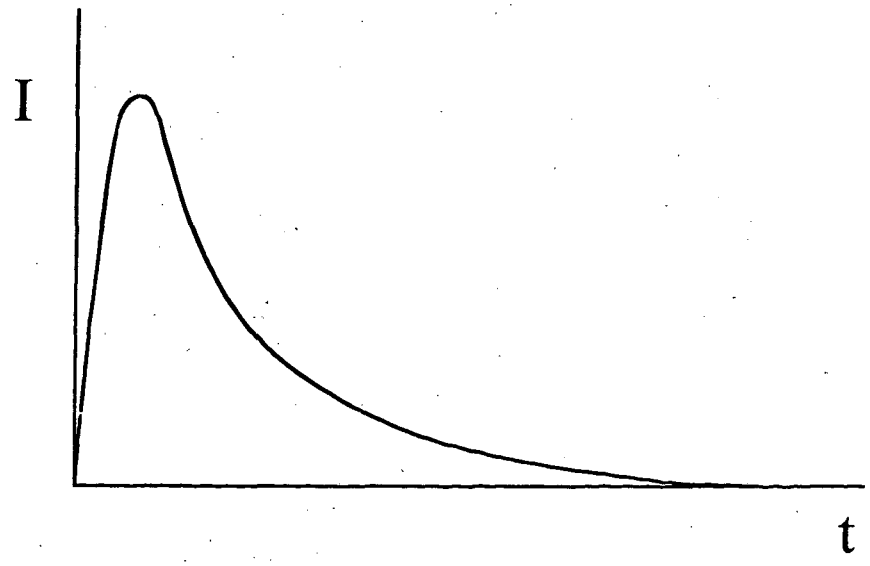

Figure 2.2: Current *vs.* time in the photoconductive generator.

collisions, with time constant τ_c, typically of order 70 fs [2]. The first effect leads to a decay factor e^{-t/τ_r}, while the second effect leads to a 'decaying rise' factor that appears in a Drude response to a step-function field (see appendix A), $(1 - e^{-t/\tau_c})$. Putting these together, we have

$$S(t) = \alpha(1 - R)e\mu\theta(t)(1 - e^{-t/\tau_c})e^{-t/\tau_r}, \tag{2.1}$$

where θ is the unity step function, α is the optical absorption constant, R is the reflectivity of the photoconductive material, and μ is the mobility of the carriers, which for simplicity is assumed to be the same for electrons and holes.

The current across the switch is the convolution of the laser intensity with the response function. Thus

$$J(t) = L(t) \otimes S(t) = \alpha(1 - R)e\mu \int_0^t dt' L(t')(1 - e^{-(t-t')/\tau_c})e^{-(t-t')/\tau_r}. \tag{2.2}$$

We can understand from this equation the limiting factors in the frequency response of the current. Since the current is the convolution of $L(t)$ and $S(t)$, the Fourier transform is the product; hence, the cutoff will come from $S(\omega)$, since that function does not extend to frequencies as high as the laser bandwidth. Looking at the structure of $S(t)$, we can see it is the product of a rising exponential $(1-e^{-(t-t')/\tau_c})$ and a decaying exponential $e^{-(t-t')/\tau_r}$. Hence the Fourier transform $S(\omega)$ is the convolution of the Fourier transform of these two functions. This implies that the frequency roll-off is dominated by the *higher* of the two frequency scales (if they are very different), meaning that $1/\tau_c$ is the limiting frequency scale. This analysis confirms the intuitive statement that the rising edge of the current pulse determines the emission bandwidth. It also shows that the rise time is not limited by the laser pulse once the pulse is significantly shorter than the parameter τ_c.

Thus far we have mentioned only the frequency response of the photocurrent as a factor in the terahertz bandwidth. The other significant component is the geometry of the emitting structure. Since the emitter functions as a dipole antenna it has a resonance when the spacing between the transmission lines is $\lambda/2$, where λ is the wavelength of the emitted terahertz radiation. For dipole antennas much smaller than the wavelength of the emitted radiation, the amplitude of the emitted radiation is proportional to $\omega J(\omega)$. To obtain the broadest bandwidth possible in the terahertz beam, we avoid the resonance by using emitters with line spacing of 30-50 μm. These emitters have sufficient signal to about 1.2 THz, but due to frequency limitations of our photoconductive receivers our bandwidth is limited to about 800 GHz.

If we are interested in working only at lower frequency, such as 100-400 GHz,

we can increase the terahertz power by going to a larger design. For much of the low-frequency work in this thesis, 300 μm dipole antennas were used. These antennas emit THz radiation with amplitude 10-20 times that of the 30 μm designs. The reason for this is twofold. The $\lambda/2$ resonance for these structures is estimated to be about 220 GHz [9] when the index of refraction of the substrate is taken into account. Thus we are operating close to a resonance in the current-radiation coupling. The other reason for the increase in emitted power is simply the length of the structure. The amplitude of emitted radiation is proportional to the length of the current path times the derivative of the current[15], so our 300 μm structures gain a factor of ten in emission amplitude over the 30 μm structures.

As advertised earlier, the terahertz technique benefits from the simplicity of using the same type of device for detecting the radiation as for generating it. To operate the antenna as a receiver rather than a source, we simply run it backwards: instead of applying an external voltage bias across the Auston switch, the incoming terahertz pulse provides the bias. When the switch is activated by the laser pulse, a current flows in proportion to the amplitude of the terahertz electric field. Measurement of this current then yields a quantity proportional to the strength of the field.

Unfortunately, the current measured is not proportional to the amplitude of the electric field in a narrow time window (compared to the terahertz pulse length). The switch samples the electric field from the time the laser pulse activates it until the carriers recombine, which is longer than the entire duration of the incoming terahertz pulse. Writing down the full mathematical expression for the current response, as in eq. 2.2, is considerably more complicated for the receiver because the electric field is now time dependent. We can

simplify matters considerably by applying the intuition that the rising edge of the current response is not key, as in the generator, but rather the decaying tail. This is because the electronics can measure only the total charge transferred across the switch. The signal from the receiver is proportional to the *integral* of the current, while the terahertz output from the generator is proportional to the *derivative* of the current.

Putting these simplified ideas into mathematical form, the signal from the receiver takes the form

$$Q(t_L) = \int J(t)dt \propto \int_{t_L}^{\infty} dt E(t) e^{-(t-t_L)/\tau_r}. \tag{2.3}$$

The quantity Q is the total charge that passes through the Auston switch from a single pulse. It is a convolution of the electric field and the response function of the antenna, evaluated at a time delay t_L between the generating and the detecting laser pulses. By scanning t_L we map out the cross-correlation function between the terahertz electric field and the receiver response function. Fourier transforming $Q(t_L)$ yields the quantity $E(\omega)R(\omega)$, where $R(\omega)$ is the receiver response function in the frequency domain. A time trace and spectrum of such a scan is shown in figure 2.3.

The $1/\tau_r$ roll-off in $R(\omega)$ is the most significant limitation to the high-frequency capabilities of this technique. As will be explained in the following section, we can perform a partial deconvolution of the signal to eliminate $R(\omega)$, though we cannot avoid its bandwidth-limiting effects.

It is important to stress that this technique generates and detects the radiation coherently. In addition to enabling full characterization of material parameters, the coherence of the measurement has advantages for signal-to-noise issues. Whereas detectors sensitive to

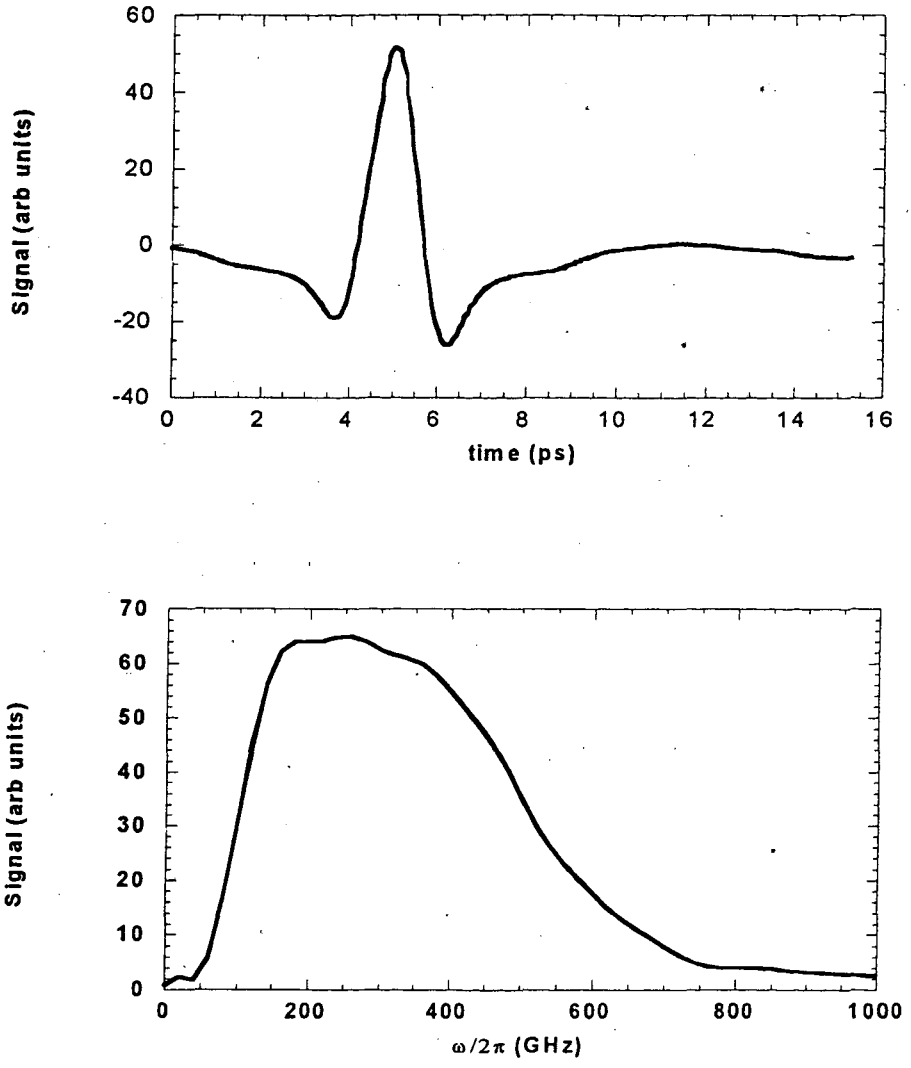

Figure 2.3: Terahertz time trace and spectrum

energy flux (such as bolometers) generate a signal proportional to E^2, the photoconductive detectors produce a signal proportional to E. Thus a film that transmits only 10^{-4} of the incident energy reduces the terahertz signal by only 10^2. This is a bonus to the already high signal-to-noise of 10,000:1 $\sqrt{Hz}$.

2.3 Thin Film Transmission

We turn our attention now to how the terahertz signal is used to extract material parameters from thin films. The information we seek is the complex conductivity of the thin film, $\sigma(\omega)$. Figure 2.4 depicts the experimental procedure for measuring σ. A pulse of terahertz radiation, $E_i(t)$ is incident on the film and substrate. The film reflects some of the radiation and transmits the rest, which we will call $E_t(t)$; absorption is negligible because the film thickness d is much less than the terahertz wavelength λ ($d/\lambda < 10^{-5}$).

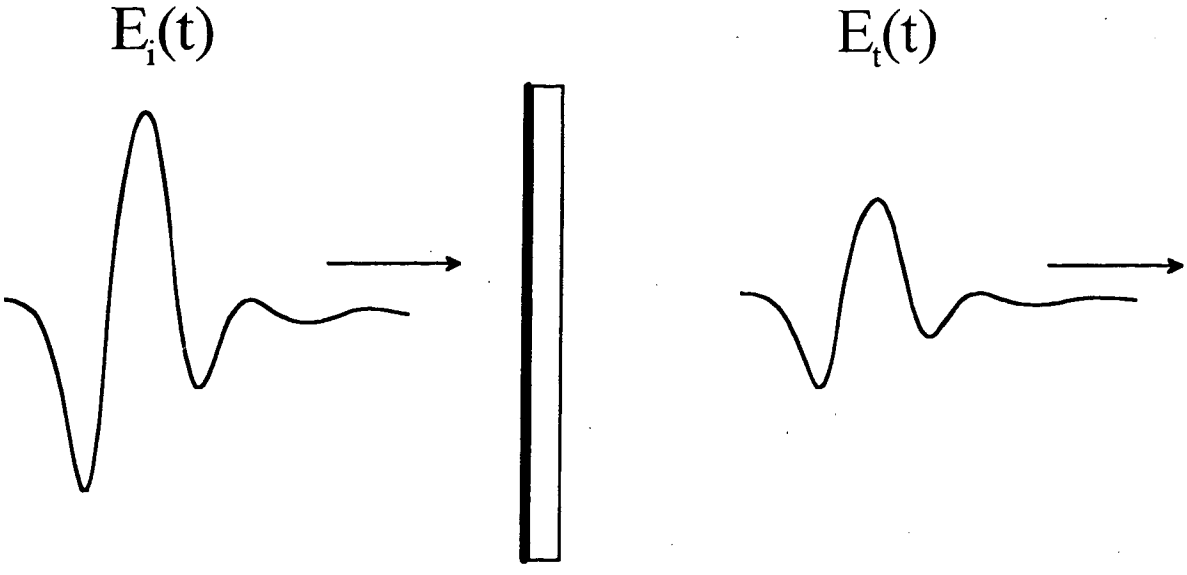

Figure 2.4: Thin-film transmission experiment.

As discussed in the previous section, we can measure the transmitted radiation and Fourier transform to get $E_t(\omega)R(\omega)$. Performing the measurement without the film and substrate provides $E_i(\omega)R(\omega)$. The ratio then removes the response function R and yields the transmission coefficient,

$$t(\omega) \equiv \frac{E_t(\omega)}{E_i(\omega)} = \frac{4ne^{i\Phi}}{(n+1)(n+1+Z_0\sigma(\omega)d)}. \tag{2.4}$$

Here n is the index of refraction of the substrate, $Z_0 = 377\Omega$ is the impedance of free space, and d is the thickness of the film. Φ is a phase factor that depends on the thickness and index of the substrate. A derivation of 2.4 follows from simple application of boundary conditions and is given in reference [11]. Thus we have a very simple relation between the experimentally measured quantity $t(\omega)$ and the material parameter we seek, $\sigma(\omega)$. An additional useful property of equation 2.4 is that for metallic films, the σd term dominates the denominator so that to good approximation $t \propto 1/\sigma$.

Equation 2.4 is valid in the thin-film limit ($d/\lambda \ll 1$) and for conductivities satisfying $\mathrm{Im}(\sigma/\epsilon_0) \gg \omega$. The second condition is so unrestrictive as to be virtually irrelevant for any metal. It should also be noted that this form for the transmission coefficient is applicable when σ is a diagonal tensor; if it is not, one must transform to a diagonal representation before applying eq. 2.4.

2.4 Experimental Apparatus

The experimental apparatus consists of four major parts: the laser and laser optics, the terahertz devices and optics, the cryostat, and the processing electronics. This section is intended to describe these subsystems and give detailed information on using them and dealing with various issues that arise.

Figure 2.5 is a schematic of the terahertz spectrometer. The process begins at the Titanium-sapphire (Ti:sapphire) laser, where $\sim$ 100fs pulses of 800-nm light are generated at a repetition rate of 100 MHz. The beam is split, part going directly to the generator and the rest proceeding to the receiver via an optical delay line (to be discussed later). The

purpose of the delay line is to map out the cross-correlation between the terahertz electric field and the receiver response function, as described in section 2.2.

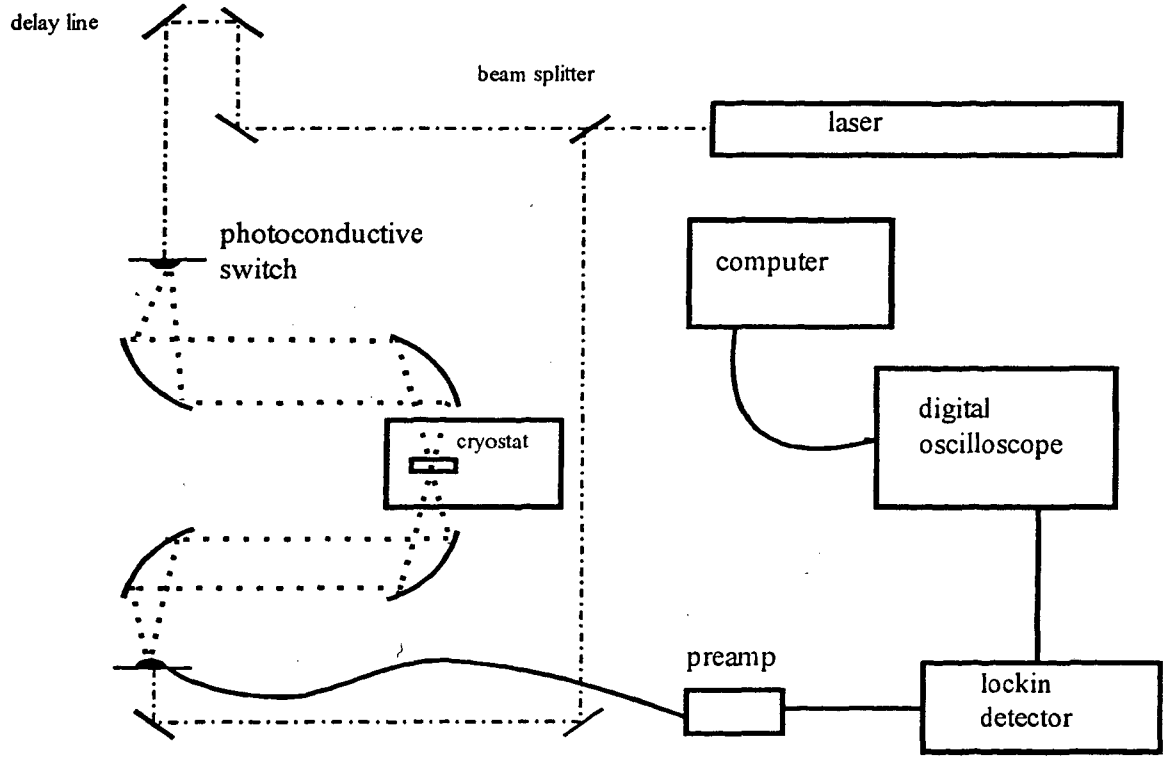

Figure 2.5: Terahertz Spectrometer

The laser pulses strike the generating antenna which emits the terahertz radiation through the substrate and into a hyperhemispherically-shaped silicon lens. The radiation is collimated and refocused with a pair of 90° off-axis parabolic mirrors through the sample, which sits in a cryostat. Another pair of parabolic mirrors recollimates and focuses the transmitted radiation onto the receiving antenna, which converts the terahertz signal to a current that is amplified and processed by the computer.

2.4.1 Laser and laser optics

The laser used for most of the work reported in this thesis was a Lexel model 480 Ti:sapphire laser, passively mode-locked with pulses of 130 fs duration. It was pumped with a Spectra Physics model 2040a Argon-ion laser at 432 nm. The more recent work (zero-field studies of σ_1) was done with a model TS Ti:sapphire laser kit from Kapteyn-Murnane Laboratories pumped by a Spectra Physics Millenium diode-pumped Nd:Yag laser at 514 nm. The pulses are nominally 100 fs in length, though with pulse compression this laser is capable of producing pulses as short as 20 fs. The Kapteyn-Murnane laser reliably produces mode-locked pulses at 450-650 mW.

The mirrors used to guide the Ti:sapphire pulses are dielectric coated for high reflectivity near 800 nm. The high reflectivity is important if laser power is not abundant, as the laser strikes 10-15 surfaces before it reaches the antennas. The dielectric coating, however, has the side effect of broadening the pulse. The amount of broadening depends upon the initial length of the Ti:sapphire pulse. These effects could be partially compensated for with a prism pair to introduce negative group velocity dispersion, though the mirrors also introduce higher-order dispersion that cannot be compensated. We have not explored in our experiments whether the length of the pulse is a limiting factor in the terahertz bandwidth; this is an issue worth attention if pushing for higher frequencies.

Some of the more current generator designs, such as those from the Lincoln Laboratory group [16], require very little laser power (15-30 mW). In addition, these devices are made with more carefully engineered materials that likely have shorter scattering times, making the laser pulse length a stronger limiting factor. In such cases it would be worth-

while to switch to metallic mirrors rather than dielectric ones. The advantage of metallic mirrors is very little dispersion. The disadvantage is a lower reflectivity, and a shorter lifespan. However, since laser power is abundant, the lower reflectivity is not a factor.

The other element in the laser optics is the scanning delay line. We employ both a rapid-scan system, which can run up to 20 Hz, and a slow-scan system. The signal-processing issues associated with these methods will be discussed in section 2.5. Both delay systems introduce the extra path length by routing the beam into a movable corner reflector. The rapid scan system is a Clarke Instruments ODL-150; the slow-scan system is a standard 1 μm stepping motor from Klinger, with a total travel of about two inches. Because of the short travel distances on the delay lines, the optical path length in the generator arm and the receiver arm must be made approximately equal with the permanent mirror setup. A long piece of string and an infrared viewer usually suffice to attain the necessary accuracy.

Alignment of the scanners has to be done carefully. It is important that the laser beam enter the scanner parallel to the axis of travel. Otherwise, as the scanner moves, the beam will translate perpendicularly to the axis of travel. The alignment is achieved by projecting the outgoing beam to a wall as far away as possible (8-10 meters) and watching for beam movement as the delay is scanned. With the rapid scan system, achieving excellent alignment is somewhat difficult. This is a likely reason for slight differences in the spectra between the slow-scan and the rapid scan system. Another measure taken to mitigate effects of beam movement is to place the rapid-scan delay line in the receiver arm of the laser path. The receiver should be less sensitive to beam movement than the generator.

2.4.2 Terahertz devices and optics

In section 2.2 we discussed the theory of the source and the detector. Here we discuss the optical components associated with the terahertz beam. Considerable attention will be given to alignment of the system. The components of the terahertz optics consist of the source and detector, the hyperhemispherical lenses, the parabolic mirrors, and the sample mount. The hyperhemispherical lenses have been discussed extensively elsewhere [9, 10, 11] and so will not be discussed here beyond explaining that they help collect and collimate the terahertz beam.

We begin the discussion with the alignment of the laser beam onto the antennas. The procedure is the same for both emitter and receiver. The goal is to focus the laser beam to the spot which maximizes the photocarrier response. To do this, the antenna is made part of a *dc* circuit shown in figure 2.6. The purpose of the circuit is to apply a *dc* bias across the device and measure the current. The laser passes through a microscope objective (magnification 5x) that is on an XYZ translation stage. As the beam becomes better-aligned with the antenna, the impedance of the device drops and the current increases. The current is monitored by measuring the voltage across the 100 kΩ resistor.

The 5MΩ variable resistor in parallel with the antenna acts as a safety switch to prevent voltage surges from damaging the antenna. In the 'off' position, the antenna is shorted; in the 'on' position, the antenna is in parallel with 5 MΩ. This same switch is used to turn the generating antenna on and off when in use by the spectrometer.

The amount of laser power used on the generator depends strongly on the type of antenna. The SOS antennas made in our group generally use 100-150 mW of power. The

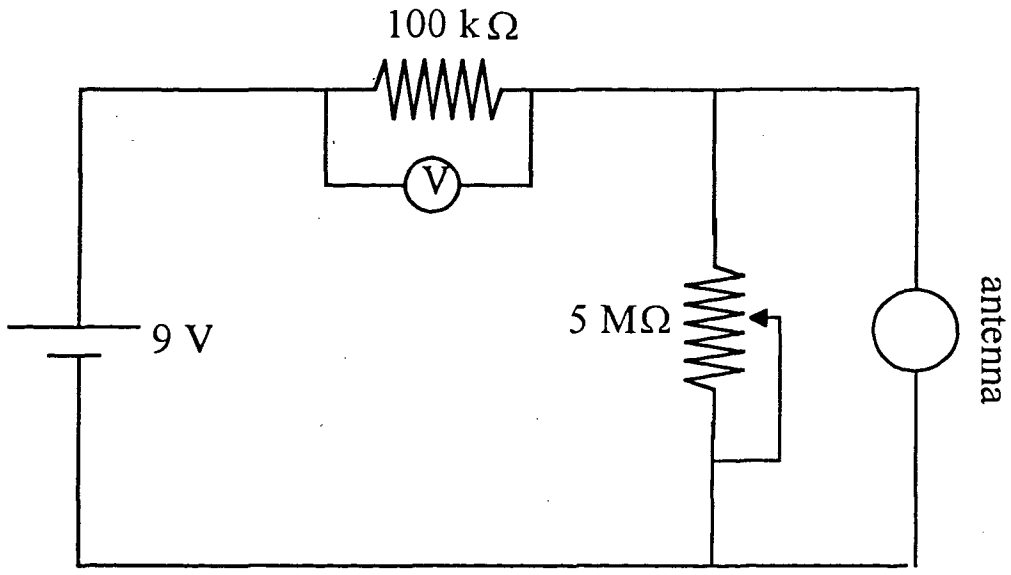

Figure 2.6: Circuit used for aligning the laser onto the antennas

smaller L-T GaAs devices from Lincoln Laboratories [16] use only 10-25 mW. In either case, it is important to find the saturation regime–the point at which increased laser power has little effect on the terahertz output. This sharply reduces the transfer of laser noise into the terahertz signal.

We turn next to the propagation of the terahertz beam. Interesting experimental issues arise in the system because the wavelength of the terahertz radiation is not much smaller than the optical components (300 GHz = 1 mm). Diffraction effects become significant and must be handled carefully.

The beam is emitted through the hyperhemispherical lenses as if from a point-like source[9]. When refocused at the sample location, it propagates in a zeroth order Gaussian mode with e^{-2} diameter (on amplitude) of $(4\sqrt{2}\lambda/\pi)(f/\#)$, where $(f/\#)$ is the f-number of the beam. Our beam has $f/\#$ of 2, so for our low-end frequency of 100 GHz, the beam

diameter is slightly less than 1 cm.

It is, in fact, the diffraction-limited focus size that determines the low-frequency limit of our experiments. The films we study cannot be made reliably much larger than 13 cm across. We mount the films on a slab of metal to block radiation from going around; the film sits over a circular aperture with diameter 11 cm. If the beam encounters the metallic aperture, the aperture will have an effect on the transmission of the radiation. The primary influence is on the phase of the transmission rather than the magnitude.

If the aperture effects were independent of the film transmission, there would be hope of dividing them out with proper reference measurements. Unfortunately, the transmission properties of the aperture and film seem to involve coupling between them. We have not established any method of taking the aperture effects into account other than ignoring the low-frequency data where the aperture effects are present.

We establish the lower frequency limit of good data with the following procedure. We measure the radiation transmitted through the superconductor in the normal state and in the superconducting state. As a function of frequency, we look at the relative phase of these transmissions, $\phi(\text{normal}) - \phi(\text{superconducting})$, which should be very close to $\pi/2$ (since $t \propto 1/\sigma$). At lower frequencies the aperture effect kicks in and causes this phase difference to deviate rapidly from $\pi/2$. This deviation marks the point at which the phase information has become corrupted by the aperture. Any aperture effects which get divided out by this procedure and do not manifest themselves here will also be divided out in the data analysis, to be discussed later.

It is clear that in order to minimize the aperture influence, it must be accurately

placed in the focus of the beam. Since there is no way to visualize the terahertz beam, the task is nontrivial. In principle it can be completely accomplished with knife-edge scans of the beam at the focal point. This characterizes the shape and location of the beam so that with the help of some pointing lasers, the aperture can be placed in the correct position. However, it is preferable to have some scheme for verifying the procedure; the 'verification' scheme is equally good for locating the focus in the first place. It is still helpful to use the knife-edge scan to locate the focus position along the path of the beam; this reduces the degrees of freedom by one for the later procedure.

The following method works well with or without the sample in place. With the rapid-scan delay line running, the aperture is moved approximately into place by observing the transmitted signal on the oscilloscope. One can get reasonably close to the proper position by adjusting the aperture position so that the magnitude of the signal is maximized. At this point, we assume that the position along the beam propagation direction is correct from the knife-edge scan. To place the aperture more precisely, we scan the aperture position in small increments, taking spectra along the way. We compare the relative phase of these spectra by dividing them all by a reference spectrum. By looking at the relative phase as a function of frequency, for various aperture positions, we can see when the aperture effects are minimum. Performing this procedure in both transverse directions locates the center of the focus completely.

Once the correct aperture position has been established, it is important to be able to place the aperture back in the same location throughout the experiment. Even if the cryostat is not being moved to perform reference air measurements, the aperture will

move about 2-2.5 mm upon cooling the cryostat from room temperature to 5 Kelvin due to thermal contraction of the cryostat arm. This effect is present only in the zero-field cryostat because it is operates with a coldfinger rather than by gas exchange cooling.

The solution to this problem is to monitor the position of the aperture with a pointing laser. The general idea is to pass a laser beam across an obstruction on the sample mount, so that half of the beam is blocked. The unobstructed half passes to a photodetector; as the sample mount moves from thermal contraction, the amount of light passing over the obstruction changes and is read out from the photodetector.

The amount of light striking the photodetector changes if the output of the laser changes, so a reference beam is used. See figure 2.7. The laser is first split; half passes over the sample mount as described, while the other half goes to another photodetector wired up in a subtraction circuit with the first one. The output from the photodiode pair is the difference in laser power striking them. The reference beam also passes through a polarizer which is used for equalizing the intensities in the two beams.

Small changes in sample position lead to big swings in the output of the photodiode pair. We are able to detect changes in the cryostat position as small as a few microns. It also allows us to pull the cryostat out for reference measurements, and place it back in with micron precision.

The final element to discuss in the terahertz optical components is the parabolic mirrors. This is often considered a difficult or tricky operation, but with a small visible light source this can be done very accurately in an hour or two. The light source we use is a tungsten filament that has a 1 mm aperture placed directly in front of the filament,

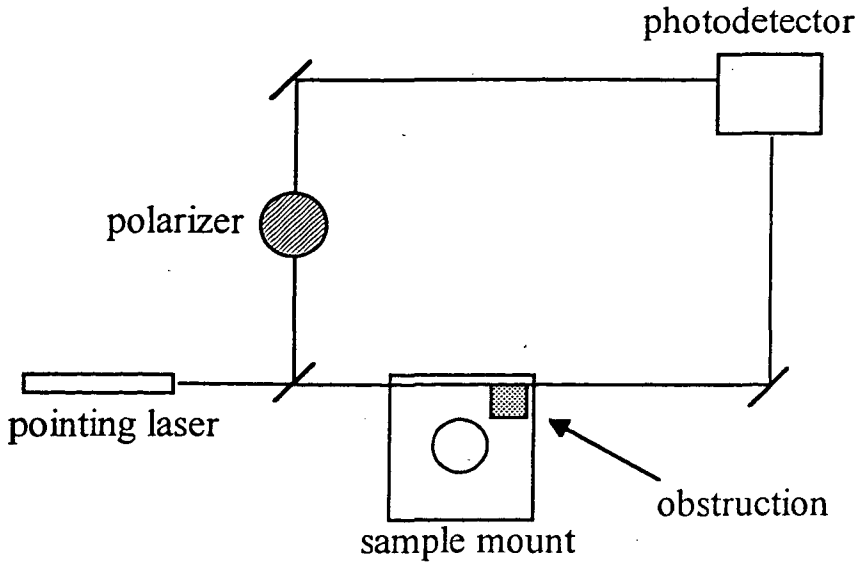

Figure 2.7: Positioning setup for the aperture

inside the bulb. It is referred to as a 'point source.' We will refer to the parabolic mirrors by number, with the first one being closest to the generator and the last one being closest to the receiver.

The first step is to adjust the point source to the height of the cryostat sample chamber. Height comparisons throughout this procedure are done with the beam of a leveled pointing laser. The point source is placed in the location where the generator is to go and clamped down. Using the light from the point source, the first parabola is brought into place and moved around until a collimated beam is produced at the right height. The mirrors are not perfectly shaped for optical imaging, so the visible beam should be observed as far away as possible without excessive distortion (usually 1-3 meters). One can judge the collimation of the beam by checking the diameter close to the mirror and far away. Another convenient scheme is to place an object with holes in it in the path of the collimated beam

and observe the image formed downstream.

The second mirror is then placed in the path of the collimated beam and adjusted until a good focus is formed. To check the focus, a piece of paper is run back and forth while studying the shape. The focus should be very tight, round, and free of astigmatism as the paper is run through. Astigmatism shows up as an elliptical shape on either side of the focus, with the elongated direction rotated by 90° on either side of the focus. The height of the focus is not critical at this stage, as the parabola can be freely rotated about the axis of incoming light once a nice focus is attained.

Once the first two mirrors are in place, the last two are handled identically to the first two. A collimated beam is formed with the third parabola (at the proper height), a good focus formed with the fourth. The receiver can then be put in place with the visible beam. The point source is then replaced with the generator, using crossed pointing lasers to mark the location. Once the terahertz signal is found, fine adjustments can be made to parabolas 3 and 4 to optimize the signal. Usually only the last parabola needs adjustment.

We have found that there is small leakage of low-frequency signal around the parabolic mirrors making to the receiver. It can be seen in the time trace as a small background 'noise' present for all time delays. On the spectra, it leads to a peak, about 10% the size of the main peak, at about 60 GHz. Since this signal does not go through the sample, it is important to reduce it as much as possible. This is achieved with walls of absorptive material (ecosorb) between the optics, with holes cut for the beam.

2.4.3 Processing Electronics

The electronics system consists of the generator driving voltage, two stages of amplification, signal averaging, and a computer. In earlier discussions of the generator, the bias field was discussed as if it were a *dc* bias. In fact most other terahertz laboratories do use a *dc* bias; we choose to bias the generator with a 8-12 kHz sinusoidal voltage. Compared to all other time scales in the system, this is essentially *dc* . The primary advantages of using an *ac* bias is that one can operate at higher frequencies than a chopper, reducing detector noise. Furthermore, a chopper throws away half the signal; this method does not.

The bias voltage comes from the lockin-detector (Stanford Research Systems model 850) and is amplified with a 10X transformer, so that the rms voltage bias on the generator (either type) is about 20 volts. If one has an ample supply of antennas, this voltage can be increased to get more signal, but the antenna lifetime will be reduced. At 20 volts the antenna shows no signs of wearing out.

The choice of bias frequency is made as high as possible without going into the roll-off regime of the preamplifier. The Ithaco model 564 preamplifier, hooked up directly to the receiving antenna, amplifies the current by 10^7 Volts/Amp. It has a frequency roll-off at 12 kHz. We choose the generator bias frequency to maximize signal-to-noise; typically this is about 8 kHz, depending on what other equipment is being operated in the building. The laboratory next door seems to generate noise at multiples of 5 kHz, so those frequencies are avoided.

The output from the preamplifier is fed into the lockin detector, which is tuned to the driving frequency of the generator. The output from the lockin goes to a signal-

averaging oscilloscope and to a computer. The lockin signal is a voltage proportional to the autocorrelation of the terahertz electric field and the receiver response function, at a particular time delay. The oscilloscope, a Lecroy 9310M, also receives a voltage from the rapid-scanning delay line that marks the position of the scanning mirror. Hence the signal can be viewed on the screen as a function of time, updated at about 8 Hz. The oscilloscope also performs a running average of the time traces; generally we average for about 1-2 minutes in an experiment. If running the slow-scan system, the computer records the position of the scanning mirror and accepts the lockin signal to record the time trace without need of the oscilloscope.

2.4.4 Cryogenics

We employ two types of cryostats in our measurements. For zero-magnetic-field measurements, we use a coldfinger cryostat. It operates with a continuous flow of liquid helium and is capable of bringing the sample temperature to 5 Kelvin. The window material is 1.5-mil thick mylar. This cryostat is used because it is much smaller and simpler than the magnet cryostat, leading to superior optics (smaller f/#) and more flexible operation. The disadvantage is that the sample is cooled with thermal contact rather than by an exchange gas, which complicates sample mounting issues. For example, because the substrate is not always a satisfactory heat conductor, we must sacrifice the edges of the films by mounting the samples film-side-down for good thermal contact.

For measurements in a magnetic field we use an Oxford Instruments SM4-7.5T magnet cryostat. The cryostat has a field range from -7.5 Tesla to 7.5 Tesla, and a temperature range from 2.2 to 300+ Kelvin. The sample temperature is controlled with helium

exchange gas and a heater. This cryostat is substantially larger than the coldfinger cryostat and requires optics with f/# of approximately 5, compared to 2 for the coldfinger.

Achieving temperatures down to 10 Kelvin is routine for this system; to get below 5 Kelvin requires a few conditions to be met. First is the use of quartz windows on the radiation shield to reduce penetration of thermal background radiation into the sample chamber. These should be mounted with good thermal contact to the radiation shield. Quartz does begin to absorb terahertz radiation at the higher end of our frequency range; if the frequency capabilities were extended to beyond 1.5 THz, a new window material may need to be found.

The second condition is having good thermal contact with the 1K pot. The 1K pot is a bath of helium with a region above it that can be pumped upon. The boiling off of the gas cools the liquid to 1 Kelvin. Thermal contact with the sample is maintained with helium exchange gas in the sample chamber. The desired pressure to achieve this is a few mbar[17]. It is important that the sorb (a piece of charcoal in the sample chamber) not remove this exchange gas. The cryostat is equipped with a needle valve to isolate the sorb from the sample chamber. If the needle valve is not functioning properly, the sorb can be persuaded not to absorb in a couple of ways. Heating it to 30-50 Kelvin prevents the absorption; however then the sorb is also in thermal contact with the sample and heats it. The ideal situation is to have the sorb saturated with helium, at low temperature. This way pressure can be maintained without thermal contact to a warm object.

2.5 Noise and signal averaging

The primary source of noise in the system is in the generation of the terahertz pulses. The noise in the detector is close to the theoretical Johnson noise limit, and the preamplifier adds a negligible amount to this. Let us justify this claim with a quick calculation. With no terahertz signal incident on the detector, the noise measured after the preamplifier corresponds to 100 fA/$\sqrt{Hz}$ noise in the detector. The average resistance of the detector is about 20 MΩ, which has a corresponding Johnson noise of 80 fA/$\sqrt{Hz}$. Clearly the amplifier is not adding much to the noise in the detector.

With the terahertz radiation incident on the detector, the noise at the peak signal is 20 pA/$\sqrt{Hz}$, a factor of 200 larger than the noise with no terahertz signal. This implies that the noise originates from the terahertz signal rather than the detector or amplifier. It is likely that this noise is caused by pointing instability of the laser onto the generator. With the generator operating in the saturation regime (see sec. 2.4.2) laser amplitude fluctuations should not lead to terahertz noise. However if the laser spot moves by even a micron or so, significant fluctuations in the terahertz output will result. With over 5 meters of path length between the laser and the generator, it would take very little disturbance to give such a fluctuation. Another possible source of pointing instability is air currents in the room disturbing the laser pulse. This could be helped by enclosing the beam. In what follows we will use the term 'laser noise' for pointing as well as amplitude fluctuations.

The signal averaging for the system is done in two ways. In one form, the delay is scanned slowly (1-2 minutes), and only once, while the lockin amplifier performs the averaging. The bandwidth for averaging is determined by the speed of the scan and the

bandwidth of the terahertz signal. This method has the drawback of picking up the low-frequency laser noise, which is of 1/f color. An alternative averaging method that reduces this problem is a rapid scan system, using the Clarke Instruments rapid scanning optical delay line. The delay is scanned at about 8 Hz while the signal is co-added on the digital oscilloscope. A mathematical analysis of this technique is given in reference 11. The upshot is that the laser noise sampled is not a narrow peak around *dc* , but rather a series of narrow peaks every 8 Hz up to the averaging bandwidth of the lockin. In this method the lockin averages over a much wider bandwidth than in the slow-scan method. The total bandwidth sampled is the same in either method, but the rapid-scan system samples at higher frequencies, reducing 1/f noise.

2.6 Time-of-flight measurements

We take a slight digression here to discuss a different type of measurement that is very sensitive to frequency-independent changes in the optical path length of the terahertz beam. Such changes shift the pulse in time without reshaping it. Examples include changes in the thickness or index of a substrate, or small variations in the scattering time of a Drude metal. If this is the only information sought, there is a very elegant way to extract it with high precision.

First let us demonstrate that small changes in the Drude scattering time lead to such a time shift. From equation 2.4 the transmission coefficient $t \equiv E_t/E_i$ for a metallic film with $Z_0\sigma d \gg n$ is approximately $t \sim 1/\sigma$. Thus the transmitted field is given by

$$E_t(t) = \int d\omega E_i(\omega) e^{i\omega t} \frac{1}{\sigma(\omega)} \sim \int d\omega E_i(\omega) e^{i\omega t}(1 - i\omega\tau). \tag{2.5}$$

In our frequency range $\omega\tau \ll 1$ for any metal, so $(1 - i\omega\tau) \approx e^{-i\omega\tau}$. Thus we can simplify our expression:

$$E_t \sim \int d\omega E_i(\omega) e^{i\omega(t-\tau)} = E(t-\tau). \tag{2.6}$$

We see that changes in the scattering time will lead to shifts in the time trace of the transmitted radiation.

To detect such a shift, we could take spectra and look for changes in the phase of the transmission coefficient. This is an acceptable way to do it, but there is an alternative method that is faster and more sensitive. We refer to it as the 'time-of-flight' measurement. Rather than scanning the entire time delay, we set the delay to the null crossing of the time trace. See figure 2.8. When the pulse shifts in time, the null moves off our time delay and we get a large error signal. We change the delay to get back to the null and record the shift. This method allows us to resolve changes of a few femtoseconds in τ.

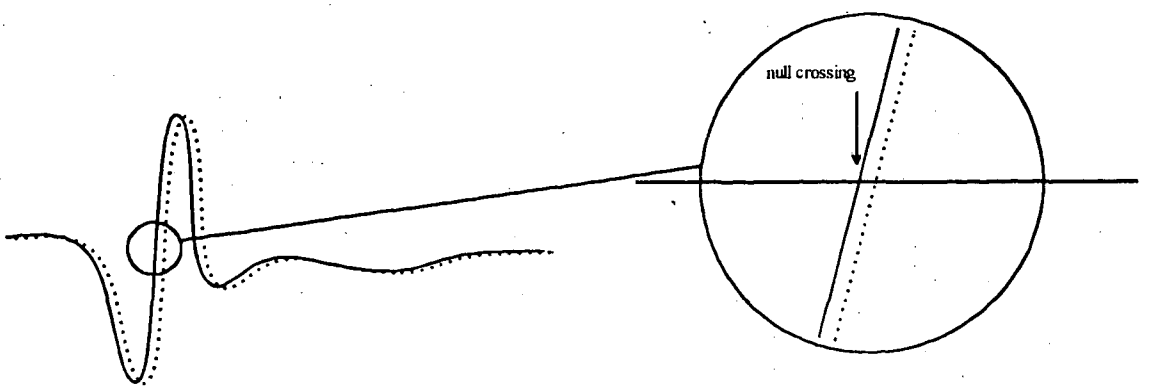

Figure 2.8: Null-crossing experiment

2.7 Data Analysis

One of the useful applications of the time-of-flight measurement described in the previous section is characterizing the substrate behavior. The analysis of the data with equation 2.4 requires a precise determination of the phase factor Φ. We generally do this by normalizing the transmission at each temperature to the transmission at a reference temperature, canceling out most of the contributions to Φ. However, the substrate changes thickness and index as it is cooled, leading to additional change in Φ that must be accounted for. The total phase change due to substrate effects is larger than any phase change caused by the sample, except the superconducting transition.

We use the time-of-flight measurement to accurately characterize the behavior of the substrate, separate from the film. Once we know $\Delta\Phi(T)$ then the conductivity can be solved for from equation 2.4. Studies of σ_1 at low-temperature in a superconducting film require very precise phase characterization of the substrate. It is only with the advances made in correcting for the substrate phase contribution that we have obtained accurate σ_1 data in the superconducting state.

Often we are unable to measure the same substrate that a film is grown upon. In this case we compare the phase change of the film and substrate to the phase change of a similar substrate in the high-temperature regime (240-300 K) and extrapolate. Slight variations in thickness do not permit us to simply use the phase change from the reference substrate. There are two options. One is to try to measure precisely the thickness of each substrate, and use that information for the phase correction. This method suffers from uncertainty in the precision of the thickness measurement. We do not know how far off this

might be. The other method is to assume the change in the phase of the film and substrate from 240-300K comes entirely from the substrate. This introduces a slight error into the measurement because changes in the scattering time of the film also lead to phase changes. However, this is a more controlled error. We have a reasonable upper bound to the error introduced by this technique.

Ideally, we would simultaneously measure the transmission of our samples and a reference substrate from the same wafer. This will be done in our next generation cryostat. Such a procedure will improve the accuracy and simplicity of the measurement.

Chapter 3

Superconducting Response in a Magnetic Field

3.1 Background

Application of a strong magnetic field to a superconductor can generate large changes in the electrodynamic response functions $\sigma(\omega)$ or $\rho(\omega)$. Understanding this response has both fundamental and practical importance. It would be difficult to claim a solid understanding of superconductivity without explaining behavior in a field. At the same time, the nonlinear response to magnetic fields may be closely related to nonlinearities plaguing radio-frequency applications of superconducting films [20].

It is clear that understanding the response to strong a static field means understanding the phenomenology of the vortex state. How do the presence and behavior of vortices manifest themselves in σ or ρ? There are two major ways. The one most often

considered is the change in the condensate response due to vortex *motion.* The other contribution is the effect of vortices on the *quasiparticle* response. This latter contribution itself has two mechanisms: changing the density of low-lying states, and changing the transport of thermally-activated quasiparticles that existed before application of the field. This last mechanism is a topic that is beginning to be explored, with intriguing results [22]. It is fundamentally different from the previous two in that it does not change the spectral weight of the condensate.

In the conventional s-wave superconductors it is the vortex dynamics that appears to dominate the magnetoconductivity [6]. In the cuprate superconductors, there is reason to believe that this may not be the case: The d-wave order parameter gives rise to low-lying quasiparticle states that may increase the importance of quasiparticle mechanisms.

Historically, vortex motion has been probed with microwave radiation. Pinned vortices are invisible to *dc* transport, but fluctuations around pinning sites can be detected in the microwave regime. Like terahertz spectroscopy, microwave measurements are coherent and so provide information about both real and imaginary parts of σ. There is widespread consensus among these experiments that characteristic vortex relaxation times in YBCO vary from 10-100 GHz.

As terahertz studies began on YBCO, it was expected that vortex motion would be invisible to such high frequencies (100-800 GHz). The intent was to study quasiparticle dynamics in a magnetic field. Instead, Parks *et al.* [23] made the surprising observation that the vortex response has the same character at higher frequencies as it does at microwave frequencies. Large changes in σ_2 were observed, signaling reduction in condensate

spectral weight at frequencies far beyond the characteristic relaxation rates. This observation revealed a gaping inconsistency in the vortex dynamics description of electrodynamic response.

It was suggested by Parks *et al.* that perhaps the *d*-wave nature of the energy gap increased the importance of quasiparticle mechanisms in the vortex response. Groundbreaking theoretical work had been done recently predicting nonlinear electrodynamics for *d*-wave superconductors [7]. The central idea behind this prediction is changes in the low-lying quasiparticle density of states (QPDOS) due to superfluid currents. We will refer to this mechanism by QPDOS, in contrast with vortex dynamics. While the data on YBCO suggested QPDOS effects, a major inconsistency stood in the way. The *d*-wave theory predictions lead to a response nonlinear in field strength, while the observed response was highly linear [23].

It was at this point that we began our studies on $Bi_2Sr_2CaCu_2O_8$(BSCCO). Pinning is less effective in BSCCO than in YBCO because of the two-dimensional nature of the vortices. In addition, BSCCO permits study of both the vortex solid and the vortex liquid phases over a wide range of temperatures. Our goal is to clarify the role of *d*-wave electrodynamics *vs.* vortex dynamics in determining the electrodynamic response of the mixed state. We will begin the discussion with a look at the vortex dynamics picture and a comparison to our data on BSCCO.

3.2 Vortex dynamical response

As discussed in section 1.2.3 the condensate contribution to σ_1 is a δ-function at $\omega = 0$, with coefficient proportional to the superfluid density. The superfluid density is itself a measure of the phase stiffness of the order parameter. Because vortices are topological defects in the order parameter field, their motion leads to order parameter fluctuations, reducing the phase stiffness. Vortices that are "free," *i.e.* have nonzero mobility in the limit $\omega \rightarrow 0$, cause a complete loss of the condensate δ-function. The δ-function is spread to a width determined by rate of order parameter fluctuations, which in turn is determined by the vortex motion.

In the pinned state, vortex mobility disappears in the $\omega \rightarrow 0$ limit. The condensate δ-function is partially restored. The mobility at higher frequency remains nonzero, however, leading to order parameter fluctuations up to characteristic vortex relaxation rates. Conservation of spectral weight dictates that some of the area from the condensate δ-function moves to these higher frequencies.

A more quantitative parameterization of the above ideas begins with the work of Gittleman and Rosenblum [24]. Vortex position $\mathbf{r}_L$ and velocity $\mathbf{v}_L$ are influenced by pinning, drag, and driving forces, which must balance to zero in the long wavelength limit. In the presence of an oscillating superfluid velocity $\mathbf{v}_s(t) = \mathbf{v}_s e^{-i\omega t}$ the equation of motion can be written:

$$\eta \mathbf{v}_L + (\kappa/i\omega)\mathbf{v}_L = (n_s h/2)[\mathbf{v}_s - \alpha \mathbf{v}_L] \times \hat{\mathbf{z}}, \tag{3.1}$$

where η is the viscosity per unit length and κ is the pinning forcer per unit length. The form of the driving force on the right-hand side was introduced by Vinokur *et al.* [25].

The Magnus parameter α determines the magnitude of the Hall effect and has been the subject of considerable controversy. High-frequency measurements find $\alpha \ll 1$ [23], while theoretical predictions yield $\alpha = 1$ for a superfluid with full translation invariance [26]. We will of course respect the experimental results and take $\alpha = 0$ in what follows.

Equation 3.1 can be solved for the vortex velocity $\mathbf{v}_L$ in terms of the superfluid velocity $\mathbf{v}_s$. A trivial application of Faraday's law gives the resulting electric field induced, $\mathbf{E} = \mathbf{v}_L \times \mathbf{B}$. Putting these together gives the vortex resistivity ($\mathbf{E} = \rho_v \mathbf{J}_s$), which adds in series with the condensate resistivity $-i\omega\mu_0\lambda_L^2$:

$$\rho_{xx} = -i\omega\mu_0\lambda_L^2 - \frac{i\omega\mu_0\lambda_c^2}{1 + i\omega/\Gamma} \tag{3.2}$$

where $\Gamma \equiv \kappa/\eta$, λ_c is the Campbell length given by $\lambda_c^2 = B\phi_0/\mu_0\kappa$, and λ_L is the London penetration depth. We have given ρ_{xx} only because experimentally $\rho_{xy} \ll \rho_{xx}$, consistent with $\alpha \ll 1$.

Though ρ is the natural response function for the vortex resistivity, it is helpful to express the response in terms of σ for future comparison with the quasiparticle contributions to the electrodynamics. σ is also a convenient choice due to the powerful spectral weight sum rule. Inverting 3.2 gives the conductivity. In the low-field limit ($\lambda_c^2 \ll \lambda_L^2$) the change in σ_1 is given by

$$\sigma_1(\omega, B) - \sigma_1(\omega, 0) = (\lambda_c^2/\mu_0\lambda_L^4)\left[-\frac{\pi}{2}\delta(\omega) + \frac{1/\Gamma}{1 + (\omega/\Gamma)^2}\right]. \tag{3.3}$$

This confirms the intuition developed earlier; the vortex motion removes spectral weight from the condensate and puts in a channel whose width is given by the characteristic vortex relaxation time Γ. Another important observation is that the spectral weight transfer is linear in H (since $\lambda_c^2 \propto H$).

3.3 Comparison of vortex dynamics models with data

We will use as our primary basis for comparison between vortex dynamics and QPDOS models the field-induced shift in condensate spectral weight. This fundamental quantity characterizes many of the most important effects without getting obscured by details. Because of the coherence of our technique, we perform this measurement simply and accurately.

As discussed in section 1.2.3 the spectral weight in the condensate is given by the coefficient of $1/\omega$ in σ_2. To observe changes in condensate spectral weight, we simply monitor changes in this coefficient. Figure 3.1 shows σ_2 *vs.* $1/\omega$ for YBCO. As the magnetic field strength increases, the slope decreases, showing the decrease in condensate spectral weight.

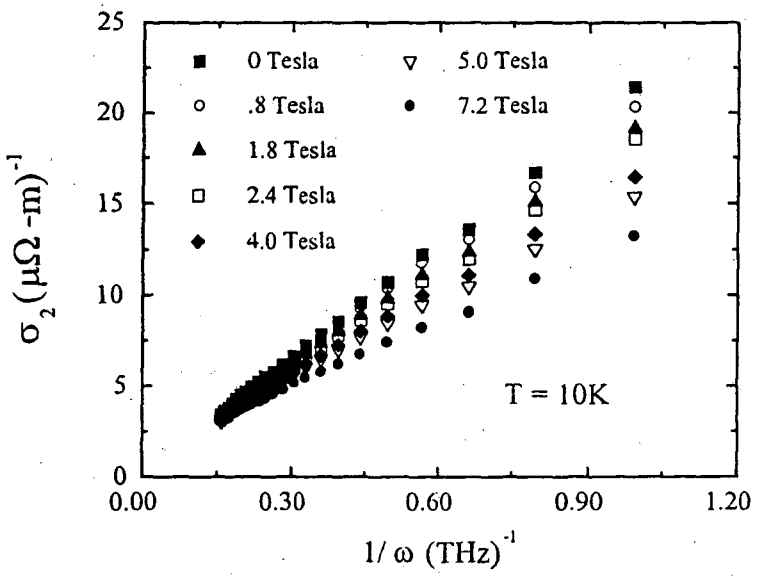

Figure 3.1: σ_2 *vs.* $1/\omega$ for YBCO

It is possible for us to be insensitive to a reduction in condensate spectral weight. If the area shifts from the δ-function to frequencies still much lower than our measurement frequencies, σ_2 remains unchanged in our range. This is a simple consequence of the Kramers-Kronig relations.

In light of this, it is already surprising to find the large changes in σ_2 seen in figure 3.1. As discussed in the previous section, pinned vortex motion causes spectral weight to shift from the condensate to a channel of width $\Gamma = \kappa/\eta$, the characteristic vortex relaxation rate. Since microwave measurements consistently find Γ to be in the ten's of GHz [21], such a shift should be invisible to high-frequency measurements of σ_2.

Nonetheless spectral weight is shifting to higher frequencies in YBCO, and it is shifting linearly in H. Figure 3.2 shows the spectral weight shift as a function of magnetic field for YBCO and for BSCCO, which we will discuss shortly. We refer to the shifted spectral weight as a 'normal' component because it no longer is in the condensate. For YBCO we have linear behavior, relatively insensitive to temperature. This linearity is consistent with a vortex dynamics model, however the presence of the shift at these frequencies is not.

We turn now to similar measurements made on BSCCO. We have performed magnetic field measurements on three BSCCO samples. They are 610, 655, and 740 Å thick c-axis oriented films grown on [100] $LaAlO_3$, with two to three layers of the 2201 BSCCO phase grown for substrate lattice matching. They were grown using atomic layer-by-layer molecular beam epitaxy with in-situ monitoring by reflective high-energy electron diffraction to ensure single-phase growth [27]. They show a resistance R linear in T above T_c, with resistance ratios $R(300)/R(0) \geq 10$.

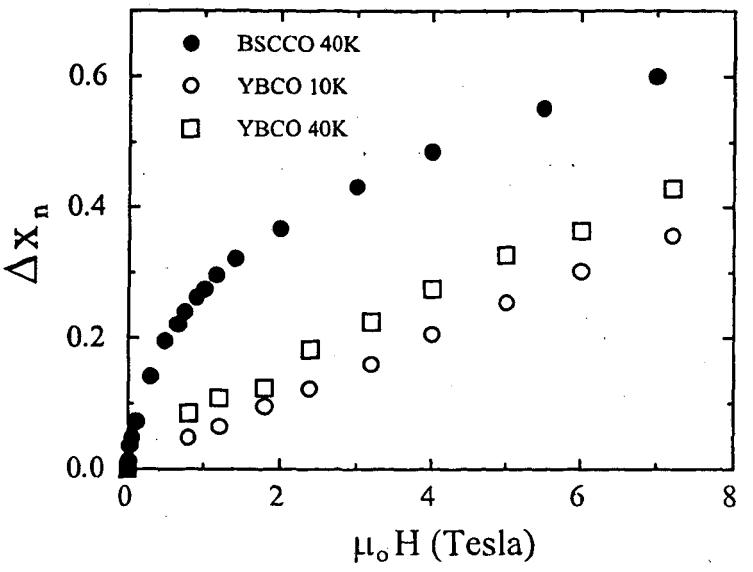

Figure 3.2: Spectral weight shift as a function of magnetic field for YBCO and for BSCCO

The samples have transition temperatures ranging from 74-80 Kelvin. Similar films were studied recently by angle-resolved photoemission and found to have spectra consistent with the bulk crystal analog [29]. We believe the films are all in the underdoped regime; the 610 nanometer film (sample 1280) was deliberately underdoped by replacing 10% of the strontium sites with dysprosium, which has an extra valence electron. The samples all show similar magnetoconductivities, so we will focus on the most well-characterized sample (sample 1249).

Figure 3.3 shows the H and T dependence of the magnetoconductivity at $\omega/2\pi =$ 150 GHz, the center frequency of our large dipole antennas [28]. The data show a number of interesting effects. Most notable is the highly sublinear dependence of σ_2 on magnetic field. σ_2 varies approximately as $H^{1/2}$ over a wide range of field and temperature. At 7 Tesla, it has dropped to about 60% of its zero field-value. The effect is remarkably insensitive

to temperature, given the large changes in vortex mobility over the temperature range. The changes in σ_1 are more complex. σ_1 increases rapidly at low fields, flattens out, and eventually *decreases* with increasing field strength.

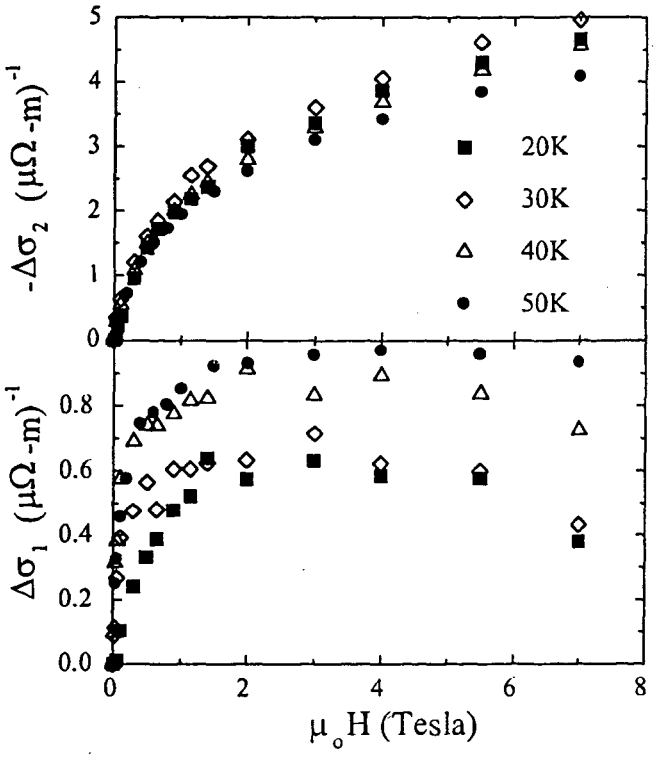

Figure 3.3: Real and imaginary parts of $\Delta\sigma(H) \equiv \sigma(H) - \sigma(0)$ at 150 GHz.

We will not focus here on the behavior of $\Delta\sigma_1$. Such changes are difficult to interpret because many factors contribute. In addition to spectral weight shifts, $\Delta\sigma_1$ reflects changes in transport of *existing* quasiparticles due to the presence of the field and the vortices. We instead follow our program of tracking condensate spectral weight shifts by studying changes in σ_2.

The sublinear behavior of $\Delta\sigma_2$ seen in figure 3.3 is inconsistent with the linear

prediction of the vortex dynamics model in eq. 3.3 with field-independent pinning and viscosity parameters κ and η. However, this is not enough to rule out the vortex dynamics picture of electrodynamic response. κ and η are simply parameters in the model and can be given the necessary field dependence to fit a wide range of behavior. One must ask whether the resulting field dependence is physically reasonable.

BSCCO offers a unique opportunity to answer this question. Because of the large temperature and field range for which vortices are in the liquid state, the response at high frequency can be compared directly to the *dc* response. This is not the case in YBCO, where the vortices remain pinned for most of the H-T phase diagram and hence are unable to completely destroy the condensate δ-function. Because of the unpinned vortices in BSCCO, the *dc* resistivity is not 'shorted' by a condensate.

Hence if we have a model that describes both the *dc* and the high-frequency response, we can evaluate the plausibility of the vortex dynamics interpretation. Several theorists have recently reached similar conclusions and presented such a model that neatly captures the essential aspects of the vortex dynamics picture [30, 31, 32]. We discuss here the work of Coffey and Clem [30].

The equation of motion for a pinned vortex is of the Gittlman-Rosenblum form, equation 3.1 with $\alpha = 0$. This equation, however, does not include the possibility of thermally-activated flux creep. At lower frequencies, the vortices will often diffuse off their pinning site before a cycle of the electromagnetic wave is complete. Coffey and Clem include this effect by modeling the vortex-pinning interaction as a particle undergoing Brownian motion on a periodic potential with amplitude U and curvature κ near the potential minima.

This modifies the equation of motion (3.1) by adding to the driving force a random element, assumed to be Gaussian. Coffey and Clem calculate the resulting frequency-dependent resistivity, valid from *dc* to $\omega = \infty$. The real part is given by

$$\Delta\rho_1 = \rho_{B-S}\frac{\chi + (\omega\tau_0)^2}{1 + (\omega\tau_0)^2}, \tag{3.4}$$

where the low-frequency resistivity is proportional to a "creep factor" $\chi = 1/I_0^2(\nu)$ describing thermal activation over the barrier. Here I_0 is the modified Bessel function and $\nu \equiv U/k_BT$. The resistivity change approaches the Bardeen-Stephen resistivity $\rho_{B-S} = B\phi_0/\eta$ in the limit that the frequency is much larger than the inverse of the vortex relaxation time $\tau_0 \equiv (\eta/\kappa)(I_0^2 - 1)/(I_1(\nu)I_0(\nu))$.

We can now use the magnitude and field dependence of *dc* resistivity measurements to fit the parameters ρ_{B-S} and $\chi(\nu)$. Nonlinear field dependence enters this model because the barrier height U (and hence χ) depend on field. Various measurements, including *dc* resistivity, consistently find U to be a decreasing function of magnetic field [33].

Figure 3.4 shows a comparison of the model to *dc* and high-frequency resistivity. The y-axis is the resistivity at a representative temperature of 50 K, normalized to the Bardeen-Stephen (B-S) resistivity. Since the vortex density and the B-S resistivity are both linear in H, this is a convenient dimensionless measure of the magnetoresistivity per vortex. $U(H)$ and ρ_{B-S} have been adjusted for a best fit, the solid line passing through the *dc* data. This leaves only one parameter to account for the high-frequency data, the vortex relaxation time τ_0. The remaining solid lines in figure 3.4 show the model predictions for $\omega\tau_0 = 0, .3$ and 1. In the limit that $\omega\tau_0 \to \infty$, the resistivity per vortex approaches a flat line at unity.

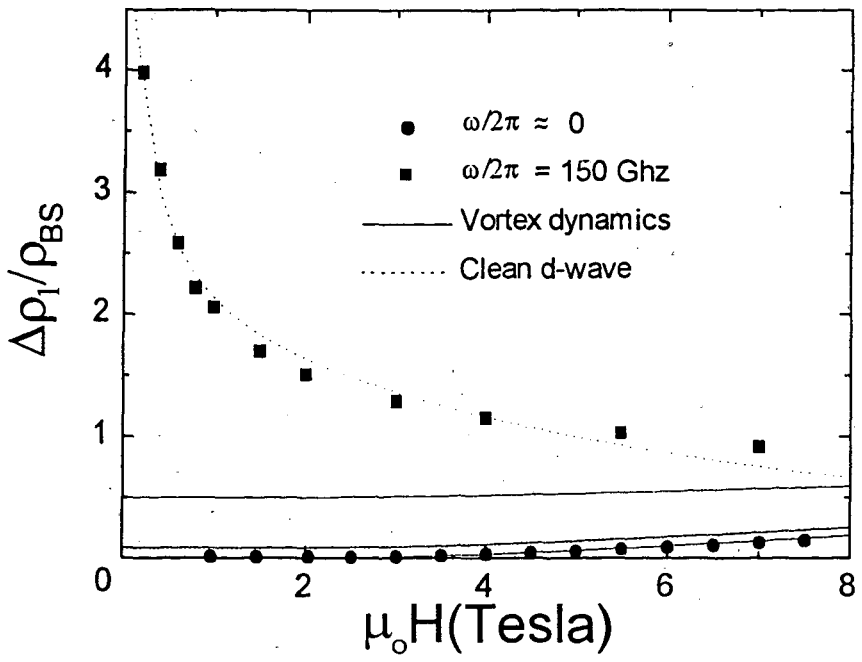

Figure 3.4: Magnetoresitivity per vortex compared to vortex dynamics models

The contrast with the data at 150 GHz (squares) is severe. The high-frequency resistivity per vortex diverges as $H \rightarrow 0$, while the model predictions approach a field-independent behavior. Though this does not completely rule out the vortex dynamics interpretation, the behavior of the barrier height $U(H)$ at high frequency would have to be opposite to the behavior at low frequency. The implausibility of such behavior contrasts with the natural explanation that follows from d-wave electrodynamics.

3.4 QPDOS model

3.4.1 *D*-wave density of states

We turn next to the electrodynamics of d-wave superconductors and discuss a model for vortex response based on the low-energy quasiparticle density of states. Yip and Sauls [7] first pointed out the importance of the QPDOS for the electrodynamics. Many unusual properties of cuprate superconductors appear to arise from the linear-in-energy QPDOS, so we begin with a description of this important characteristic.

Our starting point will be a BCS model of the local density of states (DOS) on the Fermi surface using the local value of the energy gap, $\Delta(\theta)$. We call $N(E,\theta)$ the density of states at energy E and angle θ relative to the node, normalized to the normal-state DOS. Then $N(E,\theta)$ is given by

$$N(E,\theta) = \frac{E}{\sqrt{E^2-\Delta^2(\theta)}}\Theta(E^2-\Delta^2(\theta)). \tag{3.5}$$

Here Θ is the unity step function. Though we take this as an intuitive starting point, Yip and Sauls [7, 8] arrive at this form with a more careful Green function analysis based on Fermi liquid theory.

For a clean d-wave superconductor the energy gap near the node $\Delta(\theta)$ is linear in θ with slope given by $\mu\Delta_0 \equiv \partial\Delta/\partial\theta$. The total density of states, $\tilde{N}(E)$, is given by integrating (3.5) over the arc in k-space satisfying $\Delta(\theta) \leq E$:

$$\tilde{N}(E) = 2\int_{\theta=0}^{\theta=E/\mu\Delta_0} d\theta \frac{E}{\sqrt{E^2-\Delta^2(\theta)}}\Theta(E^2-\Delta^2(\theta)) \approx \frac{2E}{\mu\Delta_0}. \tag{3.6}$$

This result, which is the contribution from one node only, is valid for $E \ll \Delta_0$ so that $\Delta(\theta) = \mu\Delta_0\theta$. We see from this analysis that the density of states is linear in energy, with

coefficient determined by the slope of the gap near the node.

3.4.2 Response to a supercurrent

Yip and Sauls [7] laid the foundation for understanding the importance of gap nodes to the vortex conductivity by describing how the linear density of states impacts the response to a supercurrent. Based on earlier work by Bardeen [34], they pointed out that the quasiparticle creation energy shifts in the presence of a superfluid velocity $\mathbf{v_s}$ by an amount $\epsilon = (m^*/2)\mathbf{v_F} \cdot \mathbf{v_s}$. In an s-wave superconductor, this shift has little consequence so long as $\epsilon \ll \Delta$. In a d-wave superconductor, the linear density of states gives the shift far-reaching consequences.

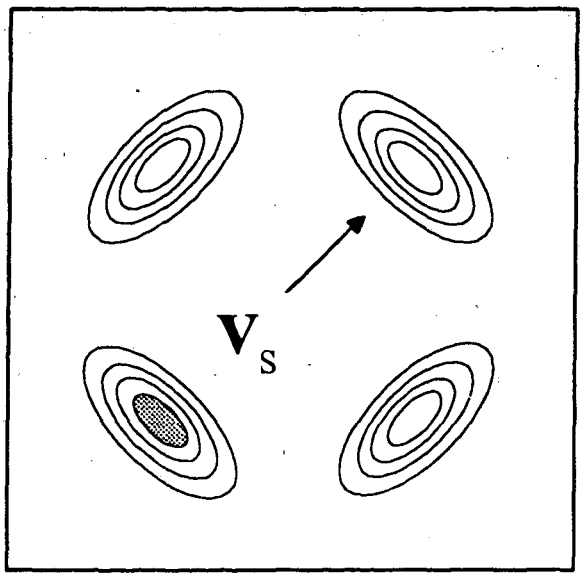

Figure 3.5: Fermi Surface and equal-energy contours in the presence of a superfluid velocity. The superfluid velocity is directed along a nodal direction, resulting in occupied quasiparticle states with opposite velocity (shaded region). The lines depict equal-energy contours of quasiparticle states.

Figure 3.5 depicts the Fermi surface for a superfluid velocity directed along a nodal

direction. Quasiparticle creation energies shift proportionally to $\mathbf{v_s} \cdot \mathbf{v_F}$, so that states with velocity directed oppositely to $\mathbf{v_s}$ shift below the chemical potential and become occupied. This is depicted in the shaded region. The lines depict equal-energy contours. If $\mathbf{v_s}$ is not along a nodal direction, two pockets of Fermi surface open up. Each has a size proportional to the projection of $\mathbf{v_s}$ onto the Fermi velocity at that node.

The fraction of normal states created by a superfluid velocity $\mathbf{v_s}$ (directed along a node) is easy to calculate. We simply plug in the quasiparticle energy shift $\epsilon = (m^*/2)\mathbf{v_F} \cdot \mathbf{v_s}$ to the normalized density of states $\tilde{N}(E) = 2E/\mu\Delta_0$ to find

$$\Delta x_n(v_s) = \frac{m^* v_s v_{nF}}{\mu \Delta_0} \equiv v_s/v_0. \tag{3.7}$$

Here v_{nF} is the Fermi velocity at the node and x_n is the fraction of normal electrons, n_n/n_{total}. In labeling it as such we are making a bit of a leap; technically, we have calculated only the density of quasiparticle states created by v_s. Calculating the fraction of normal electrons involves finding the contribution of these states to the transport of current. This more rigorous calculation, done by Yip and Sauls [7, 8] gives the same result. This is because all of the states near the node have the same velocity, $\mathbf{v_F}$. For superfluid velocities directed between nodes, $\mathbf{v_s}$ is simply decomposed into orthogonal components along the nodes and the calculation proceeds identically.

Equation 3.7 is the central result in the theory of d-wave electrodynamics. Even at $T = 0$ a superfluid velocity creates a normal component of electrons, with density proportional to v_s. In an s-wave superconductor at $T = 0$, the superfluid velocity has no effect until a critical velocity is reached such that $(m^*/2)v_s v_F \approx \Delta$.

In the clean limit of a superconductor, all of the spectral weight from the supercon-

ducting electrons is in the superfluid δ-function. Creation of a normal fraction Δx_n leads to an equally large depletion of the condensate fraction, $\Delta x_s = -\Delta x_n$. In our measurements we can see this condensate depletion by looking at σ_2.

3.4.3 Application to the vortex state

Let us consider the implications of equation 3.7 on the vortex-state conductivity. The vortex consists of a core of normal electrons surrounded by superfluid currents with velocity $v_s(r) = \hbar/m^* r$ at distances r large compared to the vortex core size ξ. In an s-wave superconductor at zero temperature these currents have no effect on the quasiparticle population. Outside the core, v_s is always less than the critical velocity $v_c = \Delta/(m^*/2)v_F$, so that the condensate remains intact. All of the normal electrons live in the core, which is bounded by the condition $v_s(\xi) = v_c(\xi)$. In d-wave superconductors, we have seen that any superfluid velocity will deplete the condensate, according to $\Delta x_s = -v_s/v_0$. Thus normal electrons exist throughout the vortex current pattern rather than at the core only.

A simple calculation similar to the one done by Volovik [35] on the field-dependent density of states yields the magnetic field dependence of σ_2. As long as spatial variations of the order parameter are slow compared to the coherence length ξ it is reasonable to define local superfluid and normal fractions $x_s(r)$ and $x_n(r)$, with $x_s(r) + x_n(r) = 1$. Then the local superfluid velocity $\mathbf{v_s}(\mathrm{r})$ directed at an angle $\theta \leq \pi/2$ from a node creates a fraction of normal electrons given by

$$\Delta x_n(\mathbf{r}) = \frac{m^*}{\mu \Delta_0} v_{nF} v_s(r)(|cos\theta| + |sin\theta|) \tag{3.8}$$

where v_{nF} is the Fermi velocity at the nodes.

The total normal fraction created, $\Delta x_n(H)$ is the spatial average of $\Delta x_n(\mathbf{r})$. Following Volovik, we approximate the unit cell as a circle with radius equal to half the inter-vortex separation $R = 2(\phi_0/\pi H)$. $\Delta x_n(H)$ is computed by averaging equation 3.8 over the unit cell, using $v_s(r) = \hbar/m^* r$:

$$\begin{aligned}\Delta x_n(H) &= \frac{1}{\pi(R/2)^2}\int^{R/2} r dr d\theta \frac{m^*}{\mu\Delta_0} v_{nF} \frac{\hbar}{m^* r}(|cos\theta| + |sin\theta|) \\ &= \frac{1}{\pi(R/2)^2}\frac{\hbar v_{nF}}{\mu\Delta_0}(R/2)8 \\ &= \frac{8}{\pi(R/2)}\frac{\hbar v_{nF}}{\mu\Delta_0}.\end{aligned} \tag{3.9}$$

Using $(R/2) = (\phi_0/\pi H)^{1/2}$ we can write this as

$$\Delta x_n(H) = \sqrt{\frac{H}{H_0}}, \quad H_0 = \frac{\pi\phi_0}{64}(\frac{\mu\Delta_0}{\hbar v_{nF}})^2. \tag{3.10}$$

We have ignored here the normal electrons from the core. If we put in the appropriate cutoff ξ for the lower limit in eq. 3.9 and then add the normal fraction from the core, $(2\xi/R)^2$, we find a correction linear in H that is much smaller than the $H^{1/2}$ contribution. Plugging in experimentally determined values for $\xi, \hbar v_{nF}$, and $\mu\Delta_0$ in BSCCO, we find that even at $H = 10$ Tesla, the $H^{1/2}$ contribution is over 60 times larger than the linear correction.

It is interesting to note that the d-wave theory defines a natural length scale given by $(\hbar v_{nF}/\mu\Delta_0)$. In BSCCO this length comes out to 28 Å, determining the field scale H_0 of only 12.5 Tesla. We can compare that to a value for H_{c2} inferred from a typical value $\xi = 17$ Å of about 220 Tesla.

3.4.4 Comparison with experimental data

In section 3.3 we compared the high-frequency data on BSCCO with models based on vortex dynamics. We now do the same for the QPDOS model. Unlike the vortex dynamics models, the QPDOS model has no free parameters. It predicts the size and field-dependence of the spectral weight transfer using only parameters available from zero-field measurements.

We have seen already elements of the model giving qualitative agreement with some of the data. The $H^{1/2}$ dependence of σ_2 indicates a depletion of condensate spectral weight consistent with the $H^{1/2}$ predictions of the model. To highlight differences from the clean d-wave model and to begin a more quantitative comparison, we again show σ_2 vs. H, this time on a log-log scale and for various frequencies.

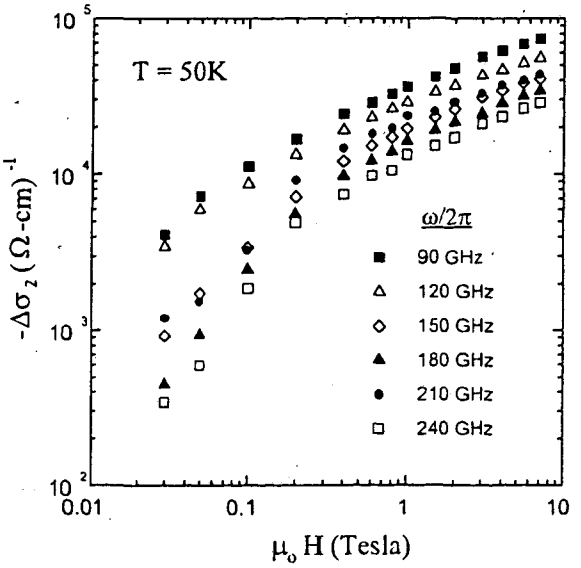

Figure 3.6: σ_2 *vs.*H on a log-log scale for various ω, at T=50K.

We see in figure 3.6 that above $H = .2$ Tesla, σ_2 exhibits clean power-law behavior,

with exponent close to 1/2, over a wide range of frequencies. Below .2 Tesla, there is a significant departure from $H^{1/2}$ which strengthens at higher frequencies. We will return to discuss this departure shortly.

The QPDOS model for a clean d-wave superconductor predicts the fraction of normal electrons created by a superfluid velocity $\mathbf{v_s}$. Two parameters are needed for this prediction: the Fermi velocity at the nodes, v_{nF}, and the slope of the gap function near the nodes, $\mu\Delta_0$. Both of these parameters are available from zero-field measurements of the angle-resolved photoemission. When combined with the relation for the superfluid velocity around a vortex, $v_s(r) = \hbar/m^* r$, the model makes a quantitative prediction for the fraction normal electrons as a function of distance r from the vortex center. This is given by performing the angular integration of equation 3.8:

$$\Delta x_n(r) = (\frac{\hbar v_{nF}}{\mu\Delta_0})(\frac{4}{r}). \tag{3.11}$$

We now show that the raw data for σ_2 vs. H can be recast to yield the *same* quantity.

We begin by expressing $\Delta\sigma$ in terms of the change in normal fraction. Equation 1.3 gives the conductivity for the condensate and quasiparticle system in the two-fluid model. We rewrite that here:

$$\sigma(\omega) = \frac{n_s e^2}{m}[\frac{\pi}{2}\delta(\omega) + i/\omega] + \frac{n_n e^2 \tau_n}{m}\frac{1}{1 - i\omega\tau_n}. \tag{3.12}$$

We use this form to express $\Delta\sigma$ in terms of $\Delta x_n \equiv \Delta n_n/n_{total}$, ignoring the δ-function since we are at high frequency:

$$\Delta\sigma = \epsilon_0\omega_p^2\Delta x_n[S(\omega) - i/\omega]. \tag{3.13}$$

Here $\omega_p^2 = n_{total}e^2/\epsilon_0 m$ is the plasma frequency, $S(\omega)$ is the frequency dependence of the quasiparticle response, and we have used the clean-limit relation $\Delta n_s = -\Delta n_n$. If we

assume that $\mathrm{Im}[S(\omega)] \ll 1/\omega$, which is true in the Drude model for $\omega\tau \ll 1$, then the change in normal fraction is given simply by

$$\Delta x_n = -\frac{1}{\epsilon_0 \omega_p^2} \Delta\sigma_2. \tag{3.14}$$

The plasma frequency ω_p is attainable by combining normal-state measurements of the conductivity, for which $\sigma = \epsilon_0 \omega_p^2 \tau$, with published values of τ from infrared measurements. We can check the value thus obtained by comparing it to the coefficient of $1/\omega$ in the superconducting σ_2 at low temperature. A sample with conductivity phase change very close to $\pi/2$ in passing from high temperature to very low temperature has nearly complete carrier condensation, so that the two quantities match.

Having expressed Δx_n in terms of $\Delta\sigma_2$, we now consider the relationship between this *total* (or *average*) normal fraction, and the *local* normal fraction $\Delta x_n(r)$. We obtain the total change in normal fraction as a function of the intervortex separation R by integrating the local change $\Delta x_n(r)$ over the unit cell:

$$\Delta \bar{x}_n(R) = \frac{1}{\pi(R/2)^2} \int^{R/2} 2\pi r dr \Delta x_n(r). \tag{3.15}$$

The function $\Delta\bar{x}_n(R)$ comes from $\Delta\sigma_2(H)$ measurements, as described above. To access the function $\Delta x_n(r)$, we simply differentiate both sides of equation 3.15 with respect to $R/2$:

$$\Delta x_n(r) = \frac{1}{4r} \frac{d}{dR} [R^2 \Delta x_n(R)]|_{R/2=r}. \tag{3.16}$$

Equations 3.11 and 3.16 are the theoretical and experimental functions $\Delta x_n(r)$. We plot each of these in Figure 3.7 as a function of $1/r$. The experimental data is the same as shown in figure 3.3; the dashed line is a plot of the QPDOS model, eq. 3.11 with

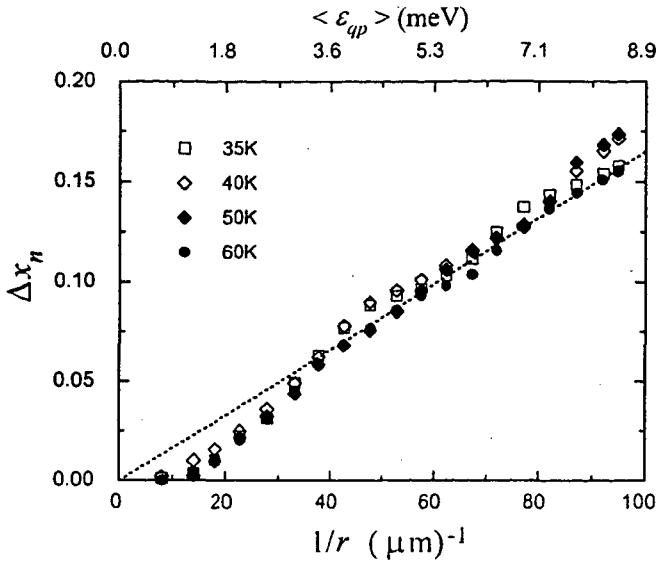

Figure 3.7: Local fraction of normal electrons *vs.* inverse distance from the vortex center, and *vs.* quasiparticle energy shift for BSCCO. The data shown here were taken at $\omega/2\pi$ =150 GHz.

values of $\hbar v_{nF} = 140\text{mev} - \text{nm}$ and $\mu\Delta_0 = 54\text{meV}$ taken from angle-resolved photoemission measurements [36, 37].

The agreement between the QPDOS model and the data is remarkable. The experiment accesses over a decade of r, from 100 to 1200 Å. In an s-wave superconductor, we would expect a very different magnitude and r dependence at such large distances from the vortex core. $\Delta x_n(r)$ would be essentially zero for r much larger than ξ (≈ 17Å), and increase to unity near $r = \xi$.

On the top axis we have converted $1/r$ to quasiparticle energy shift by combining the relation $v_s(r) = \hbar/m^* r$ with the quasiparticle energy shift $\epsilon_{qp} = (m^*/2)\mathbf{v_s} \cdot \mathbf{v_F}$ (and performing the angular average). Viewed in this manner, the experiment is something of a spectroscopy of the gap node. The Δx_n measures the area of Fermi surface, and ϵ_{qp} is the

energy away from the chemical potential.

Above 3 meV, the QPDOS model provides an excellent description of the vortex electrodynamic response. The data show linear behavior with a slope extremely close to that prescribed by the parameters $\hbar v_{nF}$ and $\mu\Delta_0$. Below 3 meV, we see a departure from the clean d-wave prediction which corresponds to the departure from $H^{1/2}$ at low fields seen in figure 3.6. There are a number of possibilities for this departure.

The first that comes to mind is the nonzero temperature of the measurement. The model presented thusfar is valid at $T = 0$. There is a crossover in the theory when the quasiparticle energy shift $(m^*/2)\mathbf{v_s} \cdot \mathbf{v_F}$ becomes smaller than $k_B T$. In this regime the normal fraction created from $\mathbf{v_s}$ is quadratic rather than linear in v_s. We should expect, then, that at low energies Δx_n come in to zero quadratically.

We rule this possibility out because of the complete lack of temperature dependence of the data. If the low-energy departure were related to this temperature crossover, we should see its onset change by close to a factor of two. It is, in fact, something of a mystery why the $T = 0$ theory works so well. The temperature range shown corresponds to energies from about 3 to 6 meV, which passes right through ϵ_{qp} in this experiment. This remains an open question for us.

Another possibility for the low-energy deviation is a finite frequency effect. Although no theory has been worked out for the response at high frequency, it is reasonable to expect a crossover from dc behavior when $\hbar\omega$ becomes comparable to the quasiparticle energy shift ϵ_{qp}. When this occurs, the photons no longer simply probe the Fermi surface area. Direct excitations across regions of small gap make an important contribution. The

data shown in figure 3.7 correspond to $\hbar\omega = .6$ meV, which is beginning to approach the 3 meV departure energy. This finite-frequency interpretation is supported by the observation that the deviation from clean d-wave behavior is larger at higher frequencies (figure 3.6).

The remarkable agreement between the QPDOS model and the experiment indicates that we have quantitatively described the high-frequency vortex response. The QPDOS description has the elegance of involving no fitting parameters; two measurable parameters describe the spectral weight transfer, and one more gives the resulting changes in σ_2. There is still an unresolved issue, however, which is what is happening in YBCO.

3.5 The mystery of YBCO

These measurements on BSCCO were originally motivated by an incomplete description of high-frequency vortex dynamics in YBCO. Having seen that the d-wave electrodynamics completely describes the response of BSCCO in the vortex liquid state, we can more sharply define the issues in YBCO.

The linearity of $\Delta\sigma_2$ with H in YBCO presents a problem for the QPDOS description. One can ask whether the vortex dynamical effects do in fact dominate the QPDOS effects in YBCO. Referring back to figure 3.2, which compared the spectral weight shifts in YBCO and BSCCO, we see that the total depletion of superfluid in YBCO is always *smaller* than that in BSCCO. We can conclude from this that the QPDOS effects must not be present in full form as they are in BSCCO. If they were present in full form and simply overshadowed by larger vortex dynamical effects, than the spectral weight shifts should be *larger* in YBCO than in BSCCO.

To account for the smaller spectral weight shifts in YBCO, we must conclude that the QPDOS effects are somehow inhibited. One strong possibility is that the comparatively strong pinning prevents the vortices from attaining their equilibrium separation in YBCO. The $H^{1/2}$ behavior in the QPDOS model depends heavily on the vortices maintaining equilibrium separation. Without it, the pairbreaking effects are still there, but the $H^{1/2}$ dependence is lost.

Evidence to support this picture comes from recent scanning tunneling microscopy (STM) observations of the vortex lattice in YBCO [38]. It was observed in twinned crystals of YBCO that as H was decreased, the vortices did not maintain uniform separation, but separated into regions devoid of vortices and regions that maintained the original vortex density. Such behavior of the vortex density would yield linear field dependence of the spectral weight shifts in the QPDOS model as well as the vortex dynamics picture.

Even in BSCCO we begin to see the $H^{1/2}$ behavior gradually moving toward linear behavior as we cool below 25 Kelvin and enter the vortex solid phase. Figure 3.8 shows the intermediate and low-temperature changes in σ_2 with field, from 6 to 30 Kelvin. Also shown, as guides, are lines depicting $H^{1/2}$ and H behavior. As the temperature is lowered, the field dependence is shifting toward linear, particularly at low fields. It is reasonable that the effects would be stronger in YBCO, as the vortices have a 'line tension' that is barely present in BSCCO vortices, making pinning much more effective.

Resolving conclusively the different behavior in YBCO and BSCCO remains an important task. If our suggestion is correct, than the electrodynamics of YBCO is also dominated by QPDOS effects rather than vortex dynamical effects. Such a realization would

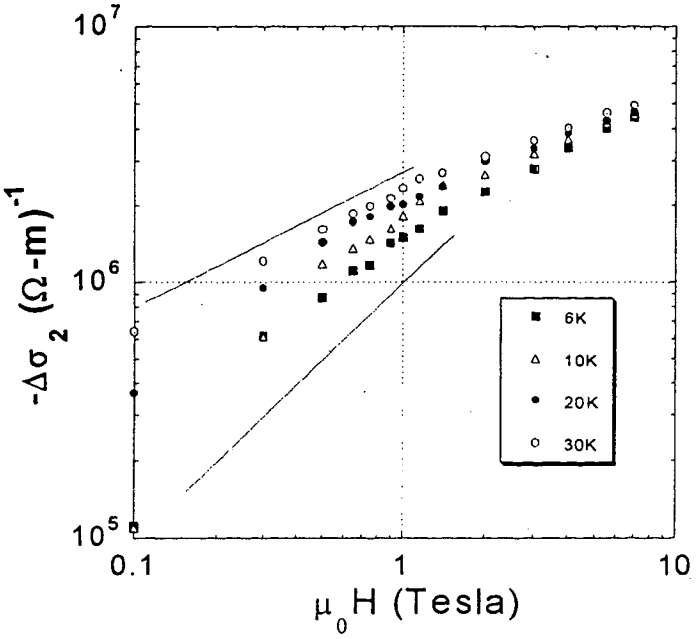

Figure 3.8: $\Delta\sigma_2$ vs. H for BSCCO at intermediate and at low temperatures. Also shown are lines depicting $H^{1/2}$ and H dependence. At low temperature, the vortices become pinned, leading to linear field response.

completely change the current picture of mixed-state electrodynamics in the cuprates.

Chapter 4

Zero-Field Properties

In the previous chapter we built an understanding of the vortex response by studying spectral weight shifts. The more complicated changes in σ_1 we set aside because of the complexity of quasiparticle dynamics. In general, understanding the magnetic field response of a system requires first an understanding of the zero-field response. We were able to understand σ_2 in a field because the behavior in zero field is particularly simple. With quasiparticle dynamics, the zero-field properties are far more complicated and not well understood. The 'frontiers' of σ_1 are still at the zero-field response. So rather than push to understand quasiparticles in a field, we seek to broaden our understanding of high-frequency electrodynamics by studying their zero-field properties, both in the normal and superconducting state.

Attempts to understand the quasiparticle response focus on the frequency and temperature dependence of the renormalized quasiparticle scattering rate $\Gamma_*(\omega, T) \equiv 1/\tau_*(\omega, T)$. This quantity is one of the primary parameters in the *extended Drude*, or *memory function*

[5] analysis of the conductivity, in which the simple Drude model is generalized to parameterize a more general linear response function. The Drude scattering time τ and mass m are given frequency dependence so that the conductivity is written

$$\sigma(\omega) = \frac{ne^2}{m^*(\omega)} \frac{1}{\tau_*^{-1}(\omega) - i\omega}, \tag{4.1}$$

where m^* and τ_*^{-1} are the renormalized mass and scattering rate.

In the normal state, with all the spectral weight in one channel, τ_* can be obtained from the phase of σ: $\omega\tau_* = \tan^{-1}(\sigma_2/\sigma_1)$. In the superconducting state the imaginary part of σ is dominated by the superfluid response, so that only the real part sheds light on the quasiparticle response. In this case τ_* cannot be separated easily from the quasiparticle density n_q.

In this chapter we study the conductivity in both normal and superconducting states. In the normal state we discuss the first terahertz measurements on underdoped BSCCO and show how they provide strong evidence against widespread conclusions recently drawn from infrared measurements. In the superconducting state we to pull together data from various measurements, including microwave and infrared, and discuss evidence for unusual quasiparticle dynamics. The study of superconducting-state quasiparticle dynamics has received little attention recently, largely due to a shortage of new experimental results. We would like to discuss the new results that do exist and how they point to some strange behavior. We would also like to show that recent improvements in measurement technique (especially our own) can provide information necessary to advance this fascinating and largely unsolved area of superconductivity.

4.1 Superconducting-state YBCO

When measurements of $\sigma_1(T)$ at low temperature in YBCO were first reported [39] a peak was found below T_c that bore passing resemblance to the Hebel-Schlichter coherence peak in an s-wave superconductor [6]. A coherence peak explanation lacks consistency with NMR measurements of the nuclear relaxation rate T_1^{-1}, which show no such peak in spite of having the same coherence factors. The following year microwave measurements from Bonn and Hardy [40, 41] solidified the now famous explanation of the conductivity.

Figure 4.1 shows σ_1 vs. T at 4 and 35 GHz from reference [42]. The conductivity begins to rise rapidly above T_c, and continues rising after T_c has been crossed. At approximately 40 Kelvin, σ_1 achieves its maximum value and then begins to fall as the temperature is further decreased.

As explained by Bonn and Hardy [40], the peak occurs because of a large increase in the quasiparticle lifetime as the temperature is lowered. Bonn and Hardy found that $1/\tau_*$ drops by almost two orders of magnitude from its normal state value at 100K. At frequencies below $1/\tau_*$ (at $T = T_c$), this leads to an increase in the conductivity. As the temperature drops further, two effects can lead to the ensuing decrease in the conductivity. The decreasing quasiparticle population is one mechanism for lowering the conductivity. The other is for $1/\tau_*$ to sweep below the measurement frequency. Bonn and Hardy later estimated that $1/\tau_*$ reaches its limiting low-temperature value of 60-70 GHz by roughly 40 Kelvin [41].

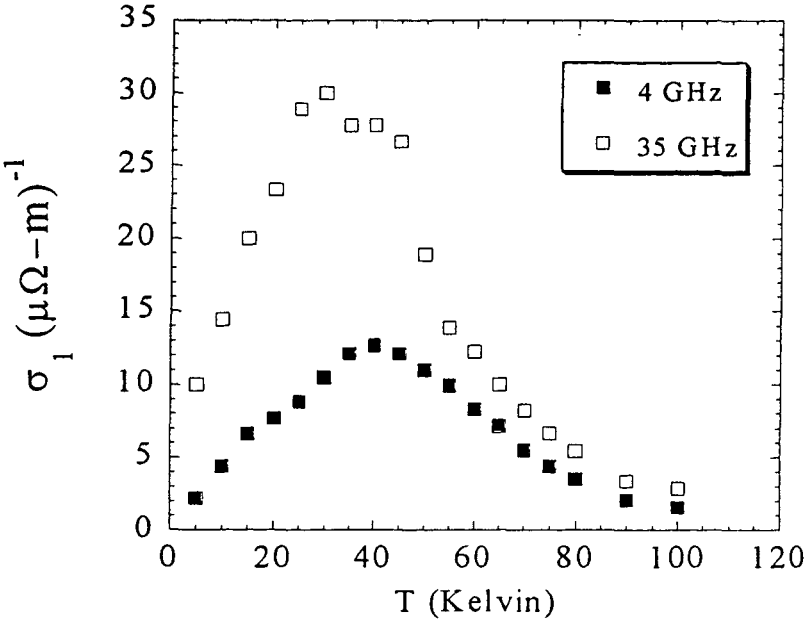

Figure 4.1: σ_1 vs. T for YBCO

4.2 Superconducting-state BSCCO

BSCCO is a system we might expect to show similar quasiparticle behavior as YBCO. Both share similar Fermi surface structure, described nicely be a two-dimensional tight-binding Hamiltonian. The BSCCO band has a higher filling factor than YBCO [48], leading to a slightly smaller Fermi surface (since the carriers are holes).

Microwave studies on BSCCO crystals have been performed by Lee *et. al.* [44] and by Jacobs *et. al.* [45] with interesting results. Figure 4.2 shows conductivity data taken from reference [44]. The microwave cavity experiment was performed on an ultra-high quality, $T_c = 93$ Kelvin single crystal. The sample showed a linear temperature dependence in the

penetration depth at low T, indicating a clean nodal region. The figure shows σ_1 vs. T at 14.4, 24.6 and 34.7 GHz.

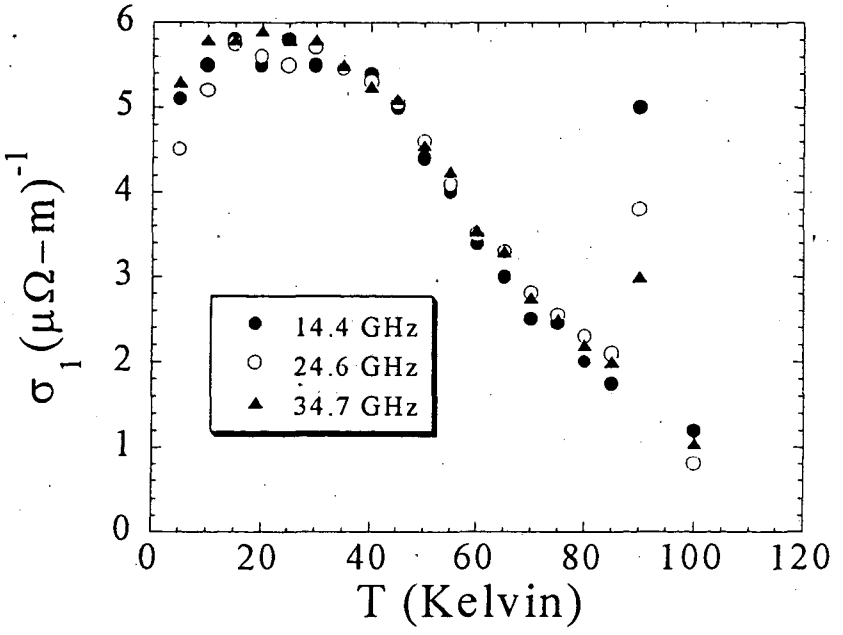

Figure 4.2: Microwave σ_1 data on BSCCO from Lee, *et al.*

As in YBCO, σ_1 continues increasing below T_c. However, to the lowest temperatures they measured, (5 Kelvin) the conductivity shows no strong peak. It steadily increases from high temperature to low, with the possibility of a slight downturn at the lowest temperatures. The low-temperature value is similar to that in untwinned YBCO crystals [41]. What is more striking, though, is the complete lack of frequency dependence in the data. From 14.4 to 34.7 GHz, the conductivity is the same throughout the entire temperature range. The data on YBCO (figure 4.1) show a large difference between the conductivity

at 4 GHz and 35 GHz. We conclude from these measurements that the quasiparticle scattering rate in BSCCO is well above their maximum frequency of 35 GHz. When combined with the observation that the conductivity bottoms out at a significantly nonzero value, there appears to be substantial spectral weight that has not collapsed into the superfluid δ-function, even at the lowest temperatures. We will shortly present more in-depth analysis of this situation.

It is also worthwhile to compare the low-temperature value of the conductivity to the universal d-wave σ_1 in the limit of low impurity concentration, $\sigma_1^{univ} = (e^2/2\pi\hbar)(\xi_0/a)$ [46]. Here ξ_0 is the coherence length, given by $\hbar v_F/\pi\Delta_0$, and a is the lattice spacing. Using the values $\hbar v_F = 140\text{meV} - \text{nm}$ from photoemission [36], and $\Delta_0 = 25\text{meV}$, along with in-plane and out-of-plane lattice spacings of 3.81 and 15.4 Å, we find $\sigma_1^{univ} = 1.2{\cdot}10^5(\Omega - \text{m})^{-1}$. This is a factor of 50 lower than the low-temperature BSCCO conductivity, and a factor of 15 lower than that of YBCO.

We have performed measurements at higher frequency in hopes of further shedding light on the situation. Three BSCCO films have been studied: a nearly optimally doped film with T_c of 85 Kelvin (sample 1388), and two moderately underdoped film with $T_c = 72$ Kelvin (sample 1280) and 70 Kelvin (sample 1249). The two underdoped samples show similar behavior, so we present data from the one we have characterized most. We will refer to the nearly-optimally doped film as 'optimally-doped' to distinguish it from the underdoped samples, though in reality it is most likely slightly underdoped.

Figure 4.3 shows σ_1 and σ_2 vs. T at various frequencies for the nearly optimally doped film. The behavior of σ_1 undergoes a large change between 120 and 200 GHz. At our

lowest frequency of 120 GHz, we see the same behavior as the microwave measurements in figure 4.2. σ_1 steadily increases below T_c but does not exhibit a peak. The magnitude of the conductivity is consistent with the data of Lee, *et. al.* At higher frequencies (200 GHz and above) the conductivity peaks at T_c and then decreases monotonically as the temperature is lowered.

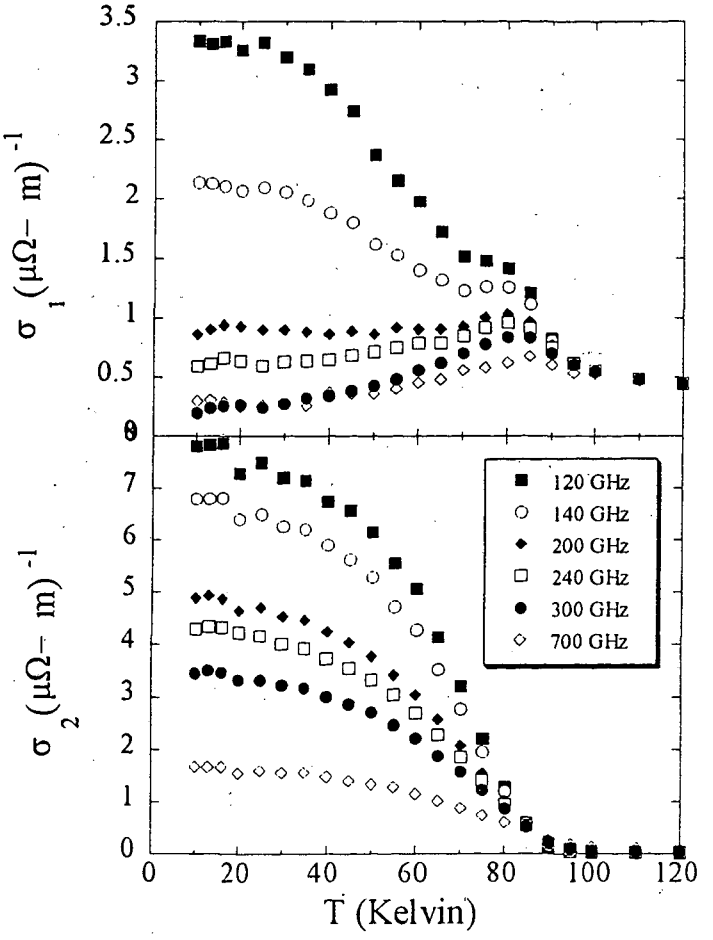

Figure 4.3: σ_1 (top panel) and σ_2 (bottom panel) for nearly optimally doped film (sample 1388)

The corresponding spectra for σ_1 are shown in figure 4.4. This data shows clearly that much of the 'action' occurs between 50 and 150 GHz. Unfortunately, this cuts through

the edge of our reliable frequency coverage. We are cautious about interpreting even the 100 GHz, data, though the low frequency $\sigma_1(T)$ behavior does match well with that seen in microwave measurements. Since the data in figure 4.3 was taken, several changes have been made in the terahertz system that should improve the lower-frequency data. Measurements will resume when we have a new optimally-doped film.

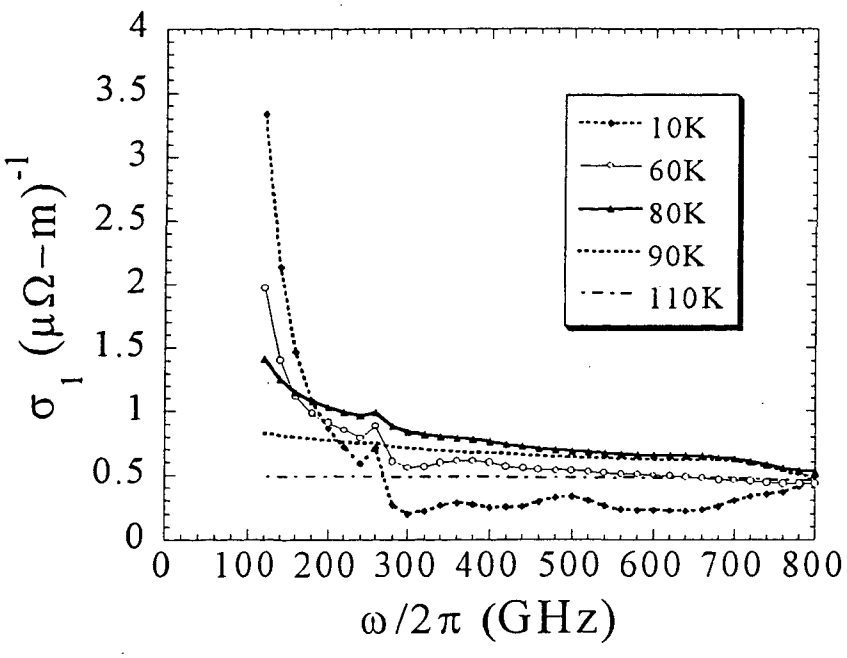

Figure 4.4: σ_1 spectra for nearly optimally doped sample (1388) at various temperatures

For completeness, we show in figure 4.5 microwave measurements of σ_1 on the single-layered thallium compound, $Tl_2Ba_2CuO_{6+\delta}$ [47]. The measurement was performed by the same group that published the figure 4.2 data. This crystal is slightly underdoped, with $T_c = 78$ Kelvin. Like the BSCCO crystal they studied, the penetration depth changes

linearly in temperature below 25 Kelvin. Such behavior exhibits itself only in the highest quality samples. The σ_1 data shows similar temperature dependence as the data on BSCCO, though the frequency dependence is slightly different. Starting at roughly 50K, we see some effect of the relaxation rate approaching the measurement frequencies, as σ_1 decreases at higher frequency.

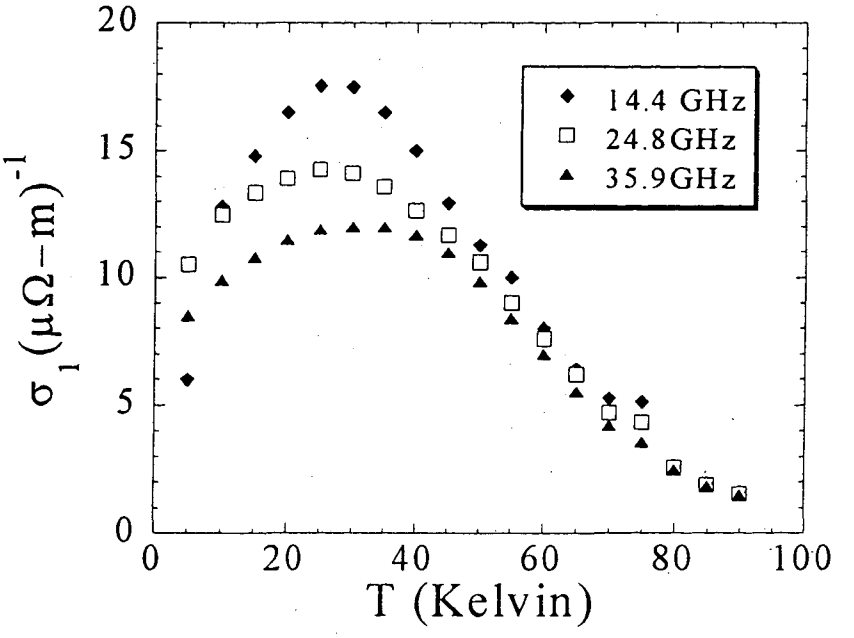

Figure 4.5: σ_1 *vs.* T on $Tl_2Ba_2CuO_{6+\delta}$ at 14.4, 24.8, and 35.9 GHz from *Broun, et. al.*

4.3 Analysis of conductivity data

As we suggested earlier, a significant fraction of spectral weight appears to reside outside the superfluid δ-function in BSCCO. The question is potentially interesting because

the behavior of the spectral weight is an excellent diagnostic of the many-body interactions. It identifies the important energy and time scales and allows us to see how they evolve as the system enters different regimes. There is potential for learning something new and important about these materials. Perhaps parts of the Fermi surface do not participate in the superconductivity. Or perhaps there exists a collective mode that pulls spectral weight out of the δ-function. Or maybe the node is cut off at some energy scale, leaving a finite region of Fermi surface even at zero temperature. Any important many-body effect influences the spectral weight, and this may be the easiest way of first detecting it.

The conductivity data from microwave measurements and our own terahertz measurements are suggestive of some anomaly in the low-temperature spectral weight. The usual suspects for a large residual conductivity are the opening of Fermi surface near the nodes due to impurities or disorder (gapless superconductivity), and the existence of grain boundaries. The first possibility leads to a T^2 dependence of the penetration depth rather than the linear dependence that has been observed in these crystals. As for the possibility of grain boundaries, the same low-temperature spectral weight anomaly can be seen in measurements of thermal conductivity at zero frequency [22], which should not be so seriously affected by grain boundaries.

The spirit of the analysis that follows is to combine the results of other experiments with our own to make a case for the spectral weight anomaly. At this time, all of the data, including our own, suffer from uncertainties that prevent basing a strong conclusion on any one of them. The microwave measurements must deal with a residual surface resistance that is difficult to distinguish from residual conductivity in the sample. They also require

an independent measurement of the penetration depth, which is always done on a different crystal. Our own measurements suffer from an increasing errors at low frequency due to diffraction effects. However, since the data presented here was taken, important improvements have been made in the technique. We now have precise position control of the sample, both in the initial placement and in correcting the movements incurred by thermal contraction of the apparatus upon cooling. We also have identified and mitigated the leakage of radiation around the sample and cryostat. Both of these modifications yield substantial improvement of the low-frequency data. Unfortunately, since these improvements, we have not had the sample necessary to study this effect (the original expired [89]).

In spite of the uncertainties associated with each experiment, microwave measurements from two groups, our own measurements, and thermal conductivity measurements all point to a large component of spectral weight outside the condensate. We are not aware of any measurements that conflict with these results. Taken together, they suggest that the anomaly is real.

We begin an analysis of the spectral weight with the microwave measurements of Lee, *et. al.* [44], which we showed in figure 4.2. The Drude form of the conductivity gives σ_1 as

$$\sigma_1 = \frac{n_q e^2}{m^*} \frac{\tau_*}{1 + (\omega \tau_*)^2}, \tag{4.2}$$

where n_q is the quasiparticle density.

Equipped only with the real part of the quasiparticle response, we cannot disentangle n_q from τ_*. However we do have additional information from the penetration depth measurements performed on the same sample. Since λ is a direct measure of the superfluid

density ($1/\mu_0\lambda^2 = n_s e^2/m$) we can use the values of $\Delta\lambda$ reported in the paper to calculate Δn_s, and hence Δn_q. Lee *et. al.* show $\lambda^2(0)/\lambda^2(T)$, which is the superfluid density normalized to its zero-temperature value. Using the clean limit relation $x_s + x_n = 1$ (where x_s and x_n are the normal and superfluid fractions), we can assume a variety of values for the zero-temperature normal fraction $x_n(0)$ and deduce the resulting $x_n(T)$.

If we assume a frequency-independent scattering rate, we can combine these pieces of information to get an idea of the residual normal fraction. By normalizing σ_1 to divide out the total spectral weight, we can write

$$(\mu_0\omega\lambda^2(0))\sigma_1(T) = x_n(T)f(\omega\tau_*), \qquad f(\omega\tau_*) \equiv \frac{\omega\tau_*}{1+(\omega\tau_*)^2}. \tag{4.3}$$

The function $f(\omega\tau_*)$ represents the frequency dependence of the quasiparticle conductivity. It depends on temperature through the scattering time τ_*. In the Drude model, $f(\omega\tau_*)$ cannot exceed 1/2, even with a frequency-dependent τ_*. The temperature dependence of this function is experimentally accessible from the σ_1 data and an assumed value of $x_n(0)$. By imposing 'reasonable' behavior on $f(\omega\tau_*)$, we can deduce rough values for the zero-temperature normal fraction.

Figure 4.6 shows $f(\omega\tau_*)$ as a function of temperature for various values for $x_n(0)$. By assuming zero normal fraction at $T = 0$, we have a clearly implausible behavior of f. As the temperature is lowered, f climbs to very large values. To bring f down to approximately 1/2 or less for all temperatures, it is necessary to assume a zero-temperature normal fraction of about 10%.

In fact the σ_1 behavior for BSCCO resembles more the behavior of YBCO when it has been deliberately doped with Ni impurities [42]. In this case, the peak is washed

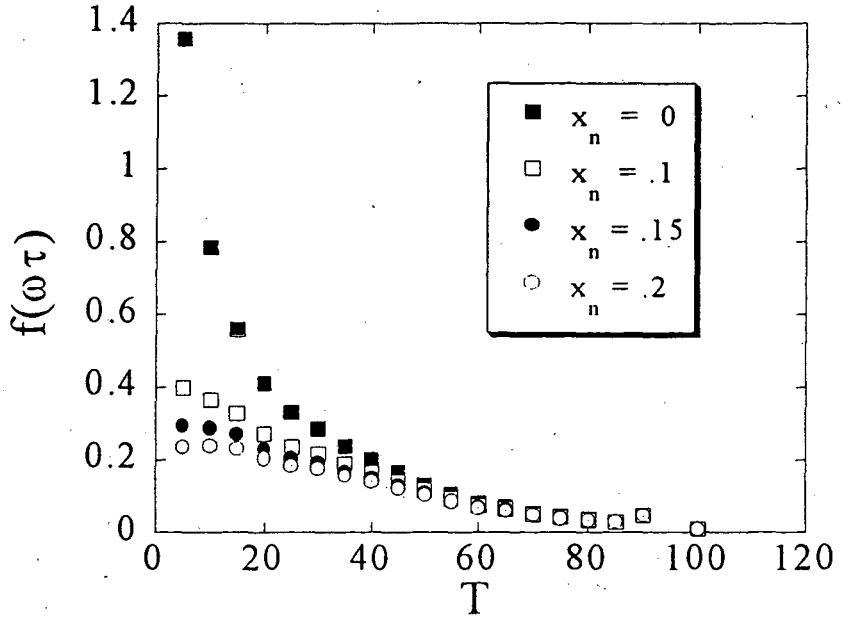

Figure 4.6: Scattering function *vs.* temperature for various values of $x_n(0)$.

out and the scattering rate reaches only about 150-200 GHz at low temperature. If we use $1/\tau_* = 2\pi \cdot 150\ GHz$, then $f(\omega\tau_*) \approx .22$, which according to figure 4.6 suggests that $x_n(0)$ is closer to 20%.

Another way to obtain an estimate of the residual normal fraction is to combine our own measurements with infrared studies. Romero, *et. al.* [50] have measured the conductivity of thin BSCCO crystals out to 3000 cm^{-1}(90 THz) using infrared transmittance. By using their data for the frequency dependence of σ_1 at 100 Kelvin, we can roughly determine the total spectral weight, $\int d\omega\sigma_1(\omega)$, without any model-dependent assumptions. To estimate the residual spectral weight we do have to make a guess for the low-frequency

extrapolation of our own spectra in figure 4.4. Using the microwave results of Lee, *et. al.* [44] and Jacobs, *et. al.* [45] as a guide, it is reasonable to estimate a roll-off at about 10 $(\mu\Omega - \mathrm{m})^{-1}$. Such an assumption leads to a residual spectral weight of 12%, in fair agreement with the estimate from the microwave data alone.

4.4 Conductivity of underdoped BSCCO

The unusual behavior in BSCCO conductivity becomes more interesting when we compare the optimally doped system to the underdoped. To our knowledge, no microwave measurements have been published on underdoped BSCCO. We have studied the conductivity in our frequency range on two underdoped samples ($T_c = 70, 72$ K) . We see yet another type of behavior. Figure 4.7 shows σ_1 vs. T at various frequencies. The conductivity shows a large peak at T_c for all frequencies, and then decreases monotonically. There is no qualitative change in behavior for different frequencies, as there is in the optimally-doped sample.

To highlight significant similarities and differences between the underdoped and the optimally-doped data, we plot the low-frequency conductivity from the optimally doped and the underdoped BSCCO on the same graph (figure 4.8). The figure brings out the important difference in scale between the previous figures. It also shows interesting similarities near T_c. In both samples, the conductivity rises as T_c is approached from above. Where the underdoped conductivity peaks, the optimally doped follows. As the conductivity falls in the underdoped sample, the optimally doped sample shows a kink before the quasiparticle lifetime effect takes over and brings the conductivity back up. As will be discussed shortly,

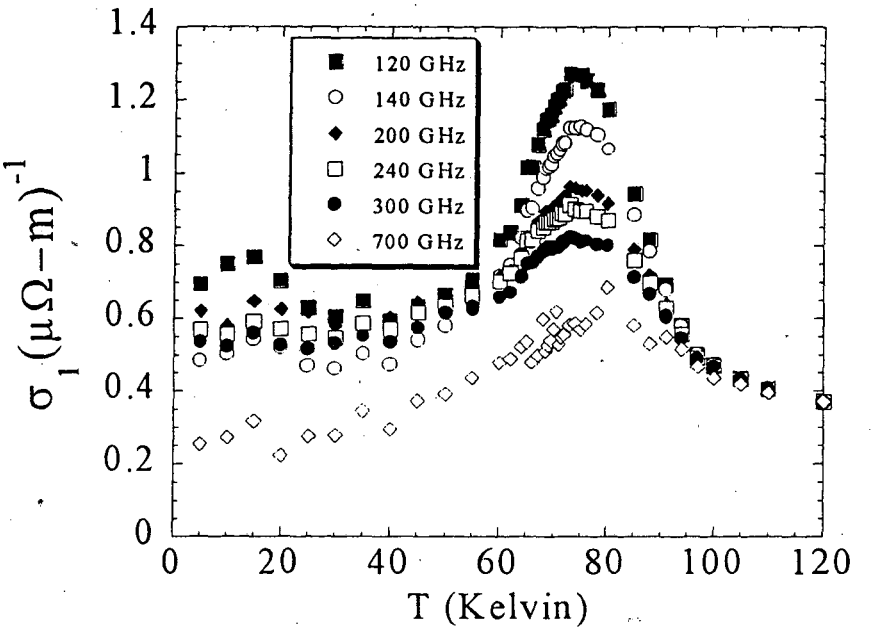

Figure 4.7: σ_1 vs. T at various frequencies for a moderately underdoped (T_c 72K) sample (1280).

the peak in the underdoped sample near T_c is due to fluctuation conductivity [49]. It appears that the fluctuation conductivity is extremely similar in the two materials, inspite of a 15K difference in transition temperatures. It is the quasiparticle contribution to the conductivity that varies so much.

Figure 4.9 show the same data as figure 4.7, plotted versus frequency rather than temperature. Above 200 GHz, the conductivity is similar in magnitude to that measured in the optimally-doped sample. In both cases, the value of the conductivity is comparable to the absolute uncertainty in our measurement, though the relative uncertainty between different temperatures is far smaller. Below 200 GHz, though, the underdoped BSCCO does not show the large increase that is seen in the optimally-doped sample.

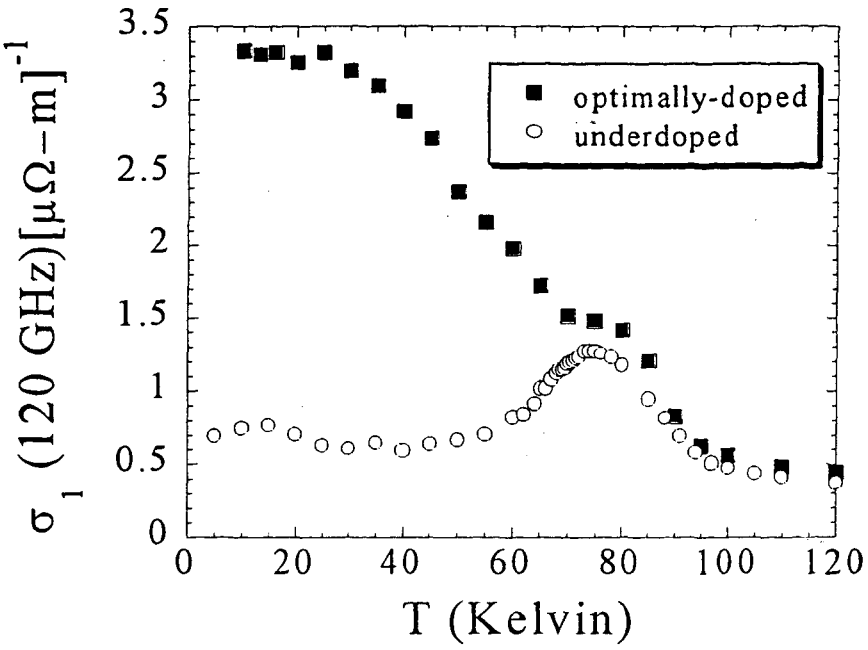

Figure 4.8: Comparison of the conductivities between the $T_c = 85K$ sample and the $T_c = 70K$ sample

The low residual value for the conductivity suggests three possible scenarios: 1) $1/\tau_*$ sweeps through our measurement frequencies; 2) the underdoped samples have a lower residual spectral weight; or 3) $1/\tau_*$ shows less of a drop than in the optimally-doped sample.

The first scenario can be virtually ruled out. Such a rapid increase in $1/\tau_*$ does not even occur in the highest-purity, untwinned crystals of YBCO [42, 51]. Furthermore, we have recently determined that the conductivity near the transition is dominated by the physics of the Kosterlitz-Thouless phase fluctuations [49], which lead to the large peak seen near T_c. The answer is more likely some combination of the second and third scenarios.

Distinguishing between scattering effects and superconducting spectral weight shifts is an important issue. In either case, there is new, interesting physics to be learned

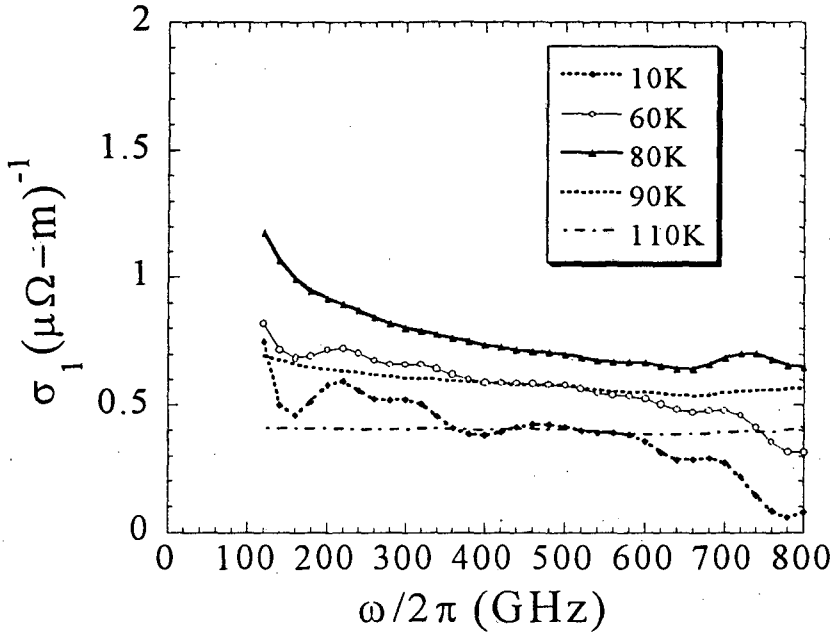

Figure 4.9: σ_1 spectra for $T_c = 72$ Kelvin underdoped BSCCO

about these materials. We would also like to understand why the underdoped system is different from the optimally-doped system. If there is a large residual spectral weight in the optimally-doped BSCCO, but not in the underdoped, what is its origin? If the effect is a fundamentally different behavior of the scattering rate, why is it different? The answer could have practical importance. The ability to reduce dissipation with proper doping could be benefit high-frequency applications, for example.

Further refinements in our technique, as well as access to a range of samples with different carrier dopings can help answer these questions. We expect that a new cryostat will aid in reducing the phase uncertainty in our conductivity measurements, which will

lead to more accurate determination of σ_1. More accurate determination of σ_1 over a wider frequency range can provide information necessary to distinguish differences in the spectral weight shifts versus changes in scattering. In addition, some of the improvements mentioned earlier will enhance the low-frequency data. Finally, we have planned collaboration with a microwave group to study the same samples over a wider frequency range.

4.5 Fermi surface

We conclude this section with a discussion of the Fermi surface geometry and the interaction with antiferromagnetic fluctuations that may be relevant to effects we have seen. Figure 4.10 depicts the Fermi surface for optimally-doped (solid lines) and underdoped (dashed lines) BSCCO, as determined by angle-resolved photoemission [52]. The nodes in the energy gap are located along the diagonal directions $(\pm\pi, \pm\pi)$. The underdoped sample, which has a T_c of 70K (like our underdoped samples) has an abbreviated Fermi surface that does not extend to the Brillouin zone edges.

Several aspects of our observations in underdoped and optimally doped systems correlate well with measurements from angle-resolved photoemission. When the sample enters the superconducting state, energy dispersion curves from photoemission experiments show a sharpening of the peak near the Fermi energy, which is attributed to an enhancement of the quasiparticle lifetime. However, this sharpening does not occur along the zone diagonals, but only away from them [29]. Interestingly, this is the same part of the Fermi surface that exists in the optimally-doped system but not in the underdoped. It is possible that this is the same effect leading to the large rise in the conductivity for the optimally

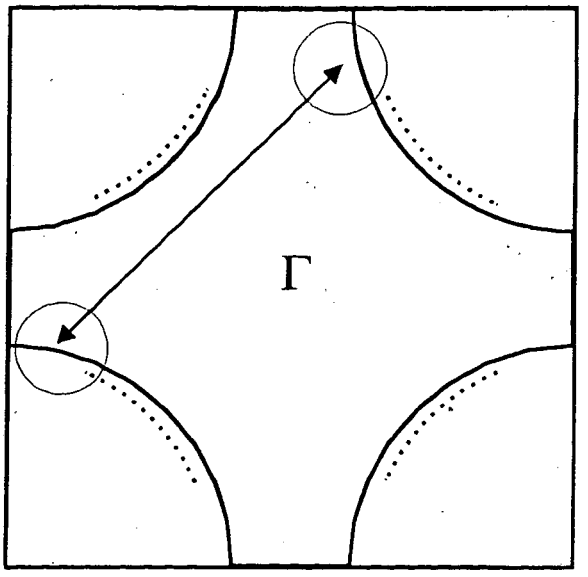

Figure 4.10: Fermi surface for optimally-doped (solid lines) and underdoped (dashed lines) BSCCO 2212. Also shown is the (π, π) momentum transfer associated with antiferromagnetic fluctuations.

doped system, but a monotonically decreasing conductivity in the underdoped material.

The mechanism behind quasiparticle scattering in the cuprates is the interaction with antiferromagnetic fluctuations [41, 53, 54]. Fermi surface dependence can arise naturally because the spectrum of fluctuations is peaked around a momentum transfer of $\mathbf{Q} = (\pi, \pi)$ [55, 56, 57]. This leads to preferential scattering on those parts of the Fermi surface that are connected via $\mathbf{Q}$ to other parts, as in figure 4.10. The creation of theses 'hot' and 'cold' spots of the Fermi surface has been studied in the normal state [55, 56, 57, 58], but little attention has been given to the superconducting state analog. The strong momentum dependence of the antiferromagnetic fluctuations could lead to highly anisotropic quasiparticle scattering at low temperature, or perhaps an even a more fundamental effect connected with the anomalously large spectral weight in the optimally-doped system. Much remains to be studied.

4.6 'Normal' state transport

In recent years the temperature-doping phase diagram of the cuprates has received much attention. For slightly underdoped materials. an additional phase exists above the superconducting transition temperature which exhibits preformed pairs and an energy gap, but no global condensation of Cooper pairs. Evidence for this phase, called the 'spin gap' or 'pseudogap' phase, exists from NMR measurements [59], infrared conductivity [60, 61, 62], and photoemission [63, 37], among others. Some of the most compelling evidence for the pseudogap comes from the photoemission measurements, which clearly show the gap formed above T_c, with the same k-dependence as the superconducting gap. The pseudogap phase exists between T_c and a crossover temperature T^*, depicted in figure 4.11. There is currently much debate about the nature of this spin-gap state, and the relation of the gap to the superconducting energy gap [65, 66].

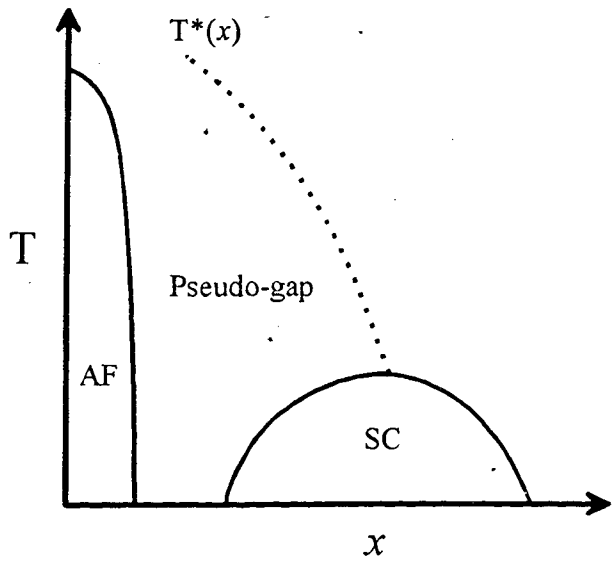

Figure 4.11: Phase diagram of the cuprate superconductors

One important piece of information about the spin-gap state is the effect of the pseudogap on charge transport. Measurements at *dc* have long revealed a deviation from the T-linear behavior of the resistivity at the crossover temperature T^* [67, 68]. A number of recent infrared measurements on underdoped BSCCO from one group have reported a large suppression of the scattering rate in the spin-gap state [69, 5]. Current theories of the pseudogap state [65, 66] suggest that the pairing is in the spin degrees of freedom only, and that the scattering rate should not be significantly altered by the presence of such a gap.

Figure 4.12 shows data from reference 69 in which they have plotted the scattering rate versus frequency for various temperatures. The sample studied in this plot is a $T_c = 67K$ underdoped crystal. They determine the scattering rate from a one-component extended Drude analysis of the conductivity. Below 1000 cm^{-1} (125 meV), they report a large suppression in the scattering rate in the spin-gap regime. The $1/\tau$ they report at 73 K has a temperature dependence very close to the superconducting state data, shown as black squares. Based on this behavior, they conclude that the scattering has been severely suppressed by the opening of the pseudogap.

Certain aspects of the case for a suppressed scattering rate warrant closer examination. In all the samples studied, the pseudogap behavior is represented only with temperatures within 6-8 degrees Kelvin of T_c, even though pseudogap regime is claimed to extend up to about 150 K in all the samples. In our own measurements of underdoped BSCCO, we have seen the onset of superconducting fluctuations at temperatures significantly higher than T_c, often 20-25 degrees higher, or 1.25 T_c [49]. It is likely that the data shown in ref. 69 is in fact in this regime of fluctuating superconductivity. Since the

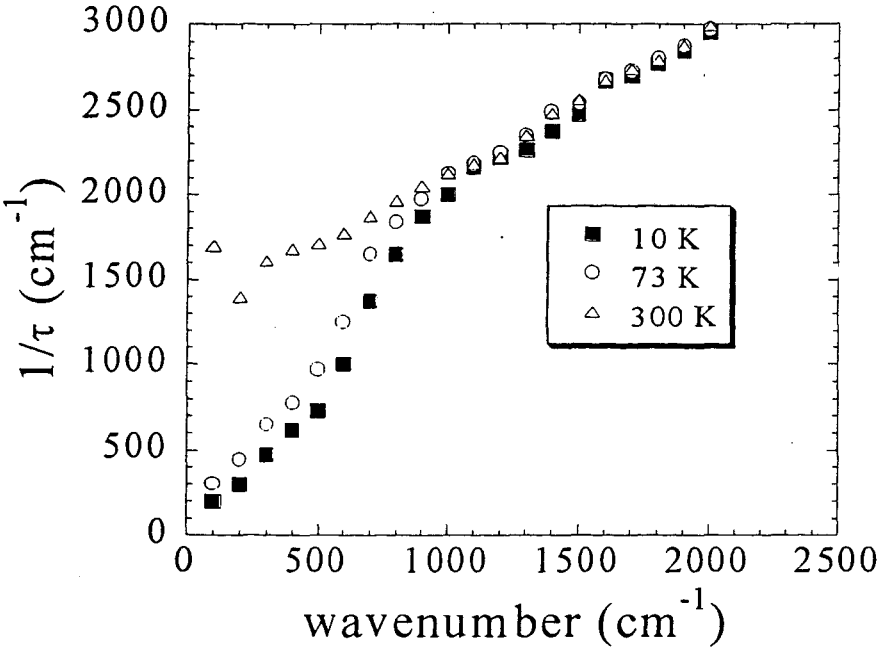

Figure 4.12: Scattering rate vs. frequency in underdoped BSCCO. The data is from reference 69 on a $T_c = 67K$ sample.

authors use a one-component Drude analysis, the development of an imaginary term in the conductivity due to superconducting fluctuations would manifest itself as a suppression in the scattering rate.

Terahertz spectroscopy provides an excellent means to study small changes in the scattering rate in the normal state. Using the extended Drude parameterization for the conductivity,

$$\sigma = \frac{ne^2}{m^*(\omega)} \frac{\tau_*(\omega)}{1 - i\omega\tau_*(\omega)}, \tag{4.4}$$

the scattering time can be measured simply through the relation $\tan\phi = \omega\tau_*(\omega)$, where ϕ is the phase of the conductivity defined by $\sigma = |\sigma|e^{i\phi}$. The dc resistivity in the normal state

exhibits a linear dependence on temperature. Thus if we plot the phase of *sigma* versus temperature, we expect to see a $1/T$ dependence for ϕ. As we cool from room temperature, ϕ should increase gradually until the superconducting transition sets in, at which time ϕ rapidly shoots up from the onset of superconductivity.

If the scattering rate shows a large depression because of the pseudogap, then we should see a significant increase in ϕ at temperatures close to 150 K or higher. Figure 4.13 shows the phase of the conductivity versus temperature at 400 GHz, expressed in units of τ_* (femtoseconds). Although we can measure the changes in τ_* sensitively, an absolute calibration is difficult due to uncertainties in the thickness and index of the substrate. We have set the phase to zero at room temperature. If the scattering rate is actually $1/\tau_* = 2\pi \cdot 9$ THz, as infrared measurements on other samples indicate [59], then the phase of all the data should be shifted upward by about 18 femtoseconds.

The figure shows the phase for a nearly optimally-doped sample, and two underdoped samples with T_c's of 70 and 42 K. Also shown is the $1/T$ dependence (solid line) expected from the *dc* resistivity. The data show very slight change in τ_* for the optimally-doped sample, and a steadily decreasing τ_* for the underdoped samples that actually goes *negative* at the lowest temperatures before the superconductivity sets in. We will discuss this shortly. In any case, two important conclusions can be drawn from the data. The first is that there is no significant lengthening in τ_* in the spin gap state, as has been reported elsewhere [69, 5]. In fact, the phase behaves *oppositely* as it would if τ_* were getting longer. Second, we can see the large growth in the phase associated with superconducting fluctuations at temperatures well above T_c. In the $T_c = 70$ K sample, the fluctuations begin at

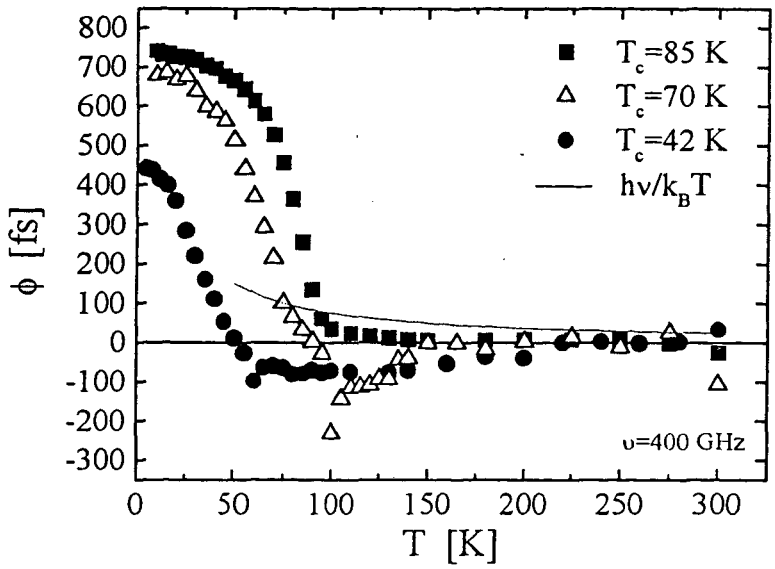

Figure 4.13: Phase (in femtoseconds) vs Temperature at 400 GHz for three samples.

about 95 Kelvin; in the $T_c = 42$ K sample, 60 Kelvin. We believe that it is the onset of such fluctuations which are giving rise to the apparent drop in $1/\tau_*$ in the infrared measurements.

It is fair to ask how we can be sure that the large increase in the phase above T_c is not in fact a lengthening in τ_*. There are two reasons. First, we observe large changes in the magnetoconductivity up to the same temperature as the onset of the phase increase. The magnetoconductivity arises because the magnetic field suppresses the superconductivity. Second, the conductivity in this temperature range is well-described by Kosterlitz-Thoulless phase fluctuations [49].

Returning to the data in the normal state, we address the question of a negative phase. The phase on the underdoped samples decreases sufficiently that even with the 18 femtosecond correction for the 300 K normalization, ϕ is still going negative. A negative

phase for the conductivity (*i.e.* negative σ_2) means that the current leads rather than lags the electric field. As we will now show, a negative σ_2 implies that there is a peak in σ_1 at higher frequency. Such a peak is generally associated with disorder.

Based on the Kramers-Kronig relations, we can show that a negative σ_2 cannot arise out of a monotonically decreasing $\sigma_1(\omega)$. The Kramers-Kronig relations for the conductivity are

$$\sigma_1(\omega) = \frac{2}{\pi} P \int_0^\infty d\omega' \frac{\omega' \sigma_2(\omega')}{\omega'^2 - \omega^2}$$

$$\sigma_2(\omega) = \frac{2\omega}{\pi} P \int_0^\infty d\omega' \frac{\sigma_1(\omega')}{\omega^2 - \omega'^2}. \tag{4.5}$$

Studying the second equation, for $\sigma_2(\omega)$, we plot $1/(\omega^2 - \omega'^2)$ (the function in the integrand along with $\sigma_1(\omega)$) in figure 4.14. We also observe that if one integrates $1/(\omega^2 - \omega'^2)$ from zero to infinity, the result is zero. In other words, a flat $\sigma_1(\omega)$ function leads to zero σ_2. The positive contribution to σ_2 comes from the part of the integral for which $\omega' < \omega$, the negative contribution from $\omega' > \omega$. For a monotonically decreasing $\sigma_1(\omega)$, then, we could replace the function $\sigma_1(\omega')$ for values of $\omega' < \omega$ with the value of σ_1 at $\omega' = \omega$ and be assured of a σ_2 that is greater than or equal to zero. Increasing the value of $\sigma_1(\omega')$ for $\omega' < \omega$ to the original value of σ_1 can only increase the value of σ_2, since that part of the integrand contributes positively to σ_2. Thus a monotonically decreasing $\sigma_1(\omega)$ cannot lead to a negative σ_2. The 'theorem' does not imply the reverse, though, that a peak in σ_1 necessarily leads to a negative σ_2.

We can see in figure 4.13 that the more underdoped sample shows more negative values for σ_2. This is not unexpected, as underdoping a sample generally increases the level

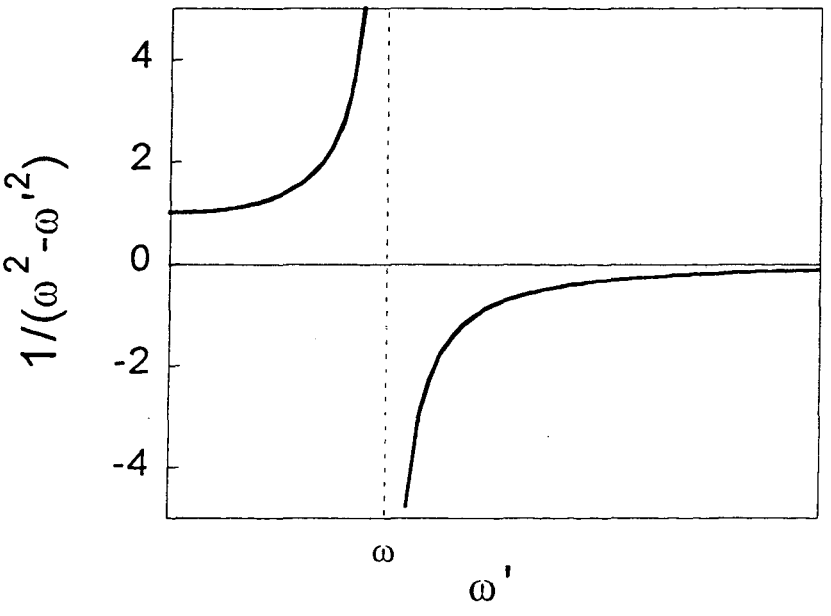

Figure 4.14: Kramers-Kronig function

of disorder. We can conclude that there is a peak in the real part of the conductivity at frequencies higher than we have measured. The unusual behavior of the phase is a result of temperature dependence of this peak. As a means for studying disorder, though, this would not be the most powerful or direct approach. It would be more fruitful to study directly σ_1 at higher frequencies, where the peak is present. Perhaps with the inevitable extension of our frequency range, this will soon be an interesting area to study.

In this chapter we have discussed measurements that utilize the phase sensitivity of the terahertz spectroscopic technique. The measurement of σ_1 in the superconducting state

and σ_2 in the normal state are basically measurements of the phase of the transmission. When the magnitude of a response function is dominated by either the real or the imaginary part, determination of the non-dominant component amounts to measuring accurately the phase of the function. A non-coherent measurement, such as conventional FTIR, cannot measure this phase directly and so cannot accurately determine the non-dominant part of the response function. Continuing improvements of our spectroscopic technique have yielded increasingly accurate data of this type, but there is still much to look forward to.

Chapter 5

C-axis Plasma Resonance

5.1 Experimental setup

Terahertz spectroscopy has generally been applied to probe the *ab*-plane of thin films. One of the advantages enjoyed by infrared techniques is the ability to study single crystals, and hence probe along the *c*-axis if the crystal is sufficiently large. Recently, we have explored a novel coupling geometry that enables us to probe along the *c*-axis of thin films [70]. The sample is placed on its side with the terahertz beam propagating along its surface, so that the sample intercepts roughly half the beam, as in figure 5.1. The polarization of the terahertz beam can be oriented in the plane of the sample, or perpendicularly to it to probe the *c*-axis. We measure the magnitude of the transmitted radiation. By comparing the throughput in the normal and superconducting states, we can observe changes in the *c*-axis dielectric properties.

Although our coupling scheme appears similar to grazing-incidence reflectivity, this appearance is deceiving because of the long wavelengths used in this experiment. The

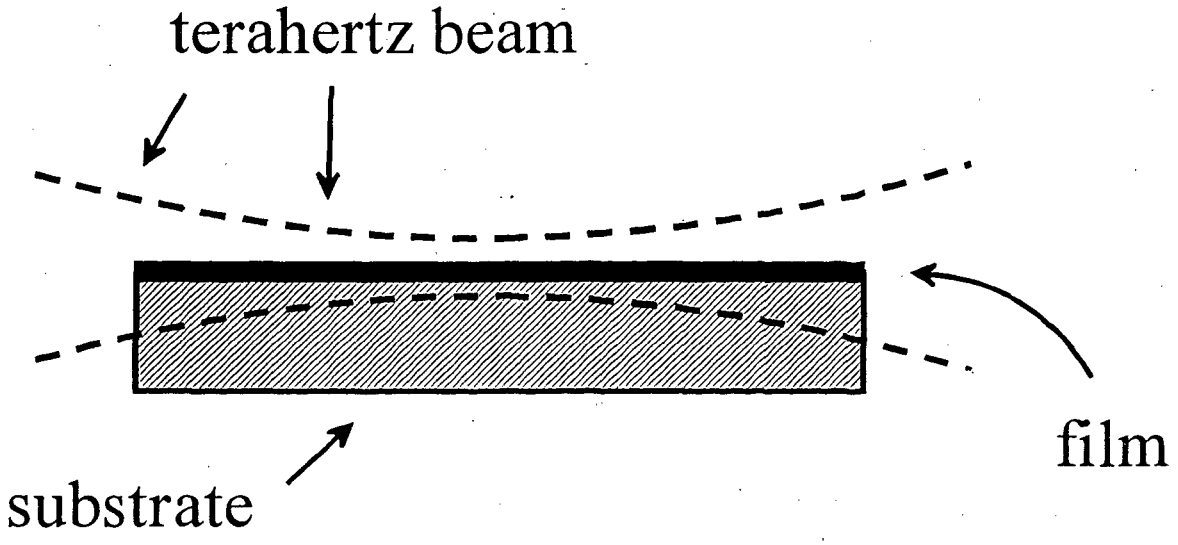

Figure 5.1: Geometry for probing the c-axis of thin films

relevant frequency span, from 100-400 GHz, translates to free-space wavelengths λ from .75-3.0 mm. The corresponding values for the Rayleigh range of our beam vary from 4 to 15 mm, which is comparable to the lateral dimension of the substrate and film. Within the Rayleigh range the radiation propagates with nearly planar wavefronts in a cylinder of diameter approximately 3λ. Because geometric optics fails within the Rayleigh range, a thin film placed in a waveguide is possibly a closer analogy to our experiment than grazing incidence reflectivity.

At present we do not have a quantitative understanding of the coupling scheme. We can gain some insight into the measurement by considering the simplest possible model: The power absorption in a thin film that intercepts an electric field $\mathbf{E_{out}}$, oriented perpendicularly to the face of the film, as in figure 5.2. Using boundary condition on the electric field displacement $\mathbf{D} = \epsilon\mathbf{E}$, we can compute the electric field inside the film and the result-

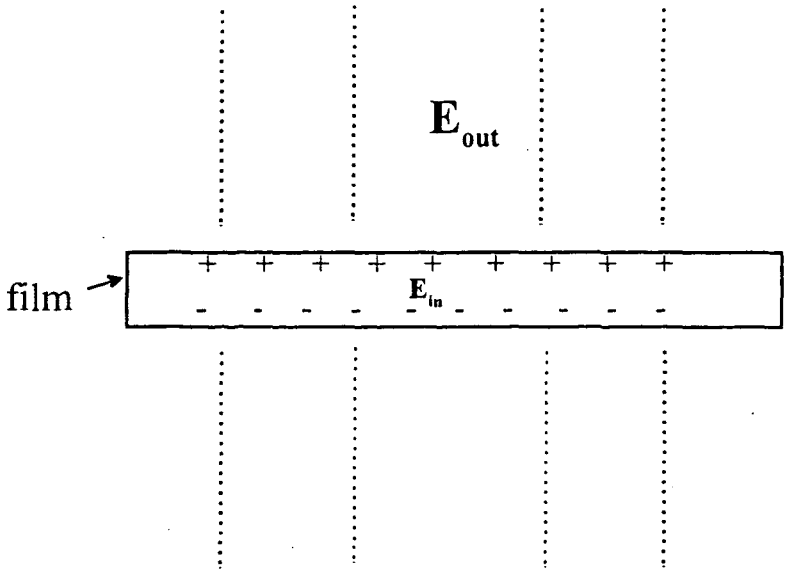

Figure 5.2: Simplified model for c-axis coupling scheme.

ing current $\mathbf{J} = \sigma_c \mathbf{E_{in}}$. Here $\mathbf{E_{in}}$ is the electric field inside the film. The power absorption is just the time average of Re $[\mathbf{J} \cdot \mathbf{E}^*]$:

$$\text{Power absorption} \quad \propto \quad < \mathbf{J} \cdot \mathbf{E}^*_{\mathbf{in}} > = < \sigma_c \mathbf{E_{in}} \cdot \mathbf{E}^*_{\mathbf{in}} >$$

$$= \text{Re} < (-i\epsilon_c)\omega \mathbf{E_{in}} \cdot \mathbf{E}^*_{\mathbf{in}} > = -i\omega \text{Re} < \epsilon_c (\mathbf{E_{out}}/\epsilon_c) \cdot (\mathbf{E}^*_{\mathbf{out}}/\epsilon_c^*) >$$

$$= -i\omega \text{Re} < (1/\epsilon_c)|\mathbf{E_{out}}|^2 > = \omega |\mathbf{E_{out}}|^2 \ \text{Im} < 1/\epsilon_c > .$$

In the second line we have assumed that the conductivity is the dominant contribution to the dielectric function ϵ_c, and we have used boundary conditions on D.

The last expression gives an appealing result. The power absorption spectrum is proportional to the frequency times the dielectric loss function Im $< 1/\epsilon_c >$. We must

stress, though, that this model is a tremendous simplification. It leaves out the substrate, the cross-sectional shape of the terahertz beam, and issues of propagation down a lossy medium. To get more quantitative information out of this measurement, it seems necessary to solve Maxwell's equations numerically for the given setup.

5.2 Application to thin films

In cuprates with relatively weak anisotropy, such as the YBCO and LSCO ($La_{2-x}Sr_xCuO_4$) systems, the complex conductivity has been measured from microwave to ultraviolet wavelengths [71] along all three axes. In the extremely anisotropic materials, such as the Bi and Tl-based superconductors, no measurements (other than our own) in the terahertz part of the spectrum have been reported. The first ab-plane measurements we have discussed in the previous two chapters. In this chapter we discuss the first c-axis experiments.

There is currently much interest in the c-axis plasma resonance of the most anisotropic cuprates, for a variety of reasons. The interaction between Cu-O planes is sufficiently weak in these materials that the system is better described by stacked planes coupled by Josephson tunneling, rather than by anisotropic Ginzburg-Landau theory [71]. The magnitude of the c-axis plasma resonance, ω_p, measures the strength of Josephson coupling between planes and places a constraint on the fraction of condensation energy that can arise from an interlayer tunneling mechanism [72]. Furthermore, the appearance of the resonance near T_c probes the onset of phase coherence in the $\hat{c}$-direction. Finally, the variation of ω_p with applied magnetic field H measures the order parameter of vortex strings [73, 74].

In single crystals of LSCO [75] and YBCO [62] the c-axis conductivity σ_c and plasma frequency ω_p have been inferred from Kramers-Kronig analysis of the infrared reflectivity, R, of a surface containing the c-axis. In these materials a sharp plasma edge appears in R upon cooling through T_c, marking the transition from a broad, incoherent σ_c in the normal state to a δ-function at $\omega = 0$. Unlike the more isotropic superconductors, the screened plasma frequency $\omega_{ps} = \omega_p/\sqrt{\epsilon_c}$ is below the gap energy, leading to extremely small damping and hence a very sharp resonance. Here ϵ_c is the background dielectric constant.

Recently, microwave cavity experiments at fixed frequencies in the 10-90 GHz range gave direct evidence for the c-axis plasmon in BSCCO in applied magnetic fields [76, 77, 78]. The presence of vortices disturbs the phase coherence between planes [73], reducing ω_p into the microwave regime. As H is varied, the resonance passes through their measurement frequency, leading to a sharp absorption peak. Although these measurements demonstrate the existence of the resonance, several questions remain unanswered. The issues of Josephson coupling energy and the onset of interlayer phase coherence, near T_c and near the vortex lattice melting transition temperature [81], all require measurement of ω_{ps} in zero and very low fields. Attempts to observe the resonance in zero-field in BSCCO [79] and in TBCO ($Tl_2Ba_2Ca_2Cu_3O_{10}$) [80] using infrared techniques have thusfar been unsuccessful, though they have placed upper bounds on $\omega_{ps}/2\pi$ of 900 GHz and 1.5 THz, respectively.

By applying our transverse coupling scheme, we have made the first observation of the c-axis BSCCO plasma resonance in zero field. Figure 5.3 shows the temperature

dependence of the power spectrum reaching the detector for two polarizations of the electric field. The sample used is our nearly-optimally doped BSCCO film with T_c of 85 Kelvin. Each spectrum has been normalized to the spectrum at 120K. Above 120K the spectra show

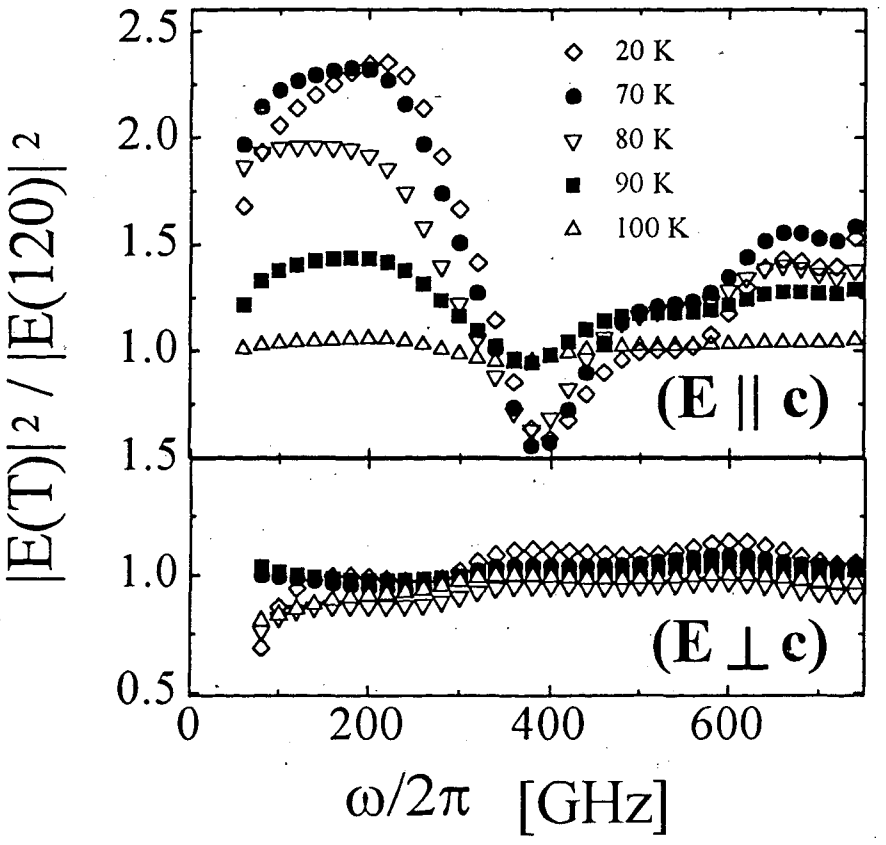

Figure 5.3: Observation of the c-axis plasmon in BSCCO. Transmitted spectra normalized to the 120K spectra. The top panel shows $\mathbf{E} \parallel \mathbf{c}$, the bottom shows $\mathbf{E}$ in the ab-plane.

relatively little temperature dependence. For $\mathbf{E} \parallel \mathbf{c}$, shown in the top panel, the spectra develop a strong step-like feature between 250 GHz and 400 GHz, near the superconducting transition temperature. Below T_c, the transmitted power at 250 GHz is nearly five times larger than at 400 GHz. The spectra for the orthogonal polarization, in which $\mathbf{E}$ lies in the

ab plane, are shown in the lower panel. There is little discernible difference in the spectra above and below T_c.

The properties of the spectral feature shown in Fig. 5.3 lead us to identify it as the *c*-axis plasma resonance. Its frequency scale, temperature dependence, and polarization dependence are all consistent with this identification. Furthermore, the spectra resemble a 'plasma edge,' as seen in near-normal incidence reflectivity of metals. Using this analogy, we would place the zero crossing of ϵ_1 (and hence ω_{ps}) at approximately 300 GHz.

Lacking a detailed model of the coupling scheme, we cannot yet extract a temperature dependence and width of the plasma resonance. To convey qualitatively the temperature dependence of the resonance, we use the size of the transmission step between 340 and 120 GHz. This is plotted in figure 5.4 as the solid symbols. The strength of the *c*-axis plasma resonance measures the phase stiffness between planes. The phase stiffness within the planes is measured by σ_{2ab}, though at higher temperatures the measurement is somewhat influenced by quasiparticle conductivity. To compare the development of phase coherence along the *c*-direction to that in the *ab*-plane, we show the imaginary part of the *ab*-plane conductivity σ_{2ab}, normalized to its value at 10K, for frequencies of 100 and 540 GHz. These are shown as the open symbols.

It is interesting to note that the onset of phase coherence along the *c*-direction occurs simultaneously with superconducting fluctuations in the *ab*-plane. The 100 GHz σ_2 begins to increase closer to the resistively-measured transition temperature of 85 K than does the 540 GHz data. This difference reflects the frequency dependence of phase fluctuations of the order parameter [49]. The *c*-axis feature begins to rise rapidly along

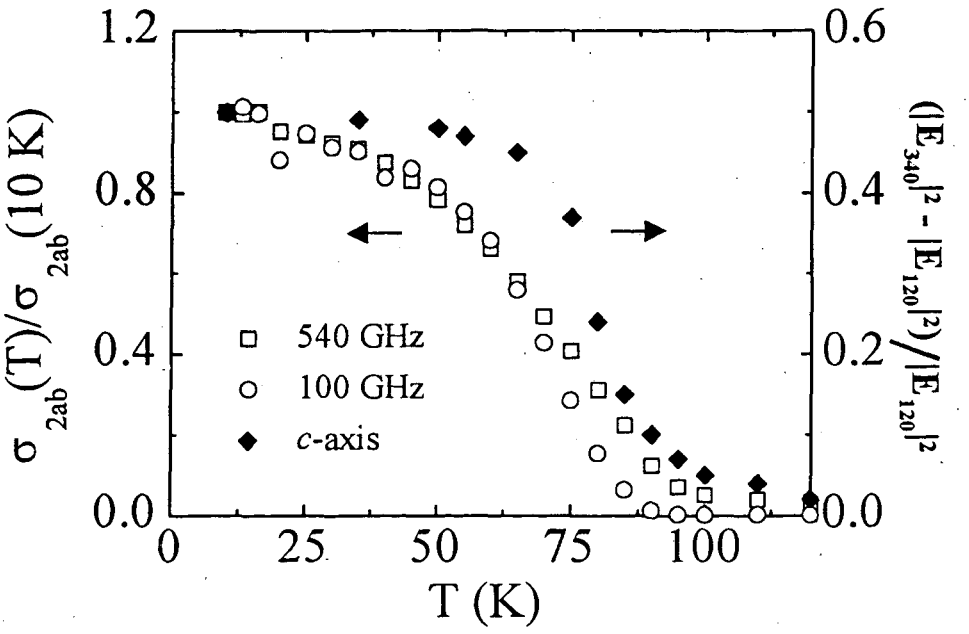

Figure 5.4: Comparison of the temperature dependence of the c-axis plasma resonance to the ab-plane charge dynamics. Solid symbols (right hand scale) show the size of the transmission step between 340 GHz and 120 GHz for $\mathbf{E} \parallel \mathbf{c}$. Open circles, and squares (left-hand scale) are σ_{2ab} at 100 and 540 GHz, respectively, normalized to their values at 10K.

with the higher frequency data, suggesting that order parameter fluctuations are coupled between planes from the moment they first appear.

Another point to note is the flatness of the c-axis feature at low temperatures. The c-axis coherence decreases very slowly until 50-60 Kelvin, where it drops rapidly. The superfluid density in the ab-plane, on the other hand, shows a more rapid decrease at low temperatures. Similar behavior, though less pronounced, has been reported in LSCO and YBCO systems [82, 83, 84]. The decrease in n_{sab} with temperature is widely understood as a consequence of nodes in the gap function. Thermally-excited quasiparticles contribute to

intralayer conduction, pulling spectral weight out of the superfluid. The comparatively slow decrease in the c-axis coherence suggests that interlayer transport of these quasiparticles is somehow inhibited. This observation is consistent with models in which single-particle tunneling between planes is suppressed by the formation of a Luttinger liquid state [85], or by band structure effects [86].

We have established that we can use this technique to couple to c-axis dielectric properties, though much work remains to develop it into a quantitative measurement. Numerical studies of the coupling scheme may shed light on the nature of the measurement. Another approach is to study films of known dielectric properties, on a variety of substrates. Perhaps we can develop an empirical understanding of the physics of this measurement. The ability to measure c-axis properties in this frequency range could be a valuable tool in the study of high-T_c superconductors, artificial structures [87], and a host of other novel materials.

Chapter 6

Future directions

Possible directions for future research divide into two areas: extension of current projects, and more long-ranged goals. Most of the current projects still have major questions remaining open. In the vortex state, we would like to use our understanding of the BSCCO electrodynamics to revisit the vortex state of YBCO. Field-cooled experiments may shed light on whether the response is in fact dominated by d-wave electrodynamics, modulated by a non-equilibrium vortex density. We would also like to understand better why the $H^{1/2}$ behavior persists to such high temperatures. In zero field, many improvements are already under way or in place to enhance the accuracy and frequency coverage of the data. More accurate measurements are required to distinguish between changes in τ and changes in the total quasiparticle spectral weight. It is also desirable to attain a more controlled range of sample doping levels, particularly in the optimally-doped direction. Another improvement in the sample growth is on the horizon: it appears that these BSCCO films can now be grown twin-free on a new $LaAlO_3$ substrate. Untwinned samples will improve the quality

of the low-temperature σ_1 experiments. Finally, we hope that the c-axis measurements are only in their infancy. Much remains to understand in this potentially exciting probe.

More long-ranged goals will of course involve branching out to new materials. Terahertz photons are well suited to studying many-body interactions. Relevant energy scales often fall into this range; the question is, what can we do to enhance our ability to study them?

I believe that studying the anisotropic response of novel systems is becoming increasingly interesting. Whenever the Fermi surface is highly anisotropic, and there is a strong momentum dependence to the electron interactions, the electronic properties may show large variation around the Fermi surface. The ability to resolve the response in different directions could provide information that is rarely available from low-energy optical probes. Several occasions arose in our high-T_c studies that called for probing the anisotropic response. Nonlinear response to intense terahertz fields [88] is one example. Another example is current studies of the scattering rate. There is considerable variation in the scattering rate around the Fermi surface. The problem is that these materials show fourfold rotational symmetry, making all linear properties fully isotropic.

There are basically two ways we can probe the anisotropy in such systems: nonlinear experiments, and the Hall effect. We have some experience with both in our group. Pump-and-probe experiments with a high-intensity terahertz apparatus is within reach and potentially very powerful. The nonlinear response is sensitive to anisotropy even if the underlying lattice shows fourfold symmetry.

The Hall effect does not give angle-resolved data, but it can provide information

useful for understanding phenomena dependent upon the anisotropic structure of the Fermi surface, such as electronic scattering behavior. It is an experiment we can do now, but the effects are quite small and difficult to resolve through the noise. But we have an overdue improvement in our apparatus that could help: extending to higher frequency. Even with photoconductive switches, good terahertz signal can be produced up to four terahertz [2]. Since Hall effects tend to be easier to measure at higher frequency, such a boost may be all we need to make fruitful Hall studies. Hopefully, photoconductive switches with higher frequency ranges will be available commercially. If not, I believe that this improvement could be made in our own microlab with a few months effort by one student. I believe that such an expansion would be an important boost for studying both high-T_c materials and other novel systems such as Ruthenates and Manganates.

Bibliography

[1] J.G. Bednorz and K.A. Muller, "Possible high-T_c superconductivity in the Ba-La-Cu-O system," Zeitschrift fur Physik B **64**, 189-93 (1986).

[2] D. Grischkowsky, "An ultrafast optoelectronic THz beam system: applications to time-domain spectroscopy," Optics and Photonics News **3**, 21-8 (1992).

[3] Q. Wu and X.-C. Zhang, "Free-space electro-optic sampling of terahertz beams," Applied Physics Letters **67**, 3523-5 (1995).

[4] A. Nahata, A.S. Weling, and T.F. Heinz, "A wideband coherent terahertz spectroscopy system using optical rectification and electro-optic sampling," Applied Physics Letters **69**, 2321-3 (1996).

[5] A.V. Puchkov, D.N. Basov, and T. Timusk, "The pseudogap state in high-T_c superconductors: an infrared study," Journal of Physics: Condensed Matter **8**, 10049-82 (1996).

[6] See, for example, Michael Tinkham, **Introduction to Superconductivity**, McGraw-Hill, New York, NY, 1996.

[7] S.K. Yip and J.A. Sauls, "Nonlinear Meissner Effect in CuO Superconductors," Physical Review Letters **69**, 2264-7 (1992).

[8] D.Xu, S.K. Yip, and J.A. Sauls, "Nonlinear Meissner effect in unconventional superconductors," Physical Review B **51**, 16233-53 (1995).

[9] Chandu Karadi, Doctoral Thesis, U.C. Berkeley Physics Department, 1995.

[10] M.C. Nuss and J. Orenstein in **Millimeter and Submillimeter Spectroscopy of Solids**, ed. by G. Gruner, Springer-Verlag, New York, NY (to be published).

[11] Beth Parks, Doctoral Thesis, U.C. Berkeley Physics Department, 1995.

[12] D.H. Auston, "Picosecond optoelectronic switching and gating in Silicon," Applied Physics Letters **26**, 101-3 (1975).

[13] D. Grischkowsky, "Nonlinear generation of subpicosecond pulses of THz electromagnetic radiation by optoelectronics-Application to time-domain spectroscopy," in **Frontiers in Nonlinear Optics**, H. Walther, N. Koroteev, and M.O. Scully, Eds. Philadelphia, PA: Inst. of Physics, 1993.

[14] Y. Liu, S-G Park, and A.M. Weiner, *IEEE Journal of Selected Topics in Quantum Electronics*, **2**, 709, (1996).

[15] John D. Kraus, **Electromagnetics, 4th ed.**, McGraw-Hill, New York, NY, 1992.

[16] E.R. Brown, F.W. Smith, and K.A. Mcintosh, "Coherent millimeter-wave generation by heterodyne conversion in low-temperature-grown GaAs photoconductors,", Journal of Applied Physics **73**, 1480-4 (1993).

[17] Robert C. Richardson and Eric N. Smith, **Experimental Techniques in Condensed Matter Physics at Low Temperatures**, Addison-Wesley, Redwood City, CA, 1988.

[18] K. Krishana, J.M. Harris, and N.P. Ong, "Quasiparticle mean free path in $YBa_2Cu_3O_7$ measured by the thermal Hall conductivity," Physical Review Letters **75**, 3529-32 (1995).

[19] Branko P. Stojković and Oriol T. Valls, "Nonlinear supercurrent response in anisotropic superconductors," Physical Review B **51**, 6049-58 (1995).

[20] Nathan Newman and W. Gregory Lyons, "High-Temperature Superconducting Microwave Devices: Fundamental Issues in Materials, Physics, and Engineering," Journal of Superconductivity **6**, 119-59 (1993).

[21] M. Golosovsky, M. Tsindlekht, and D. Davidov, "High-frequency vortex dynamics in $YBa_2Cu_3O_7$," Superconductor Science and Technology **9**, 1-15 (1996).

[22] K. Krishana, N.P. Ong, Q. Li, G.D. Gu, and N. Koshizuka, "Plateaus Observed in the field profile of thermal conductivity in the superconductor $Bi_2Sr_2CaCu_2O_8$," Science **277**, 83-5 (1997).

[23] B. Parks, S. Spielman, J. Orenstein, D.T. Nemeth, F. Ludwig, J. Clarke, P. Merchant, and D.J. Lew, "Phase-sensitive measurements of vortex dynamics in the terahertz domain," Physical Review Letters **74**, 3265-8 (1995).

[24] J.I. Gittleman and B. Rosenblum, Physical Review Letters **16**, 734 (1966); Journal of Applied Physics **39**, 1617 (1968).

[25] V.M. Vinokur, V.B. Geshkenbein, M.V. Feigel'man, and G. Blatter, "Scaling of the Hall resistivity in high-T_c superconductors," Physical Review Letters **71**, 1242 (1993).

[26] Ping Ao and David J. Thouless, "Berry's phase and the Magnus force for a vortex line in a superconductor," Physical Review B **49**, 13271(1994).

[27] J.N. Eckstein and I. Bozovic, Annual Reviews of Materials Science **25**, 679 (1995).

[28] R. Mallozzi, J. Orenstein, J.N. Eckstein, and I. Bozovic, "High-frequency electrodynamics of $Bi_2Sr_2CaCu_2O_{8+\delta}$: nonlinear response in the vortex state," Physical Review Letters **81**, 1485-8 (1998).

[29] D.S. Marshall, D.S. Dessau, D.M. King, C.-H. Park, A.Y. Matsuura, Z.-X. Shen, W.E. Spicer, J.N. Eckstein, and I. Bozovic, "Angle-resolved photoemission spectroscopy study of $Bi_2Sr_2CaCu_2O_{8+\delta}$ thin films," Physical Review B **52**, 12548-51 (1995).

[30] M.W. Coffey and J.R. Clem, "Unified theory of effects of vortex pinning and flux creep from the RF surface impedance of type-II superconductors," Physical Review Letters **67**, 386-9 (1991).

[31] C.J. van der Beek, V.B. Geshkenbein, and V.M. Vinokur, "Linear and nonlinear AC response in the superconducting mixed state," Physical Review B **48**, 3393-403 (1993).

[32] P. Martinoli, P. Fluckiger, V. Marsico, P.K. Srivistava, C. Leemann, and J.L. Gavilano, "Vortex Dynamics in $YBa_2Cu_3O_7$ films," Physica B **165-166**, 1163-4 (1990).

[33] J.T. Kucera, T.P. Orlando, G. Virshup, and J.N. Eckstein, "Magnetic-field and temperature dependence of the thermally activated dissipation in thin films of $Bi_2Sr_2CaCu_2O_{8+\delta}$," Physical Review B **46**, 11004-13 (1992).

[34] John Bardeen, "Two-fluid model of superconductivity," Physical Review Letters **1**, 399-400 (1958).

[35] G.E. Volovik, "Superconductivity with lines of GAP nodes: density of states in the vortex," Journal of Experimental and Theoretical Physics Letters **58**, 469-73 (1993).

[36] D.S. Dessau, Z.-X. Shen, D.M. King, D.S. Marshall, L.W. Lombardo, P.H. Dickinson, A.G. Loeser, J. DiCarlo, C.-H. Park, A. Kapitulnik, and W.E. Spicer, "Key features in the measured band structure of $Bi_2Sr_2CaCu_2O_8$: flat bands at E_F and Fermi surface nesting," Physical Review Letters **71**, 2781-4 (1993).

[37] H. Ding, M.R. Norman, J.C. Campuzano, M. Randeria, A.F. Bellman, T. Yokoya, T. Takahashi, T. Mochiku, and K. Kadowaki, "Angle-resolved photoemission spectroscopy study of the superconducting gap anisotropy in $Bi_2Sr_2CaCu_2O_8$," Physical Review B **54**, R9678-81 (1996).

[38] O. Fischer, C. Renner, I. Maggio-Aprile, A. Erb, E. Walker, B. Revaz, and J.-Y. Genoud, "Tunneling spectroscopy and STM observation of vortices on high temperature superconductors, " Physica C **282-287**, 315-8 (1997).

[39] M.C. Nuss, P.M. Mankiewich, M.L. O'Malley, and E.H. Westerwick, "Dynamic Conductivity and 'Coherence Peak' in $YBa_2Cu_3O_7$ Superconductors," Physical Review Letters **66**, 3305-8 (1991).

[40] D.A. Bonn, P. Dosanjh, R. Liang, and W.N. Hardy, "Evidence for Rapid Suppression of Quasiparticle Scattering below T_c in $YBa_2Cu_3O_{7-\delta}$," Physical Review Letters **68**, 2390-93(1992).

[41] D.A. Bonn, Ruixing Liang, T.M. Riseman, D.J. Baar, D.C. Morgan, Kuan Zhang, P. Dosanjh, T.L. Duty, A. MacFarlane, G.D. Morris, J.H. Brewer, and W.N. Hardy, "Microwave determination of the quasiparticle scattering time in $YBa_2Cu_3O_{6.95}$," Physical Review B **47**, 11314-28 (1993).

[42] D.A. Bonn, S. Kamal, Kuan Zhang, Ruixing Liang, D.J. Baar, E. Klein, and W.N. Hardy, "Comparison of the influence of Ni and Zn impurities on the electromagnetic properties of $YBa_2Cu_3O_{6.95}$," Physical Review B **50**, 4051-63 (1994).

[43] S. Spielman, Beth Parks, J. Orenstein, D.T. Nemeth, Frank Ludwig, John Clarke, Paul Merchant, and D.J. Lew, "Observation of the Quasiparticle Hall effect in Superconducting $YBa_2Cu_3O_{7-\delta}$," Physical Review Letters **73**, 1537-40 (1994).

[44] Shih-Fu Lee, D.C. Morgan, R.J. Ormeno, D. Broun, R.A. Doyle, J.R. Waldram, and K. Kadowaki, "a-b plane microwave surface impedance of a high-quality $Bi_2Sr_2CaCu_2O_8$ single crystal," Physical Review Letters **77**, 735-8 (1996).

[45] T. Jacobs, S. Sridhar, Qiang Li, G.D. Gu, and N. Koshizuka, "In-Plane and ĉ-Axis Microwave Penetration Depth of $Bi_2Sr_2CaCu_2O_{8+\delta}$ Crystals," Physical Review Letters **75**, 4516-9 (1995).

[46] Patrick A. Lee, "Localized States in a d-wave superconductor," Physical Review Letters **71**, 1887-90 (1993).

[47] D.M. Broun, D.C. Morgan, R.J. Ormeno, S.F. Lee, A.W. Tyler, A.P. Mackenzie, and J.R. Waldram, "In-plane microwave conductivity of the single-layer cuprate $Tl_2Ba_2CuO_{6+\delta}$," Physical Review B **56**, R1143-6 (1997).

[48] T. Dahm, "Anisotropy of the quasiparticle damping in the high-T_c superconductors $Bi_2Sr_2CaCu_2O_8$ and $YBa_2Cu_3O_{6.9}$ as seen from angle-resolved photoemission experiments," Physical Review B **54**, 10150-4 (1996).

[49] J. Corson, R. Mallozzi, J. Orenstein, J. Eckstein, and I. Bozovic, "The vanishing of phase coherence in underdoped BSCCO," to be published.

[50] D.B. Romero, C.D. Porter, D.B. Tanner, L. Forro, D. Mandrus, L. Mihaly, G.L. Carr, and G.P. Williams, "Quasiparticle Damping in $Bi_2Sr_2CaCu_2O_8$ and $Bi_2Sr_2CuO_6$," Physical Review Letters **68**, 1590-3 (1992).

[51] S. Kamal, Ruixing Liang, A. Hosseini, D.A. Bonn, and W.N. Hardy, unpublished (http://xxx.lanl.gov/abs/cond-mat/9803292).

[52] D.S. Dessau, D.S. Marshall, A.G. Loeser, C.-H. Park, A.Y. Matsuura, Z.-X. Shen, P. Fournier, A. Kapitulnik, K. Kishio, J. Eckstein, and I. Bozovic, "Evolution of the electronic structure with doping in $Bi_2Sr_2CaCu_2O_{8+\delta}$ - Angle-resolved photoemission results," Journal of Electron Spectroscopy and Related Phenomena **78**, 167-70 (1996).

[53] P.J. Hirschfeld, W.O. Putikka, and D.J. Scalapino, "Microwave Conductivity of d-Wave Superconductors," Physical Review Letters **29**, 3705-8 (1993).

[54] S.M. Quinlan, D.J. Scalapino, and N. Bulut, "Superconducting quasiparticle lifetimes due to spin-fluctuation scattering," Physical Review B **49**, 1470-3 (1994).

[55] A. Carrington, A.P. Mackenzie, C.T. Lin, and J.R. Cooper, "Temperature dependence of the Hall angle in single crystal $YBa_2(Cu_{1-x}Co_x)_3O_{7-\delta}$," Physical Review Letters **69**, 2855-8 (1992).

[56] B. Stojkovic and D. Pines, "Anomalous Hall effect in $YBa_2Cu_3O_7$," Physical Review Letters **76**, 811-4 (1996).

[57] Branko P. Stojkovic and David Pines, "Theory of the optical conductivity in the cuprate superconductors," Physical Review B **56**, 11931-41 (1997).

[58] I.B. Ioffe and A.J. Millis, unpublished (http://xxx.lanl.gov/abs/cond-mat/9803292).

[59] W.W. Warren Jr., R.E. Walstedt, G.F. Brennert, R.J. Cava, R. Tycko, R.F. Bell, and G. Dabbagh, "Cu spin dynamics and superconducting precursor effects in planes above T_c in $YBa_2Cu_3O_{6.7}$," Physical Review Letters **62**, 1193-6 (1989).

[60] J. Orenstein, G.A. Thomas, A.J. Millis, S.L. Cooper, D. Rapkine, T. Timusk, L.F. Schneemeyer, and J.V. Waszczak, "Frequency- and temperature-dependent conductivity in $YBa_2Cu_3O_{6+x}$ crystals," Physical Review B **42**, 6342-62 (1990).

[61] L.D. Rotter, Z. Schlesinger, R.T. Collins, F. Holtzberg, C. Field, U.W. Welp, G.W. Crabtree, JZ. Kiu, Y. Fang, K.G. Vandervoort, and S. Fleshler, "Dependence of the infrared properties of single-domain $YBa_2Cu_3O_{7-y}$ on Oxygen content," Physical Review Letters **67**, 2741-4 (1991).

[62] C.C. Homes, T. Timusk, R. Liang, D.A. Bonn, and W.N. Hardy, "Optical conductivity of c-axis-oriented $YBa_2Cu_3O_{6.70}$: evidence for a pseudogap," Physical Review Letters **71**, 1645-8 (1993).

[63] D.S. Marshall, D.S. Dessau, A.G. Loeser, C.-Y. Park, A.Y. Matsuura, J.N. Eckstein, I. Bozovic, P. Fournier, A. Kapitulnik, W.E. Spicer, and Z.-X. Shen, "Unconventional electronic structure evolution with hole doping in $Bi_2Sr_2CaCu_2O_{8+\delta}$: Angle-resolved photoemissin results," Physical Review Letters **76**, 4841-4 (1996).

[64] H. Ding, M.R. Norman, T. Yokoya, T, Takeuchi, M. Randeria, J.C. Campuzano, T. Takahashi, T. Mochiku, and K. Kadowaki, "Evolution of the Fermi surface with carrier concentration in $Bi_2Sr_2CaCu_2O_{8+\delta}$," Physical Review Letters **78**, 2628-31 (1997).

[65] Xiao-Gang Wen and Patrick A. Lee, "Theory of Underdoped Cuprates," Physical Review Letters **76**, 503-6 (1996).

[66] V.J. Emery, S.A. Kivelson, and O. Zachar, "Spin-gap proximity effect mechanism of high-temperature superconductivity," Physical Review B **56**, 6120-47 (1997).

[67] B. Bucher, P. Steiner, J. Karpinski, E. Kaldis, and P. Wachter, "Influence of the spin gap on normal state transport in $YBa_2Cu_4O_8$," Physical Review Letters **70**, 2012-5 (1993).

[68] B. Batlogg, H.Y. Hwang, H. Takagi, R.J. Cava, H.L. Kao, and J. Kwo, "Normal state phase diagram of $(La, Sr)_2CuO_4$ from charge and spin dynamics," Physica C **235-240**, 130-3 (1994).

[69] A.V. Puchkov, P. Fournier, D.N. Basov, T. Timusk, A. Kapitulnik, and N.N. Kolesnikov, "Evolution of the pseudogap state of high-T_c superconductors with doping," Physical Review Letters **77**, 3212-5 (1996).

[70] R. Mallozzi, J. Corson, J. Orenstein, J.N. Eckstein, and I. Bozovic, "Terahertz conductivity and c-axis plasma resonance in $Bi_2Sr_2CaCu_2O_{8+\delta}$," to be published in Journal of Physics and Chemistry of Solids.

[71] For a review see S. Tajima, in Superconductivity Review, ed. by P. Kumar (Gordon and Breach), to be published.

[72] P.W. Anderson, "Interlayer tunneling mechanism for high-T_c superconductivity," Science **268**, 1154-5 (1995).

[73] L.N. Bulaevskii, M.P. Maley, and M. Tachiki, "Low-frequency magneto-optical properties of Josephson-coupled superconductors," Physical Review Letters **69**, 801-4 (1995).

[74] A.E. Koshelev, "Plasma resonance and remaining Josephson coupling in the 'Decoupled vortex liquid phase' in layered superconductors," Physical Review Letters **77**, 3901-4 (1996).

[75] K. Tamasaku, Y. Nakamura, and S. Uchida, "Charge dynamics across the CuO_2 planes in $La_{2-x}Sr_xCuO_4$," Physical Review Letters **69**, 1455-8 (1992).

[76] O.K.C. Tsui, N.P. Ong, Y. Matsuda, Y.F. Yan, and J.B. Peterson, "Sharp magnetoabsorption resonances in the vortex state of $Bi_2Sr_2CaCu_2O_{8+\delta}$," Physical Review Letters 73, 724-7 (1994).

[77] Y. Matsuda, M.B. Gaifullin, K. Kumagai, K. Kadowaki, and T. Mochiku, "Collective Josephson plasma resonance in the vortex state of $Bi_2Sr_2CaCu_2O_{8+\delta}$," Physical Review Letters **75**, 4512-5 (1995).

[78] O.K.C. Tsui, N.P. Ong, and J.B. Peterson, "Excitation of the Josephson plasma mode in $Bi_2Sr_2CaCu_2O_{8+\delta}$," Physical Review Letters **76**, 819-22 (1996).

[79] S. Tajima, G.D. Gu, S. Miyamoto, A. Odagawa, and N. Koshizuka, "Optical evidence for strong anisotropy in the normal and superconducting states in $Bi_2Sr_2CaCu_2O_{8+z}$," Physical Review B **48**, 16164-7 (1993).

[80] J. Schützmann, H.S. Somal, A.A. Tsvetkov, D. van der Marel, G.E.J. Coops, N. Koleshnikov, Z.F. Ren, J.H. Wang, E. Brück, and A.A. Menovsky, "Experimental Test of the Inter-Layer Pairing Models for High-T_c Superconductivity Using Grazing Incidence Infrared Reflectometry," Physical Review B **55**, 11118-21 (1997).

[81] Y. Matsuda, M.B. Gaifullin, K. Kumagai, M. Kosugi, and K. Hirata, "Interlayer phase coherence in the vortex state of $Bi_2Sr_2CaCu_2O_{8+\delta}$ probed by Josephson plasma resonance," Physical Review Letters **78**, 1972-5 (1997).

[82] C.C. Homes, T. Timusk, D.A. Bonn, R. Liang, and W.N. Hardy, "Optical properties along the c-axis of $YBa_2Cu_3O_{6+\delta}$, for x = .50to.95: Evolution of the pseudogap," Physica C **254**, 265-80 (1995).

[83] T. Shibauchi, H. Kitano, K. Uchinokura, A. Maeda, T. Kimura, and K. Kishio, "Anisotropic penetration depth in $La_{2-x}Sr_xCuO_4$," Physical Review Letters **72**, 2263-6 (1994).

[84] J.H. Kim, H.S. Somal, M.T. Czyzyk, D. van der Marel, A. Wittlin, A.M. Gerrits, V.H.M. Duijn, N.T. Hien, and A.A. Menovsky, "Strong Damping of the c-axis plasmon in high-T_c cuprate superconductors," Physica C **247**, 297-308 (1995).

[85] P.W. Anderson, "The Theory of Superconductivity," Physica C **185-189**, 11-6 (1991).

[86] T. Xiang and J.M Wheatley, "c-axis superfluid resonse of copper oxide superconductors," Physical Review Letters **77**, 4632-5 (1996).

[87] J.N. Eckstein, I. Bozovic, and G.F. Virshup, "Atomic layer-by-layer engineering of high-T_c materials and heterostructure devices," MRS Bulletin **19**, 44-50 (1994).

[88] J. Orenstein, J. Bokor, E. Budiarto, J. Corson, R. Mallozzi, I. Bozovic, and J.N. Eckstein, "Nonlinear Electrodynamics in Cuprate Superconductors," Physica C **282-287**, 252-5 (1997).

[89] Sorry about that, Frank!

Appendix A

Drude response in the time domain

The time-dependent form discussed in section 2.2 is the Drude response to a step-function electric field. The reason this is the appropriate form is that the 'instantaneous' creation of carriers by the laser pulse in a *dc* electric field is akin to starting with the carriers zero electric field, and then suddenly turning on a constant field. The time-domain Drude conductivity is the Fourier transform of $\sigma(\omega)$:

$$\sigma(t-t') \propto \int_{-\infty}^{\infty} d\omega e^{i\omega(t-t')} \frac{1}{1-i\omega\tau}. \tag{A.1}$$

Performing the contour integration (the pole is at $\omega = 1/\tau$), we find $\sigma(t-t') = \theta(t-t')e^{-(t-t')/\tau}$, where $\theta(t-t')$ is the step function. Plugging this time-domain conductivity kernal into the response to a step-function electric field, we find

$$J(t) = \int_0^{\infty} dt' \sigma(t-t')E \propto \tau(1-e^{-t/\tau}), \tag{A.2}$$

which is the form used in equation 2.1.

Appendix B

Sample treatment

We describe in this appendix one of the 'nitty-gritty' details of the sample treatment, solely for the sake of documenting it. The problem is dealing with a glue of silver polish that is embedded on the back of the substrates. The glue is a necessary part of the growth process that enables good thermal contact. We must remove this glue without harming the delicate film on the other side, or else we will have to title our papers 'High-Frequency Electrodynamics of Silver Epoxy.'

To make life difficult, the superconducting film cannot be touched or placed into contact with any water. Unless, of course, we wish to write about '101 Uses for Dead BSCCO.' We can already write the first chapter on that one [89].

The procedure is as follows. The film is protected with a thick layer of photoresist. We have used AZ4330 until now, but it has come to our attention that this is not an ideal choice because of possible moisture content. The photoresist is spun on at about 2000 revolutions per second with a spinner. Sometimes the spinning process is repeated for good

measure. The film and photoresist are then baked in a 90 degree (centigrade) oven for 30-45 minutes to let it harden. The coat should not flake.

The film is now safe and ready for abuse. To get the silver glue off the back, we use a standard optics polishing powder available from any optics shop. The powders are particles that come in various sizes, from a micron or so to tens of microns. We use 35 micron powder. The powder is mixed with a little mineral oil to form a thick slurry, and set on a microscope slide. One needs very little slurry. The sample is then place film side up (epoxy side down) on the slide and slurry, and gently rubbed around with the finger placed on top of the sample, maintaining as uniform contact as possible. A protective rubber glove is worn for psychological benefit. The substrate is rubbed around gently in the slurry for about ten minutes or so, checking the progress of the epoxy as we go. The job is done when no trace of the epoxy can be seen. The substrate will look a little hazy from the rough polish. At our wavelengths, this level of roughness is not important. If a smoother substrate is desired, one can then use a finer powder for the slurry.

The remaining slurry is then wiped off, and the back of the substrate cleaned with acetone and methanol. We learned the hard way the photoresist should not be left on indefinitely, because if it develops, it ruins the film [89].

Appendix C

Data Core Dump

This appendix is a compilation of large quantities of conductivity data. The data has not been processed to cut out error points from dividing by zero, nor has it been cut off at the experimentally valid limits. It should be interpreted by the informed reader only!

C.1 Sample 1388 - nearly optimally doped, $T_c = 85K$

C.1.1 Spectra

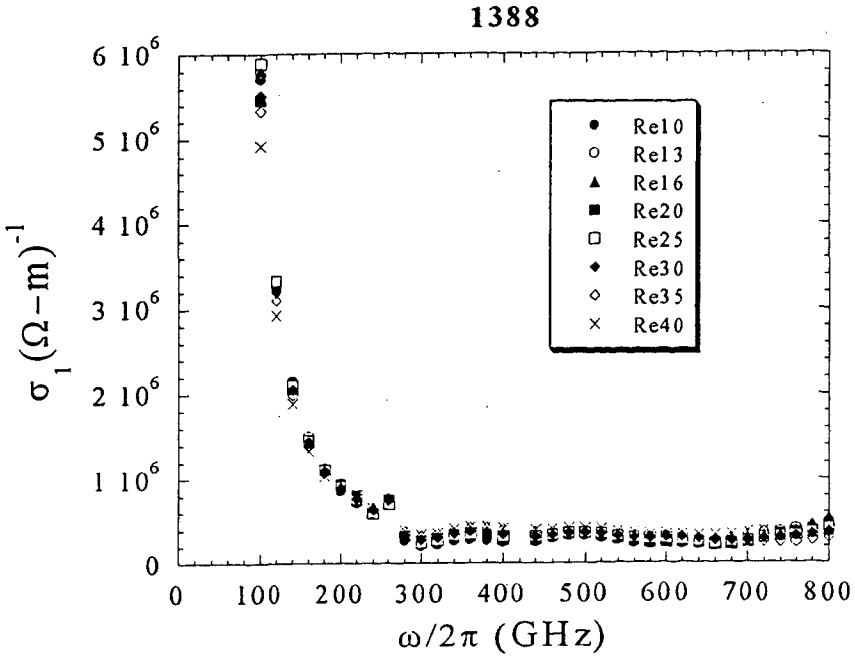
1388
6 10^6
5 10^6
4 10^6
3 10^6
2 10^6
1 10^6
0
σ_1 (Ω−m)^-1
0
100
200
300
400
500
600
700
800
ω/2π (GHz)
Re10
Re13
Re16
Re20
Re25
Re30
Re35
Re40

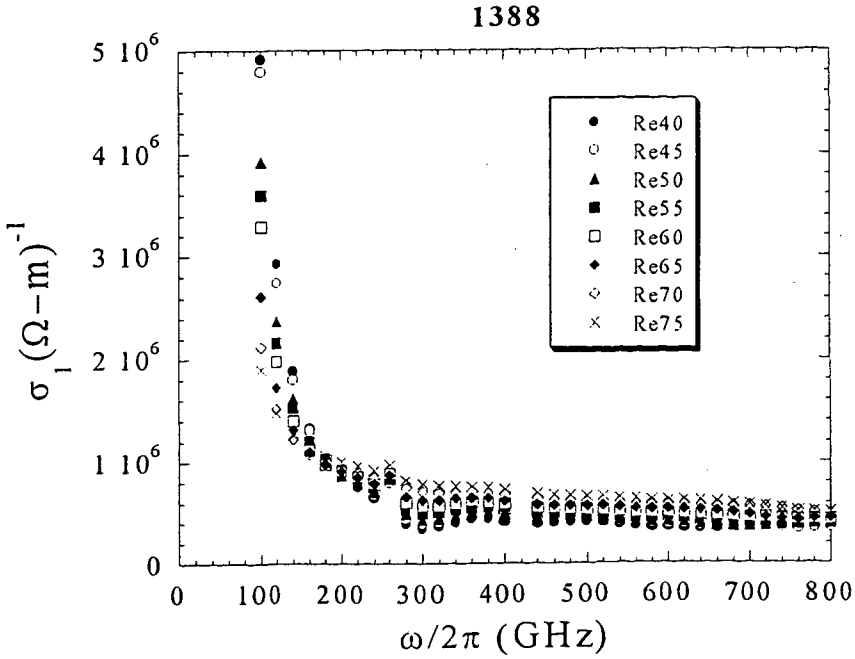
1388
5 10^6
4 10^6
3 10^6
2 10^6
1 10^6
0
σ_1 (Ω−m)^-1
0
100
200
300
400
500
600
700
800
ω/2π (GHz)
Re40
Re45
Re50
Re55
Re60
Re65
Re70
Re75

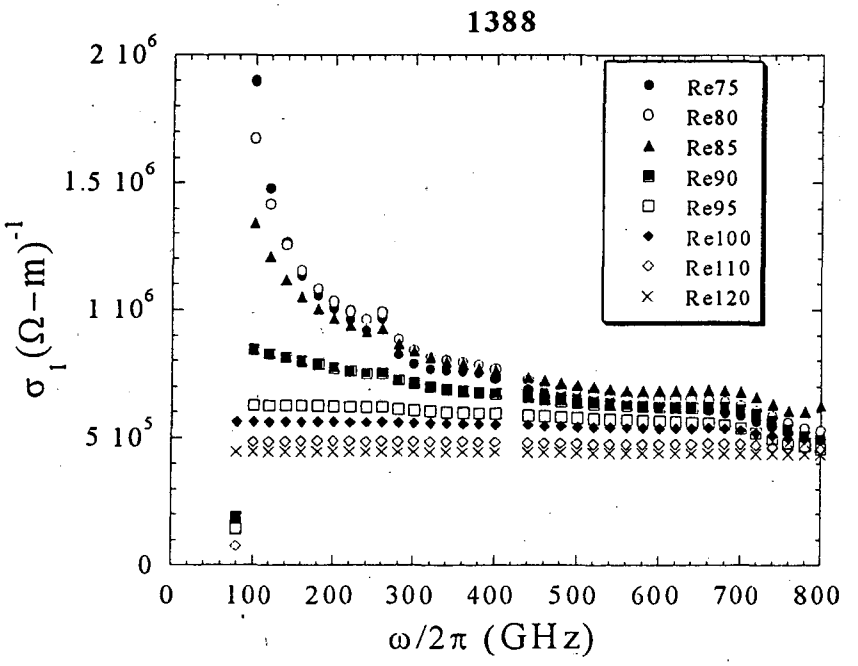
1388
2 10^6
1.5 10^6
1 10^6
5 10^5
0
σ_1 (Ω−m)^-1
0
100
200
300
400
500
600
700
800
ω/2π (GHz)
Re75
Re80
Re85
Re90
Re95
Re100
Re110
Re120

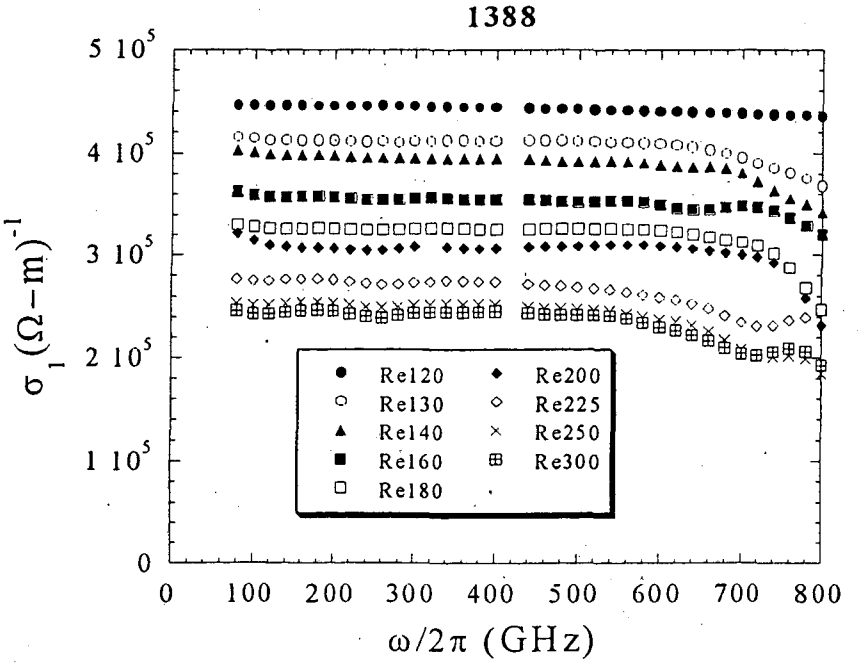
1388
5 10^5
4 10^5
3 10^5
2 10^5
1 10^5
0
σ_1 (Ω−m)^-1
0
100
200
300
400
500
600
700
800
ω/2π (GHz)
Re120
Re130
Re140
Re160
Re180
Re200
Re225
Re250
Re300

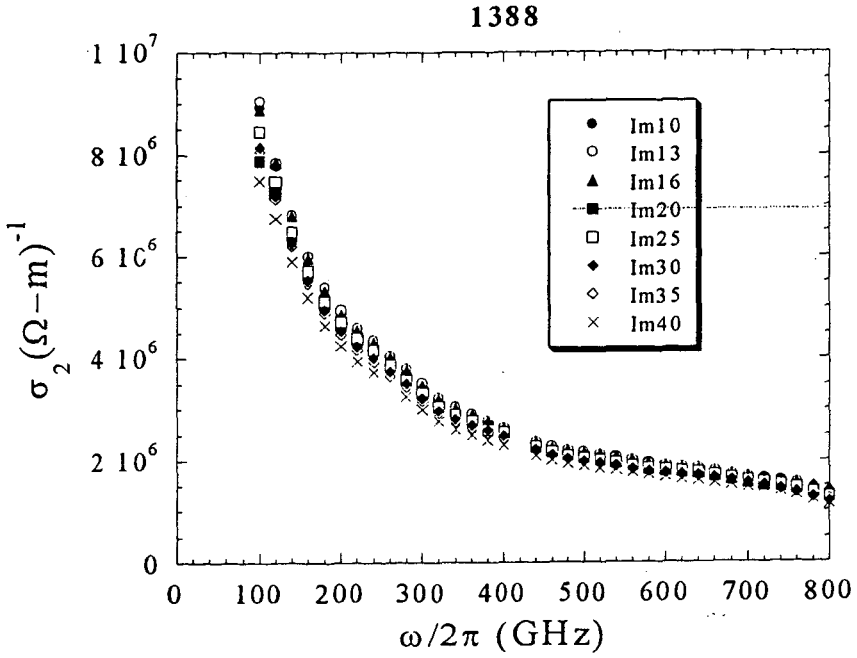
1388
1 10^7
8 10^6
6 10^6
4 10^6
2 10^6
0
σ2(Ω−m)^-1
0
100
200
300
400
500
600
700
800
ω/2π (GHz)
Im10
Im13
Im16
Im20
Im25
Im30
Im35
Im40

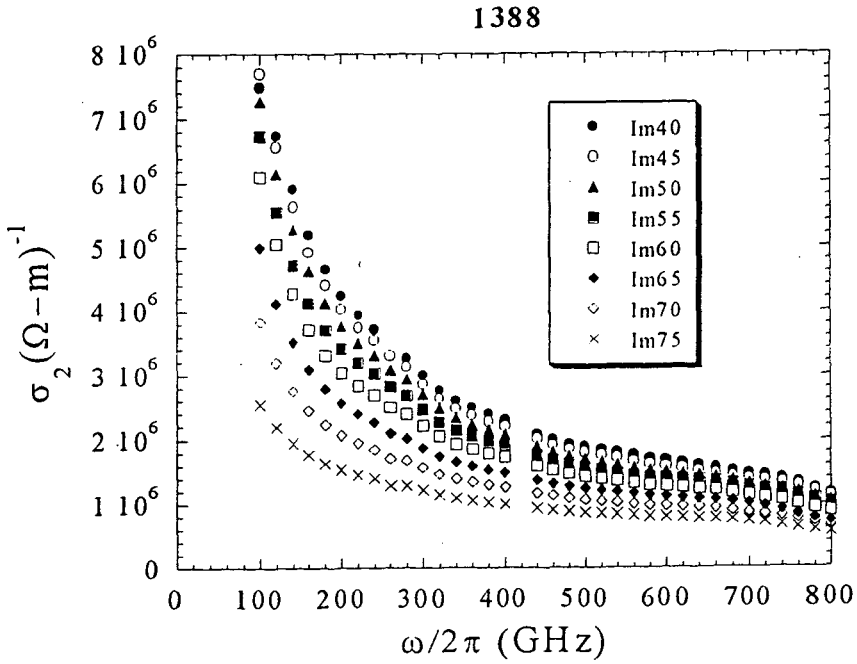
1388
8 10^6
7 10^6
6 10^6
5 10^6
4 10^6
3 10^6
2 10^6
1 10^6
0
σ2(Ω−m)^-1
0
100
200
300
400
500
600
700
800
ω/2π (GHz)
Im40
Im45
Im50
Im55
Im60
Im65
Im70
Im75

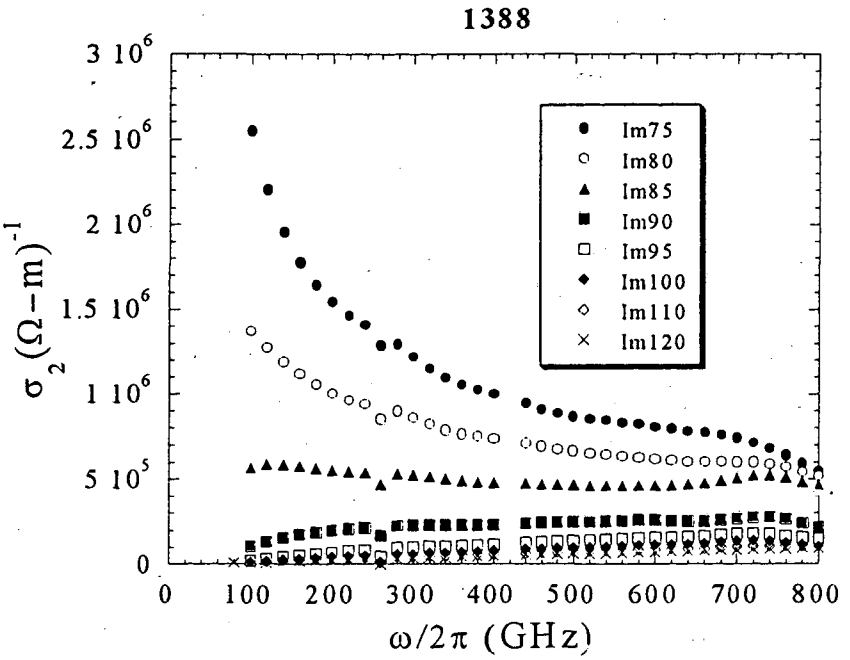
1388
3 10^6
2.5 10^6
2 10^6
1.5 10^6
1 10^6
5 10^5
0
σ2 (Ω−m)^-1
0
100
200
300
400
500
600
700
800
ω/2π (GHz)
Im75
Im80
Im85
Im90
Im95
Im100
Im110
Im120

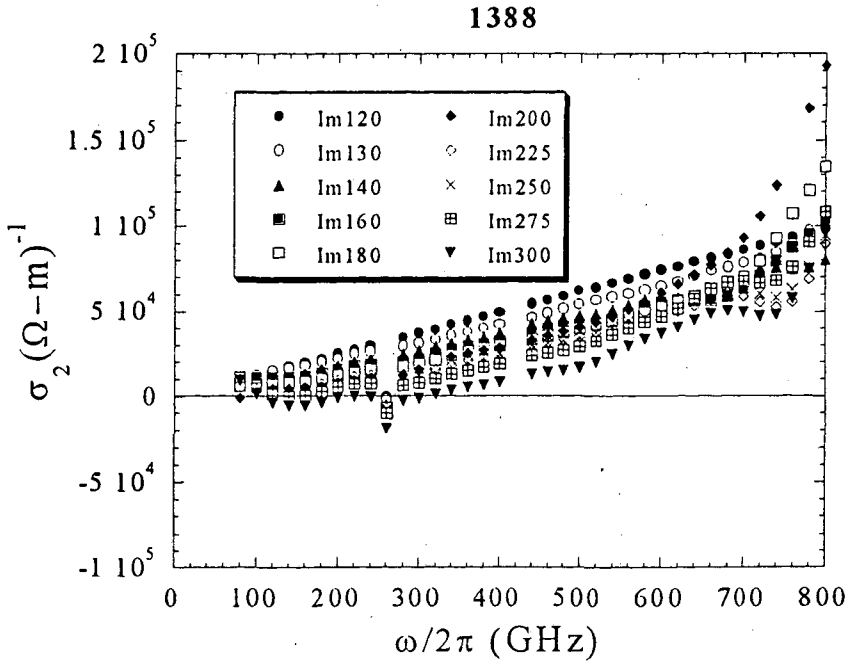
1388
2 10^5
1.5 10^5
1 10^5
5 10^4
0
-5 10^4
-1 10^5
σ2 (Ω−m)^-1
0
100
200
300
400
500
600
700
800
ω/2π (GHz)
Im120
Im130
Im140
Im160
Im180
Im200
Im225
Im250
Im275
Im300

C.1.2 Temperature Dependence

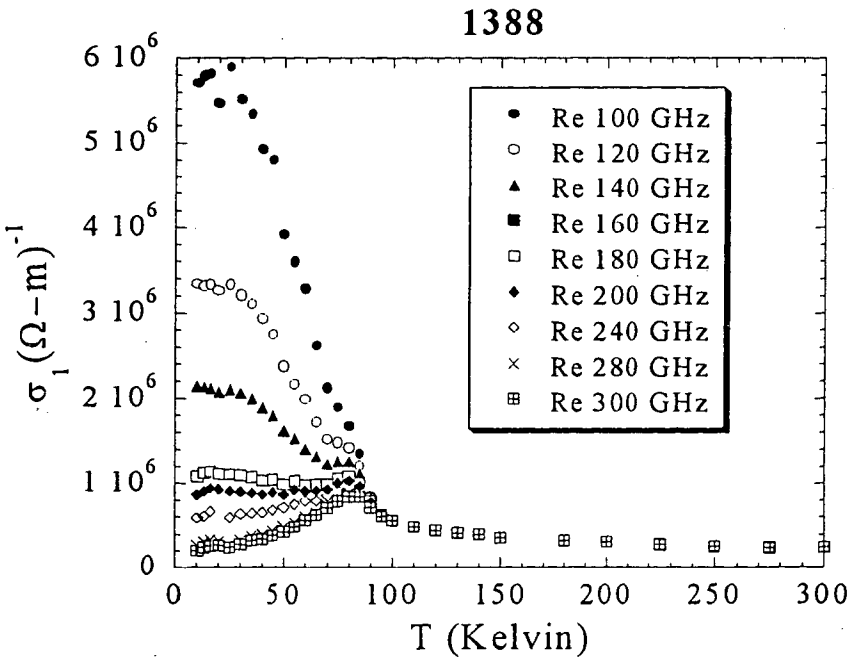

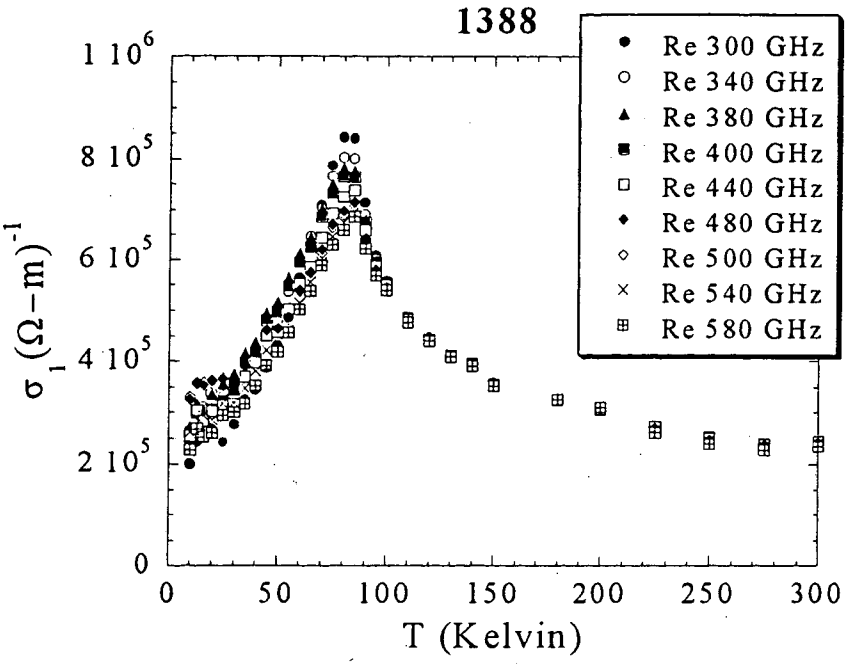
1388
Re 300 GHz
Re 340 GHz
Re 380 GHz
Re 400 GHz
Re 440 GHz
Re 480 GHz
Re 500 GHz
Re 540 GHz
Re 580 GHz
σ1 (Ω−m)−1
1 10^6
8 10^5
6 10^5
4 10^5
2 10^5
0
0
50
100
150
200
250
300
T (Kelvin)

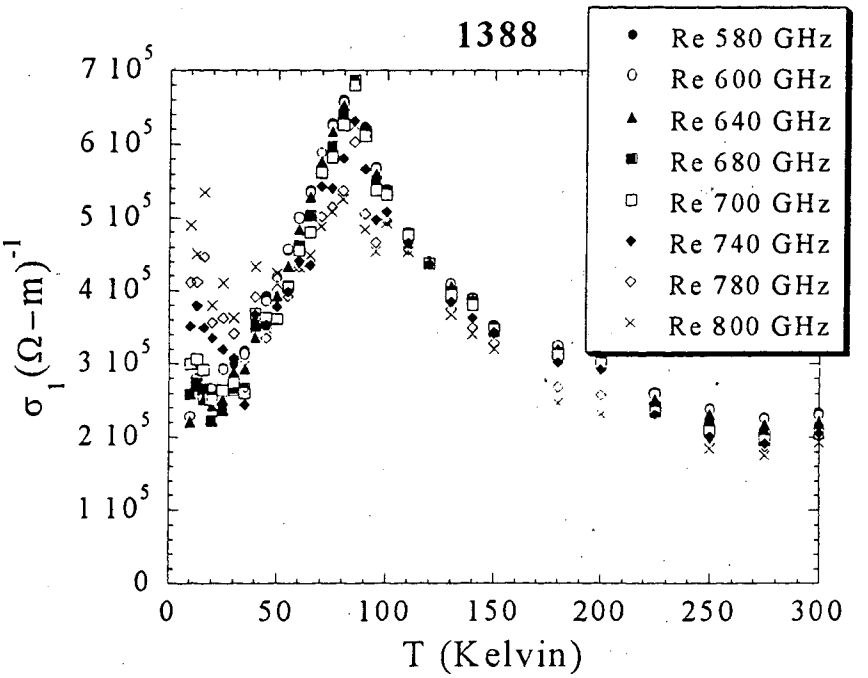
1388
Re 580 GHz
Re 600 GHz
Re 640 GHz
Re 680 GHz
Re 700 GHz
Re 740 GHz
Re 780 GHz
Re 800 GHz
σ1 (Ω−m)−1
7 10^5
6 10^5
5 10^5
4 10^5
3 10^5
2 10^5
1 10^5
0
0
50
100
150
200
250
300
T (Kelvin)

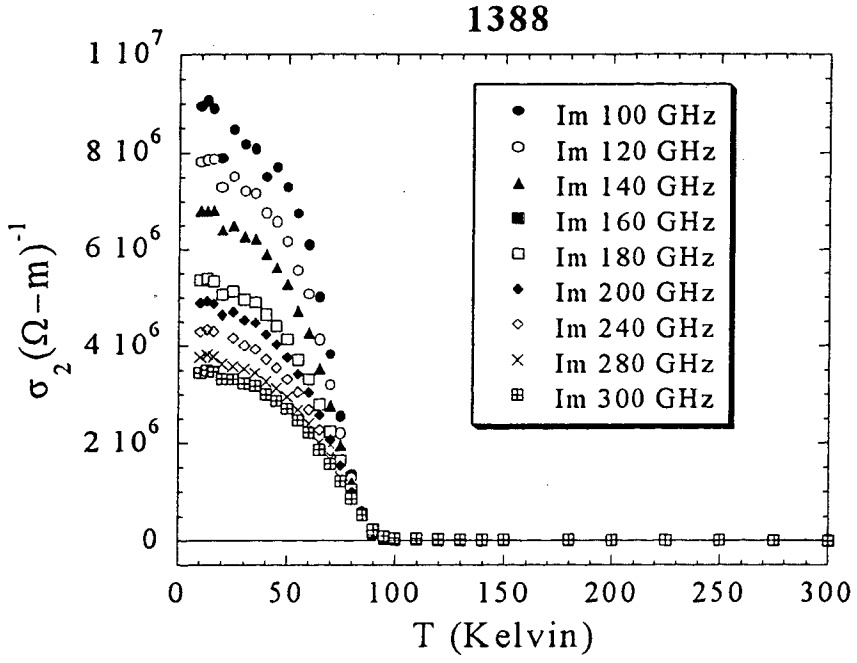
1388
1 10^7
8 10^6
6 10^6
4 10^6
2 10^6
0
σ2 (Ω−m)^-1
0
50
100
150
200
250
300
T (Kelvin)
Im 100 GHz
Im 120 GHz
Im 140 GHz
Im 160 GHz
Im 180 GHz
Im 200 GHz
Im 240 GHz
Im 280 GHz
Im 300 GHz

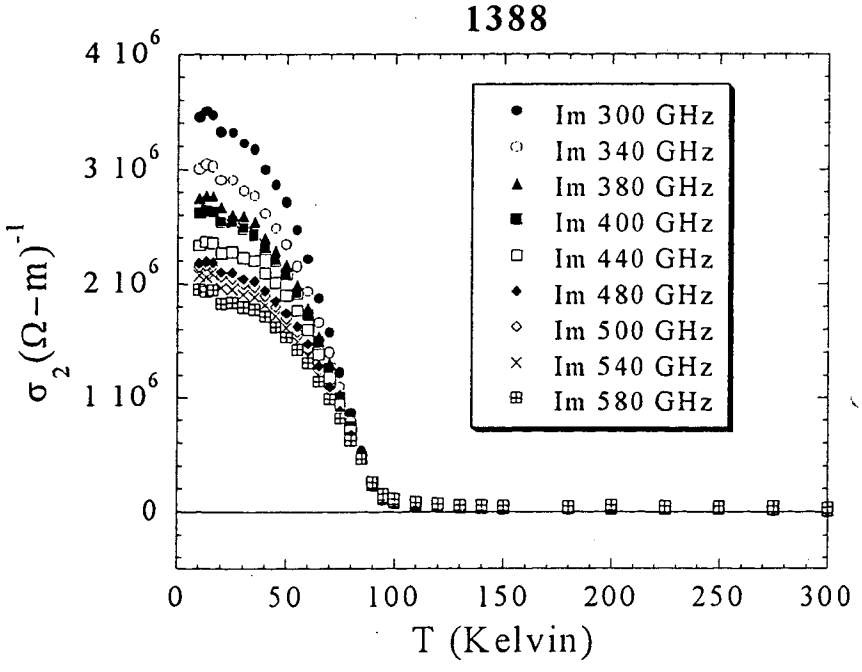
1388
4 10^6
3 10^6
2 10^6
1 10^6
0
σ2 (Ω−m)^-1
0
50
100
150
200
250
300
T (Kelvin)
Im 300 GHz
Im 340 GHz
Im 380 GHz
Im 400 GHz
Im 440 GHz
Im 480 GHz
Im 500 GHz
Im 540 GHz
Im 580 GHz

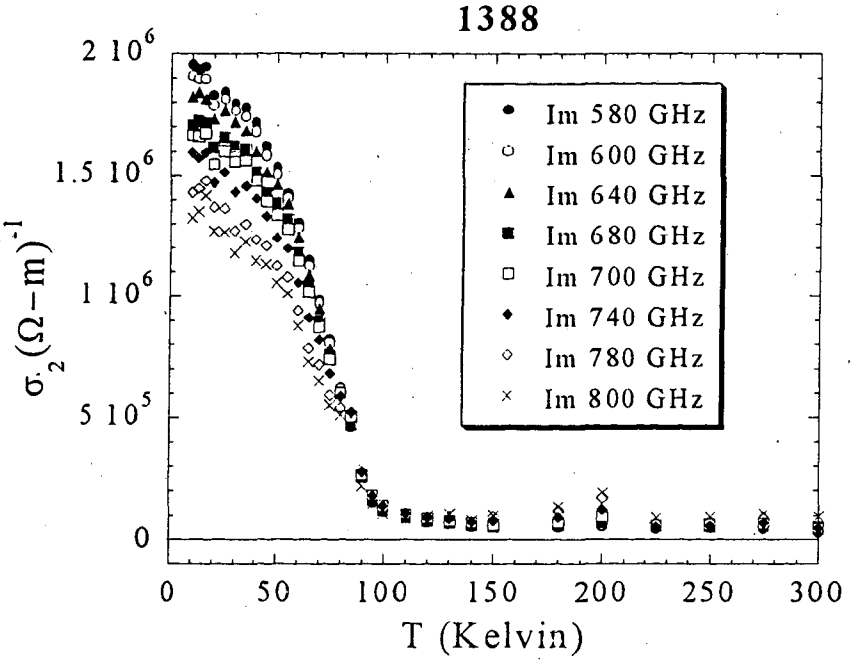
1388
2 10^6
1.5 10^6
1 10^6
5 10^5
0
σ_2 (Ω-m)^-1
0
50
100
150
200
250
300
T (Kelvin)
Im 580 GHz
Im 600 GHz
Im 640 GHz
Im 680 GHz
Im 700 GHz
Im 740 GHz
Im 780 GHz
Im 800 GHz

C.2 Sample 1280 - underdoped, $T_c = 71K$

C.2.1 Spectra

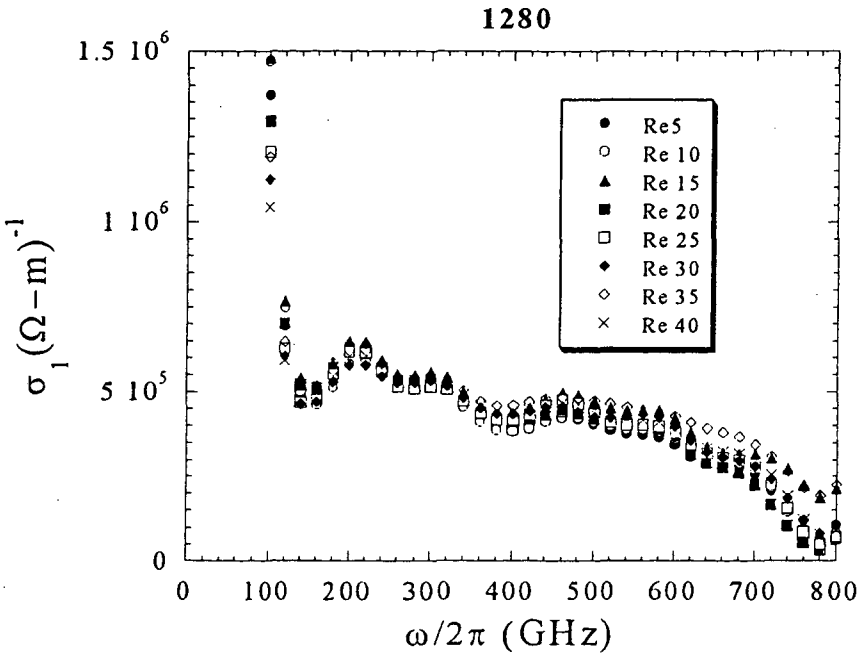

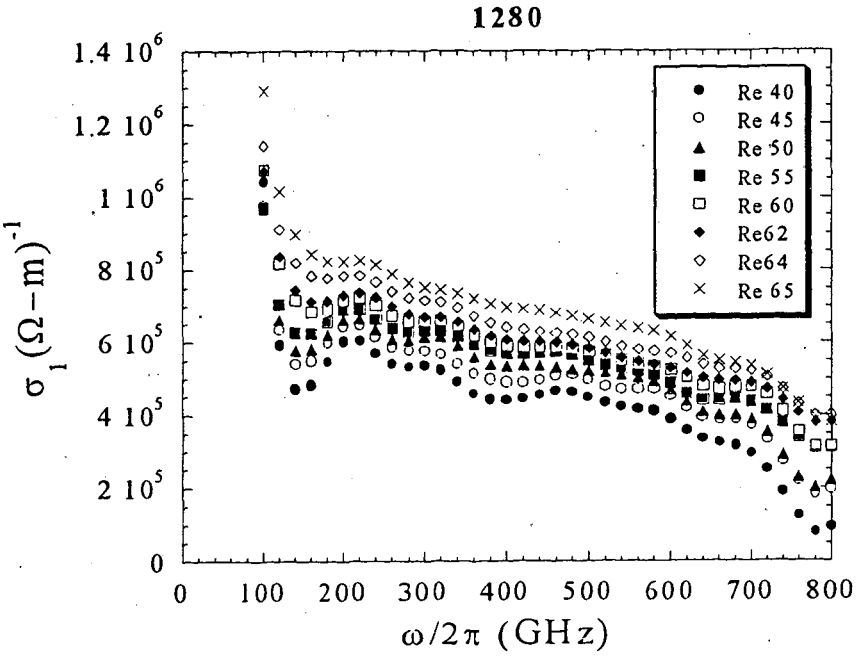
1280
1.4 10^6
1.2 10^6
1 10^6
8 10^5
6 10^5
4 10^5
2 10^5
0
σ_1 (Ω−m)^-1
0
100
200
300
400
500
600
700
800
ω/2π (GHz)
Re 40
Re 45
Re 50
Re 55
Re 60
Re62
Re64
Re 65

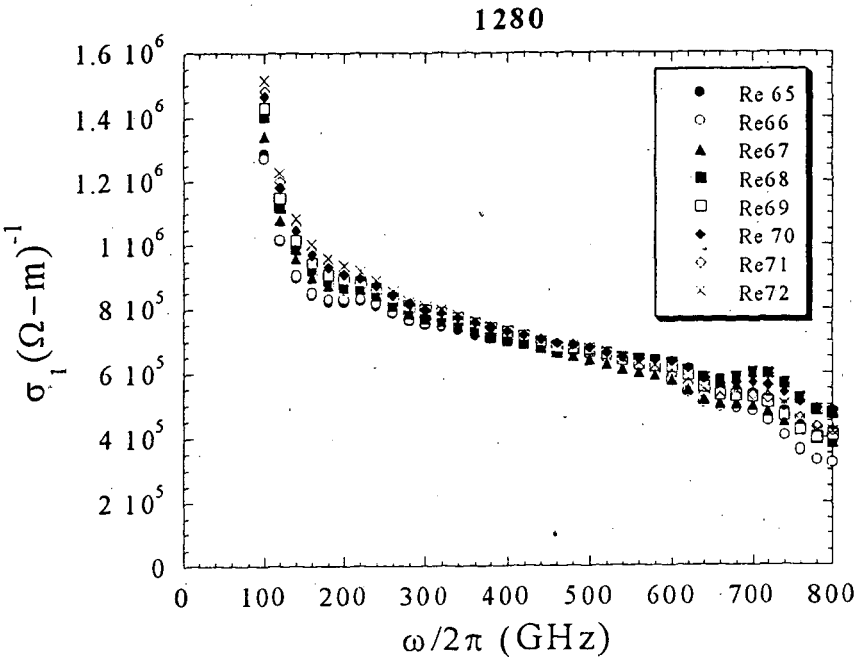
1280
1.6 10^6
1.4 10^6
1.2 10^6
1 10^6
8 10^5
6 10^5
4 10^5
2 10^5
0
σ_1 (Ω−m)^-1
0
100
200
300
400
500
600
700
800
ω/2π (GHz)
Re 65
Re66
Re67
Re68
Re69
Re 70
Re71
Re72

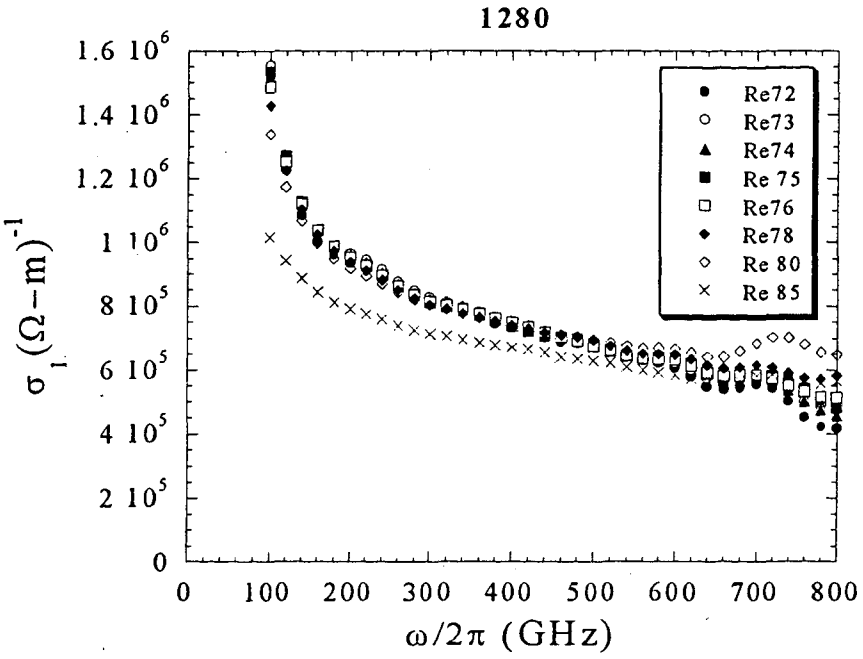
1280
1.6 10^6
1.4 10^6
1.2 10^6
1 10^6
8 10^5
6 10^5
4 10^5
2 10^5
0
σ_1 (Ω−m)^-1
0
100
200
300
400
500
600
700
800
ω/2π (GHz)
Re72
Re73
Re74
Re 75
Re76
Re78
Re 80
Re 85

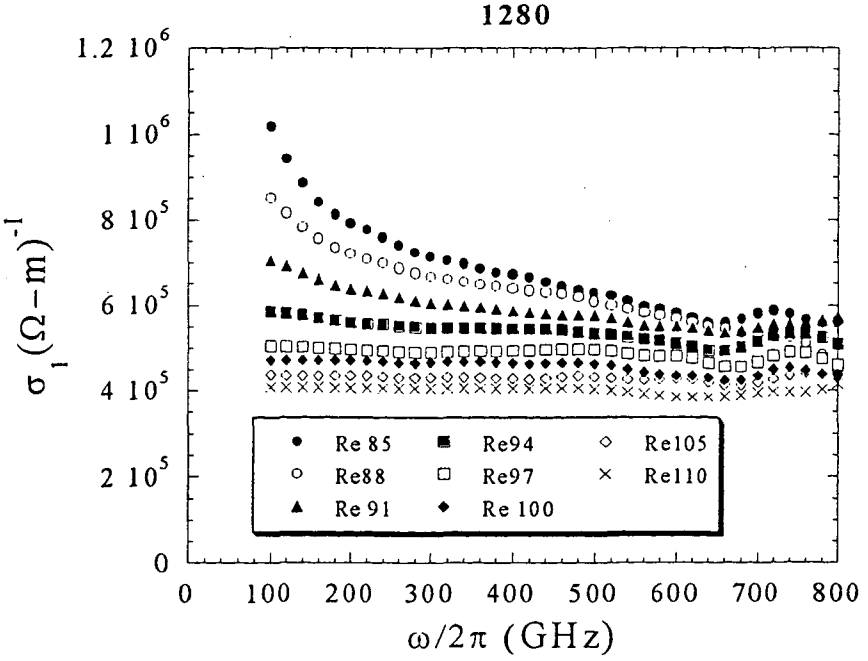
1280
1.2 10^6
1 10^6
8 10^5
6 10^5
4 10^5
2 10^5
0
σ_1 (Ω−m)^-1
0
100
200
300
400
500
600
700
800
ω/2π (GHz)
Re 85
Re88
Re 91
Re94
Re97
Re 100
Re105
Re110

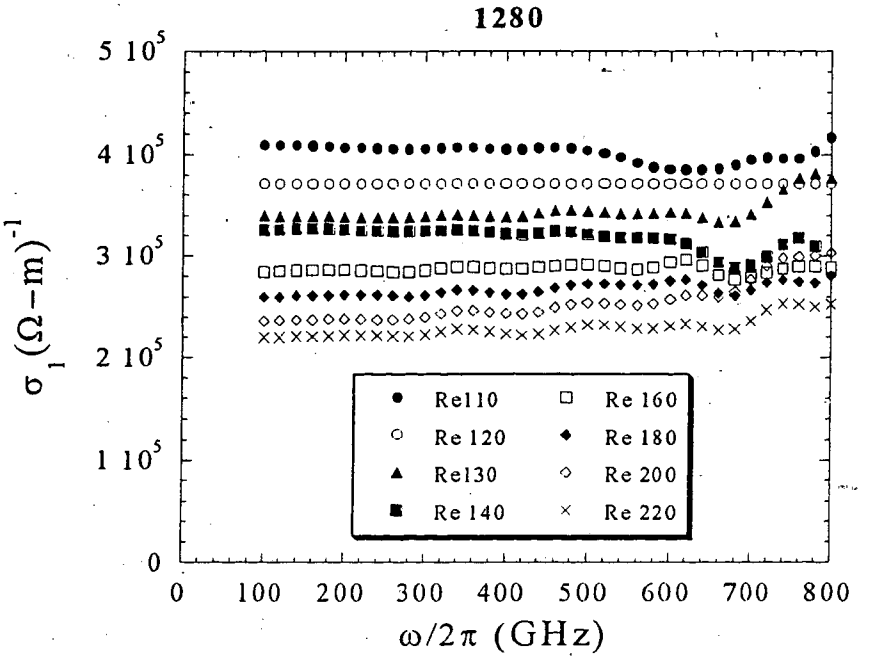
1280
5 10^5
4 10^5
3 10^5
2 10^5
1 10^5
0
σ_1 (Ω−m)^-1
0
100
200
300
400
500
600
700
800
ω/2π (GHz)
Re110
Re 120
Re130
Re 140
Re 160
Re 180
Re 200
Re 220

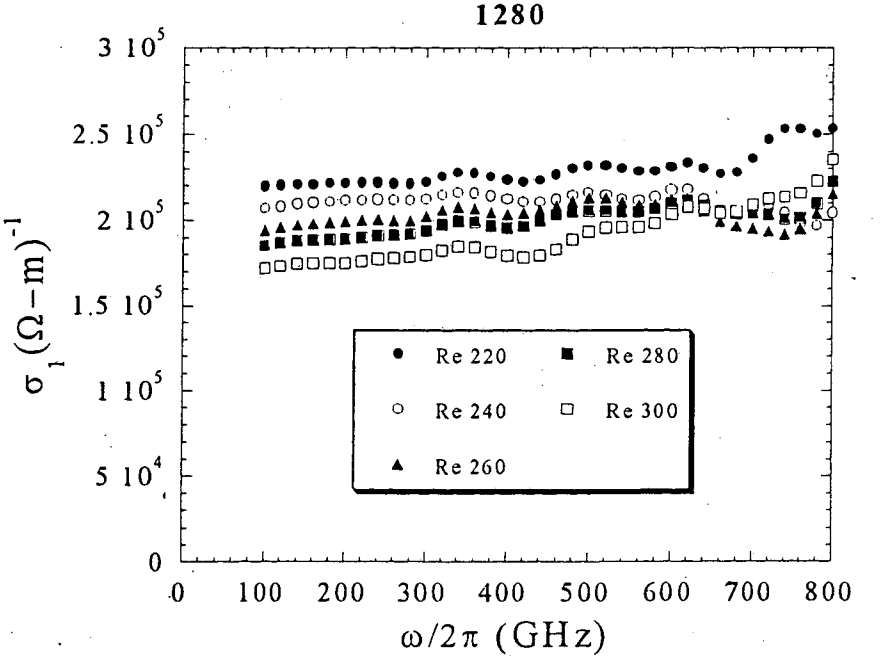
1280
3 10^5
2.5 10^5
2 10^5
1.5 10^5
1 10^5
5 10^4
0
σ_1 (Ω−m)^-1
0
100
200
300
400
500
600
700
800
ω/2π (GHz)
Re 220
Re 240
Re 260
Re 280
Re 300

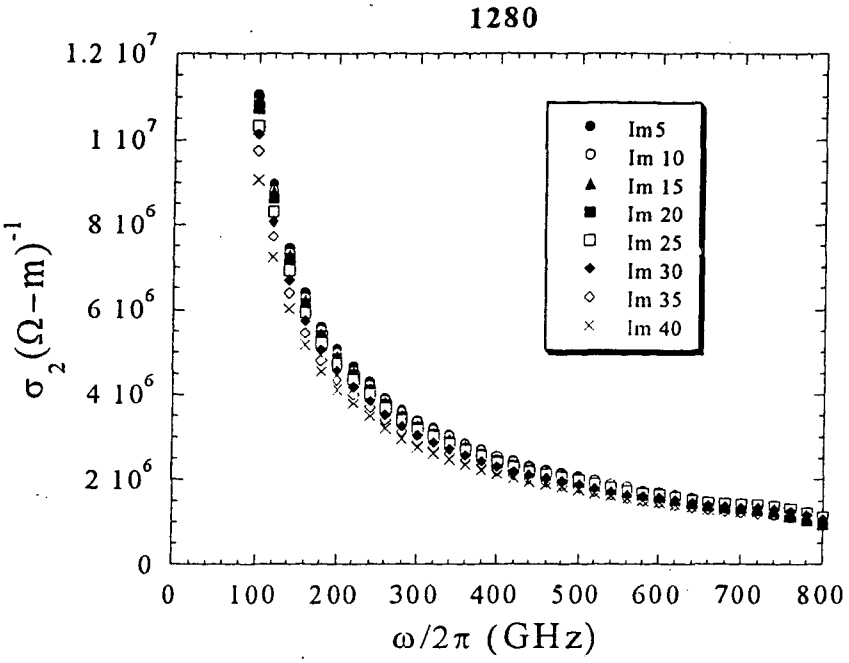
1280
1.2 10^7
1 10^7
8 10^6
6 10^6
4 10^6
2 10^6
0
σ2 (Ω-m)^-1
0
100
200
300
400
500
600
700
800
ω/2π (GHz)
Im5
Im 10
Im 15
Im 20
Im 25
Im 30
Im 35
Im 40

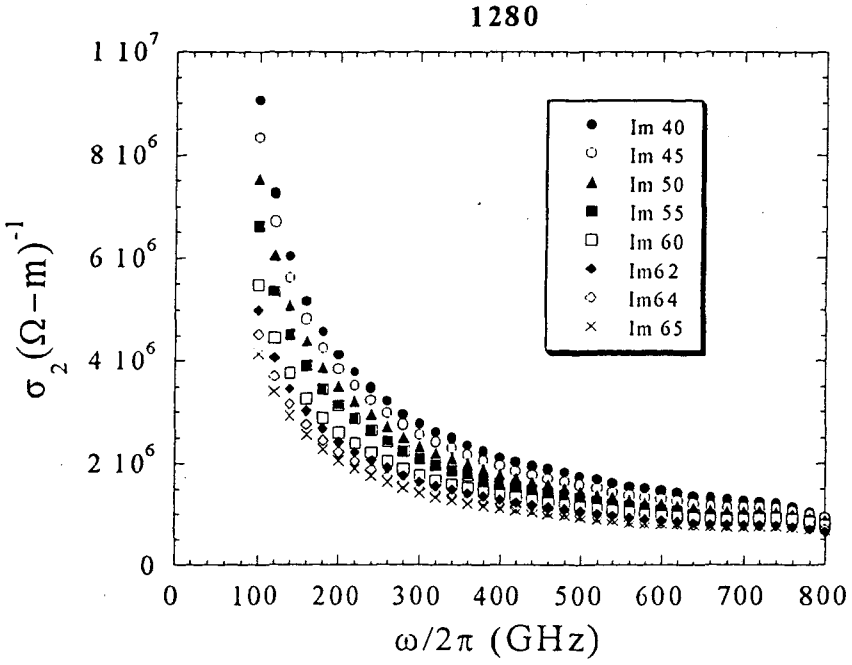
1280
1 10^7
8 10^6
6 10^6
4 10^6
2 10^6
0
σ2 (Ω-m)^-1
0
100
200
300
400
500
600
700
800
ω/2π (GHz)
Im 40
Im 45
Im 50
Im 55
Im 60
Im62
Im64
Im 65

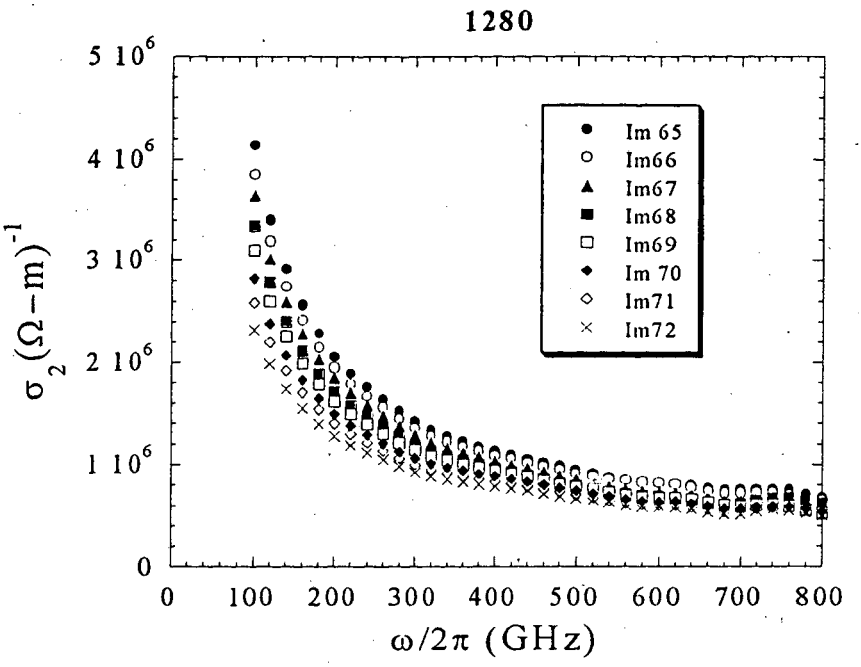
1280
5 10^6
4 10^6
3 10^6
2 10^6
1 10^6
0
σ2 (Ω−m)^-1
0
100
200
300
400
500
600
700
800
ω/2π (GHz)
Im 65
Im66
Im67
Im68
Im69
Im 70
Im71
Im72

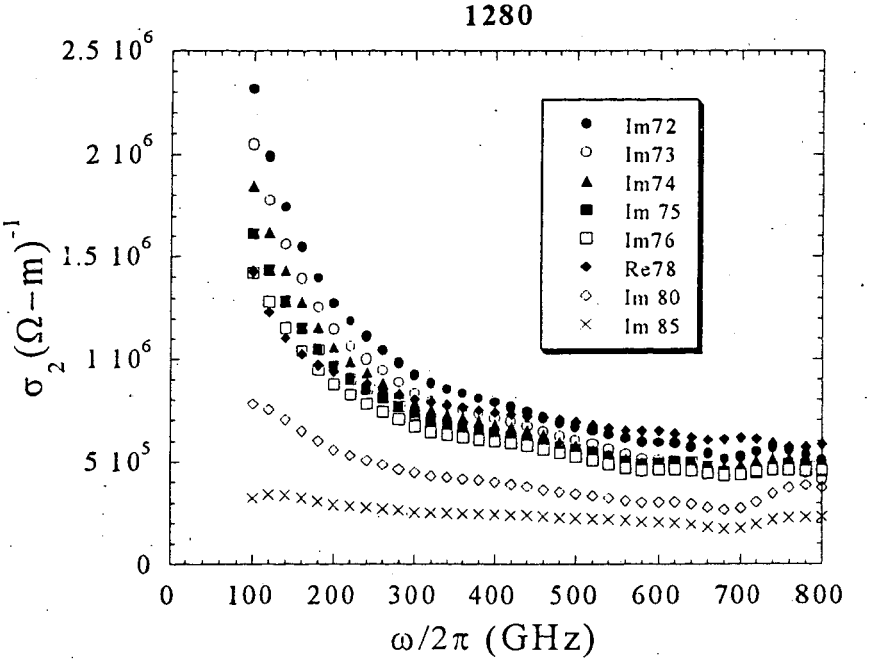
1280
2.5 10^6
2 10^6
1.5 10^6
1 10^6
5 10^5
0
σ2 (Ω−m)^-1
0
100
200
300
400
500
600
700
800
ω/2π (GHz)
Im72
Im73
Im74
Im 75
Im76
Re78
Im 80
Im 85

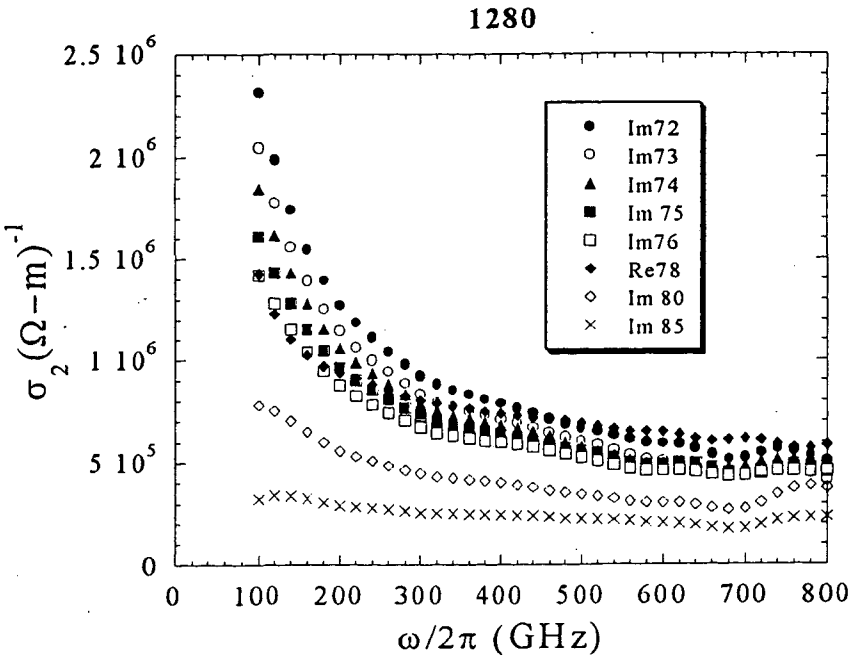
1280
2.5 10^6
2 10^6
1.5 10^6
1 10^6
5 10^5
0
σ2 (Ω−m)^-1
0
100
200
300
400
500
600
700
800
ω/2π (GHz)
Im72
Im73
Im74
Im 75
Im76
Re78
Im 80
Im 85

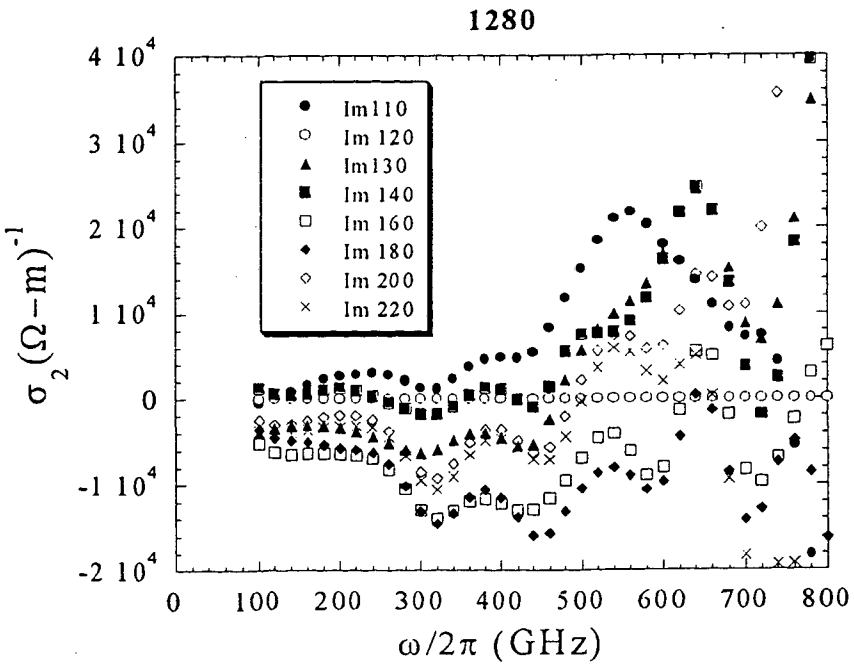
1280
4 10^4
3 10^4
2 10^4
1 10^4
0
-1 10^4
-2 10^4
σ2 (Ω−m)^-1
0
100
200
300
400
500
600
700
800
ω/2π (GHz)
Im110
Im 120
Im130
Im 140
Im 160
Im 180
Im 200
Im 220

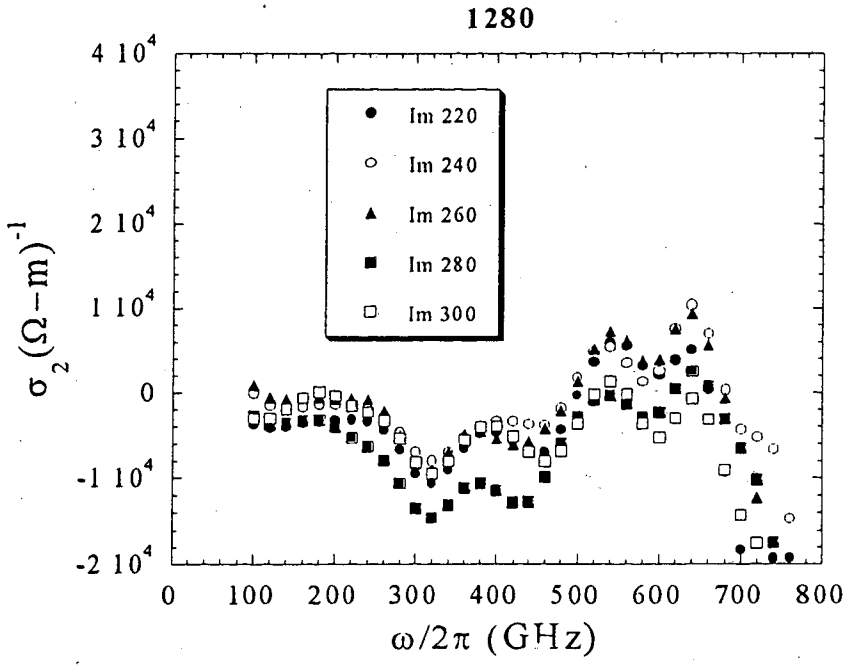
1280
Im 220
Im 240
Im 260
Im 280
Im 300
$\sigma_2(\Omega\text{-m})^{-1}$
4 10^4
3 10^4
2 10^4
1 10^4
0
-1 10^4
-2 10^4
0
100
200
300
400
500
600
700
800
ω/2π (GHz)

C.2.2 Temperature Dependence

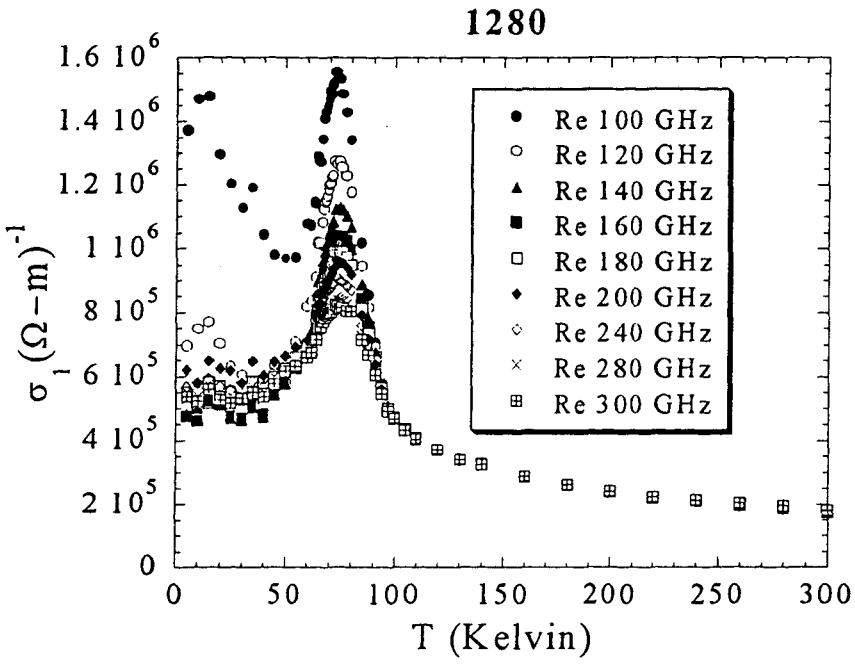

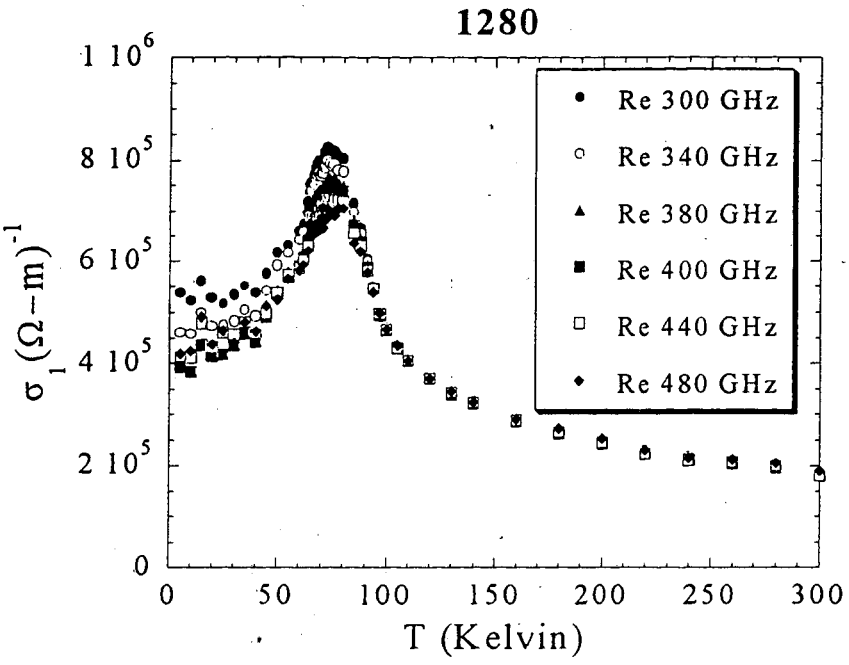
1280
1 10^6
8 10^5
6 10^5
4 10^5
2 10^5
0
σ1 (Ω-m)^-1
0
50
100
150
200
250
300
T (Kelvin)
Re 300 GHz
Re 340 GHz
Re 380 GHz
Re 400 GHz
Re 440 GHz
Re 480 GHz

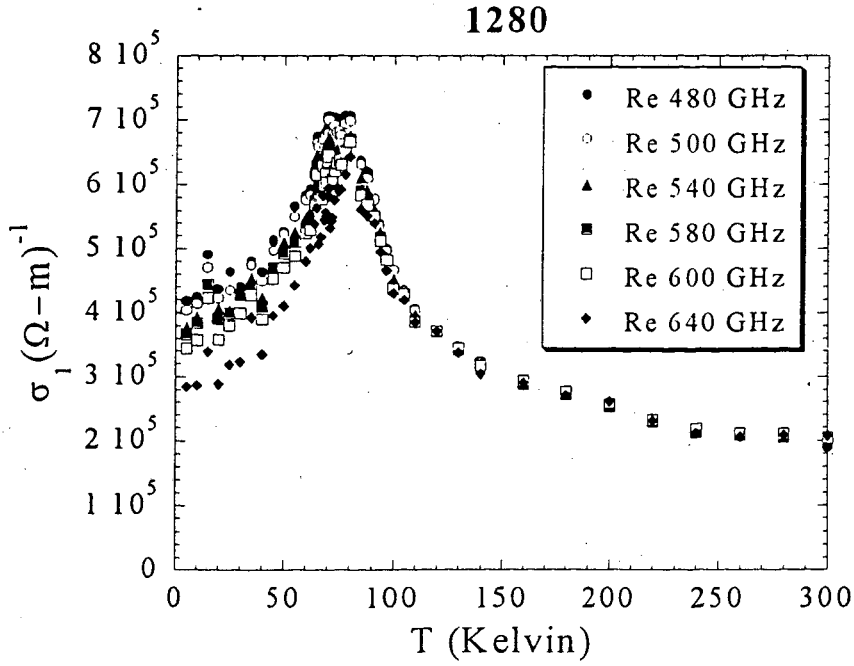
1280
8 10^5
7 10^5
6 10^5
5 10^5
4 10^5
3 10^5
2 10^5
1 10^5
0
σ1 (Ω-m)^-1
0
50
100
150
200
250
300
T (Kelvin)
Re 480 GHz
Re 500 GHz
Re 540 GHz
Re 580 GHz
Re 600 GHz
Re 640 GHz

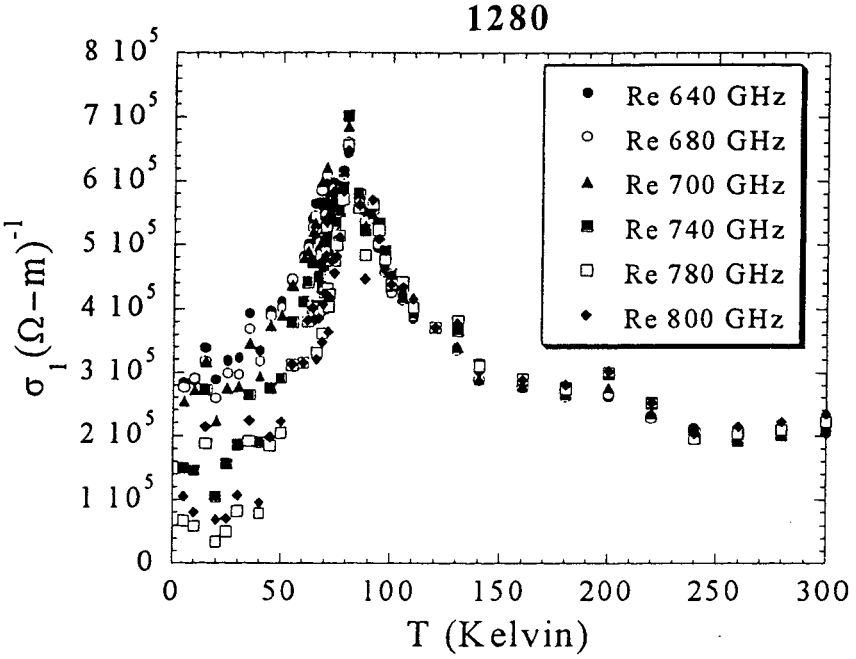
1280
Re 640 GHz
Re 680 GHz
Re 700 GHz
Re 740 GHz
Re 780 GHz
Re 800 GHz
σ1 (Ω-m)-1
T (Kelvin)

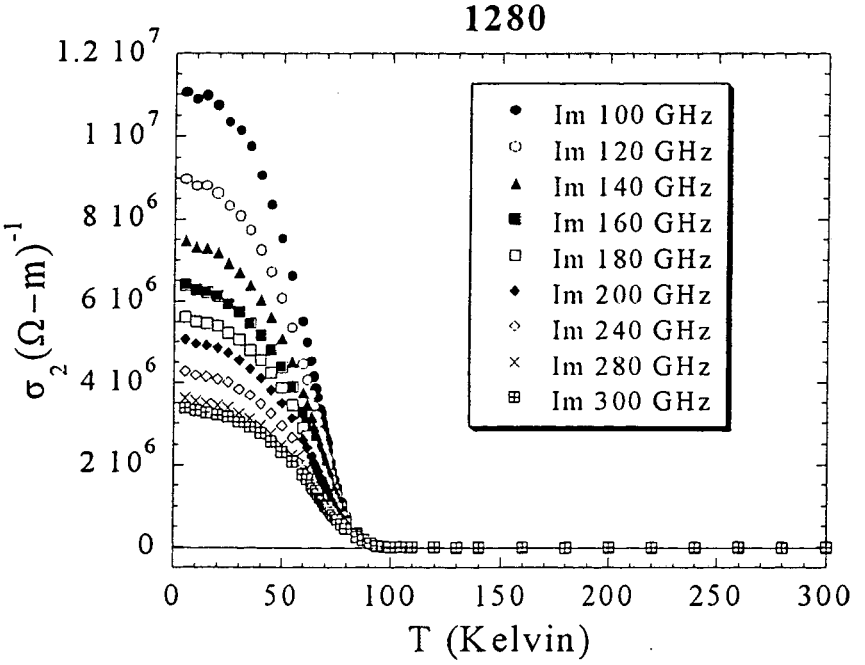
1280
Im 100 GHz
Im 120 GHz
Im 140 GHz
Im 160 GHz
Im 180 GHz
Im 200 GHz
Im 240 GHz
Im 280 GHz
Im 300 GHz
σ2 (Ω-m)-1
T (Kelvin)

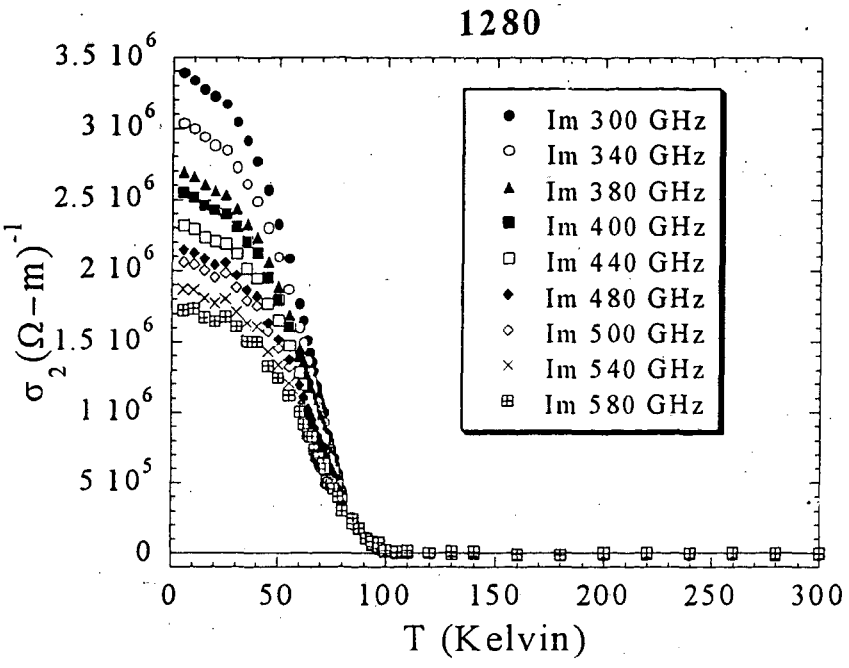
1280
3.5 10^6
3 10^6
2.5 10^6
2 10^6
1.5 10^6
1 10^6
5 10^5
0
σ2 (Ω−m)^-1
0
50
100
150
200
250
300
T (Kelvin)
Im 300 GHz
Im 340 GHz
Im 380 GHz
Im 400 GHz
Im 440 GHz
Im 480 GHz
Im 500 GHz
Im 540 GHz
Im 580 GHz

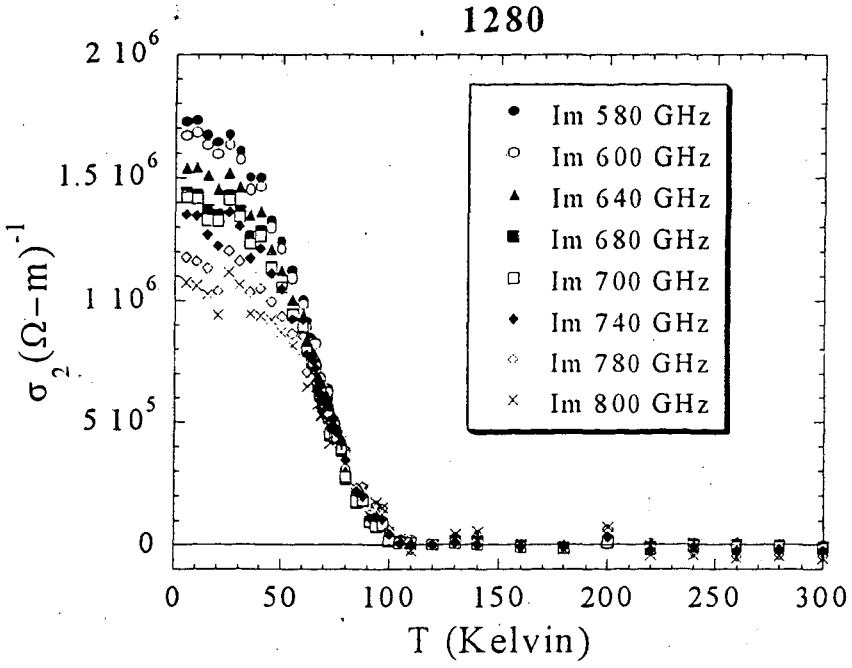
1280
2 10^6
1.5 10^6
1 10^6
5 10^5
0
σ2 (Ω−m)^-1
0
50
100
150
200
250
300
T (Kelvin)
Im 580 GHz
Im 600 GHz
Im 640 GHz
Im 680 GHz
Im 700 GHz
Im 740 GHz
Im 780 GHz
Im 800 GHz

C.3 Sample 1249 $T_c = 72K$

C.3.1 Spectra–real part

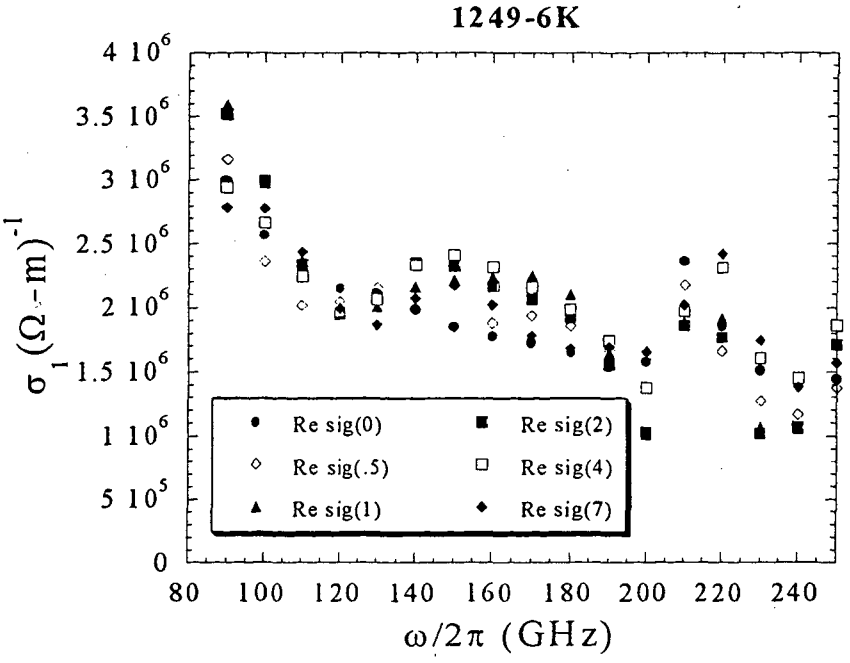

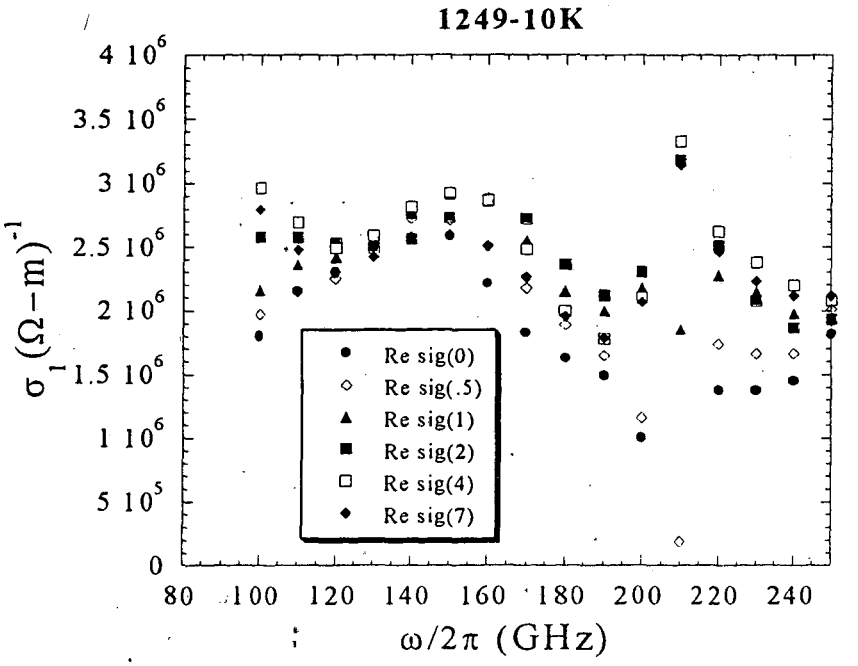
1249-10K
4 10^6
3.5 10^6
3 10^6
2.5 10^6
2 10^6
1.5 10^6
1 10^6
5 10^5
0
σ_1 (Ω−m)^-1
80 100 120 140 160 180 200 220 240
ω/2π (GHz)
Re sig(0)
Re sig(.5)
Re sig(1)
Re sig(2)
Re sig(4)
Re sig(7)

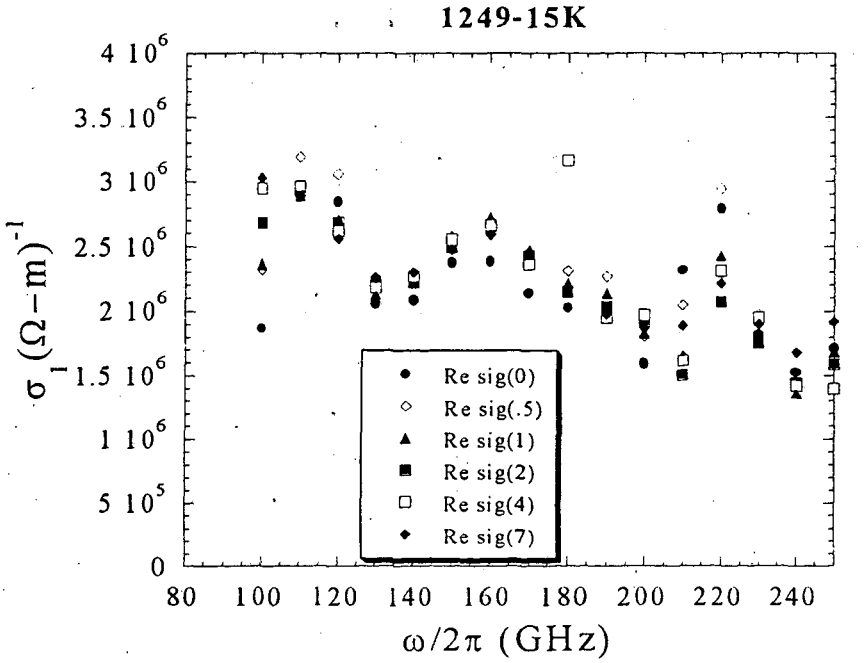
1249-15K
4 10^6
3.5 10^6
3 10^6
2.5 10^6
2 10^6
1.5 10^6
1 10^6
5 10^5
0
σ_1 (Ω−m)^-1
80 100 120 140 160 180 200 220 240
ω/2π (GHz)
Re sig(0)
Re sig(.5)
Re sig(1)
Re sig(2)
Re sig(4)
Re sig(7)

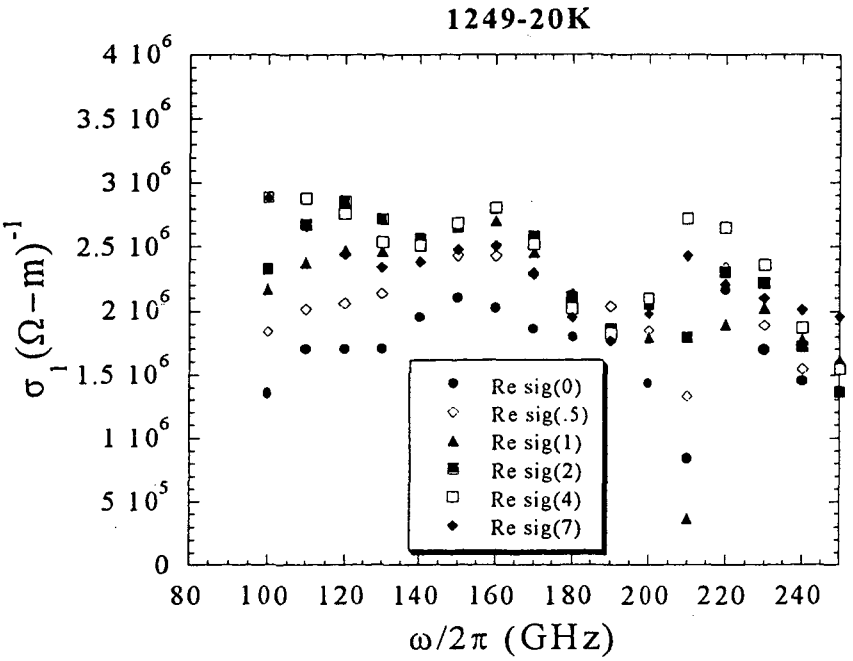
1249-20K
4 10^6
3.5 10^6
3 10^6
2.5 10^6
2 10^6
1.5 10^6
1 10^6
5 10^5
0
σ_1 (Ω−m)^-1
80 100 120 140 160 180 200 220 240
ω/2π (GHz)
Re sig(0)
Re sig(.5)
Re sig(1)
Re sig(2)
Re sig(4)
Re sig(7)

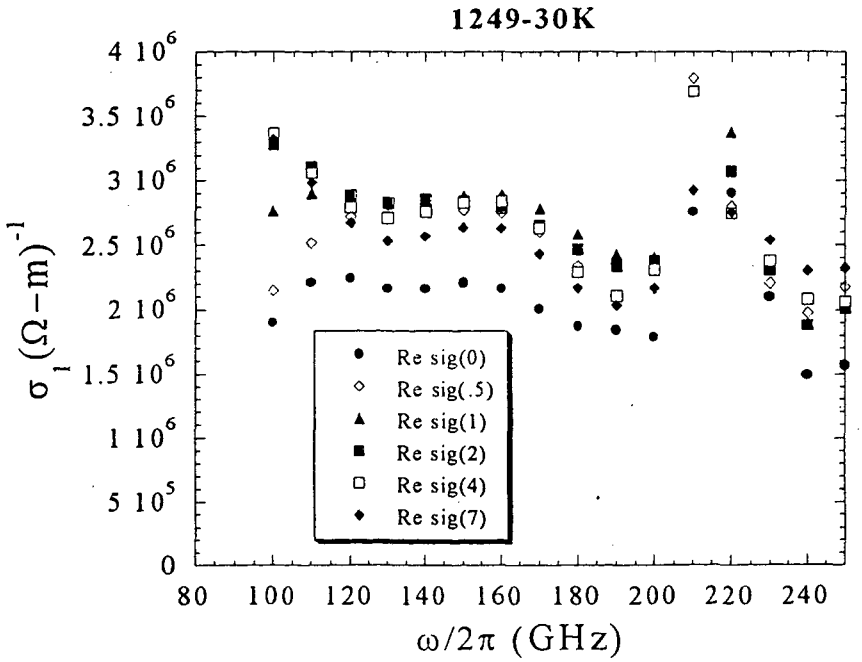
1249-30K
4 10^6
3.5 10^6
3 10^6
2.5 10^6
2 10^6
1.5 10^6
1 10^6
5 10^5
0
σ_1 (Ω−m)^-1
80 100 120 140 160 180 200 220 240
ω/2π (GHz)
Re sig(0)
Re sig(.5)
Re sig(1)
Re sig(2)
Re sig(4)
Re sig(7)

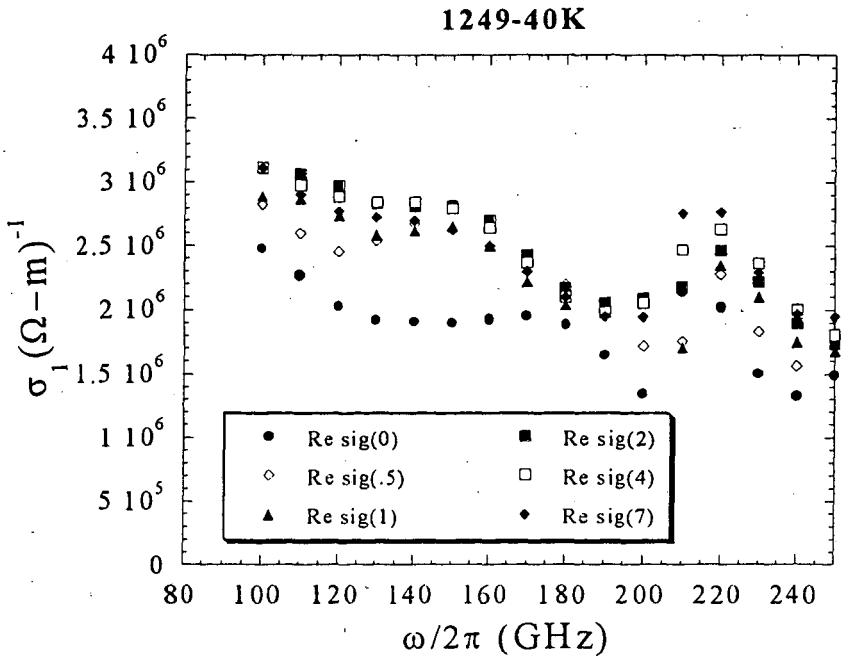
1249-40K
4 10^6
3.5 10^6
3 10^6
2.5 10^6
2 10^6
1.5 10^6
1 10^6
5 10^5
0
σ1 (Ω−m)^-1
80 100 120 140 160 180 200 220 240
ω/2π (GHz)
Re sig(0)
Re sig(.5)
Re sig(1)
Re sig(2)
Re sig(4)
Re sig(7)

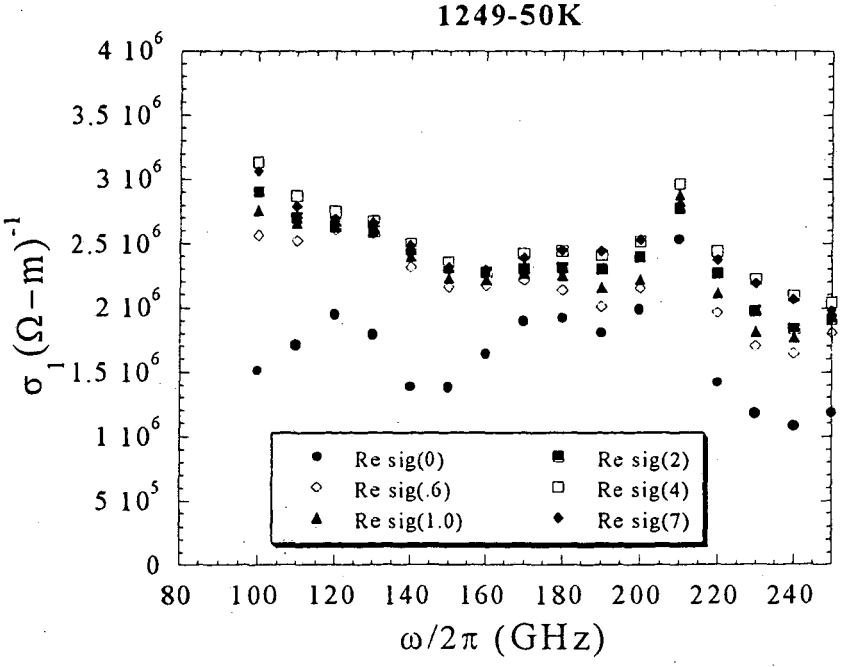
1249-50K
4 10^6
3.5 10^6
3 10^6
2.5 10^6
2 10^6
1.5 10^6
1 10^6
5 10^5
0
σ1 (Ω−m)^-1
80 100 120 140 160 180 200 220 240
ω/2π (GHz)
Re sig(0)
Re sig(.6)
Re sig(1.0)
Re sig(2)
Re sig(4)
Re sig(7)

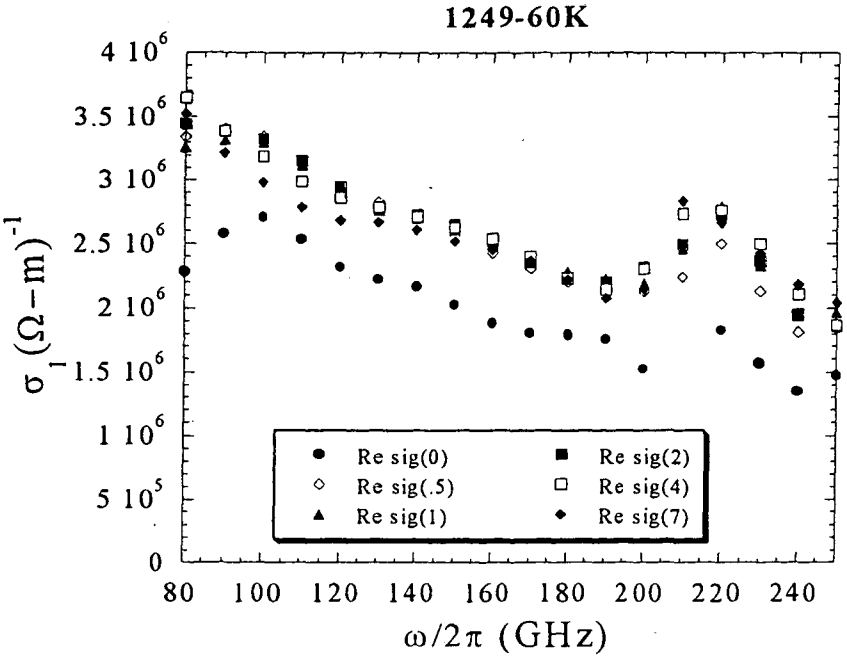
1249-60K
4 10^6
3.5 10^6
3 10^6
2.5 10^6
2 10^6
1.5 10^6
1 10^6
5 10^5
0
σ_1 (Ω−m)^-1
80 100 120 140 160 180 200 220 240
ω/2π (GHz)
Re sig(0)
Re sig(.5)
Re sig(1)
Re sig(2)
Re sig(4)
Re sig(7)

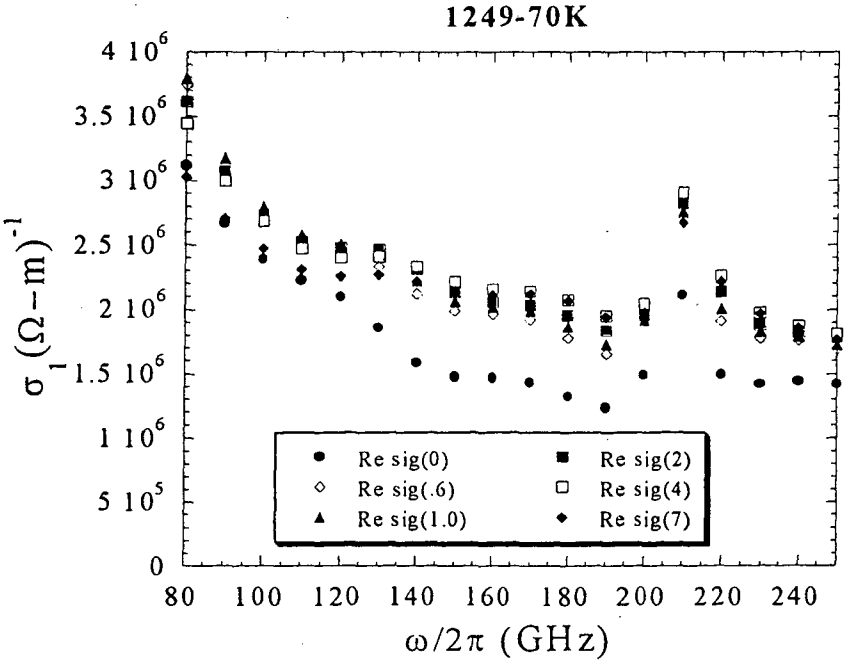
1249-70K
4 10^6
3.5 10^6
3 10^6
2.5 10^6
2 10^6
1.5 10^6
1 10^6
5 10^5
0
σ_1 (Ω−m)^-1
80 100 120 140 160 180 200 220 240
ω/2π (GHz)
Re sig(0)
Re sig(.6)
Re sig(1.0)
Re sig(2)
Re sig(4)
Re sig(7)

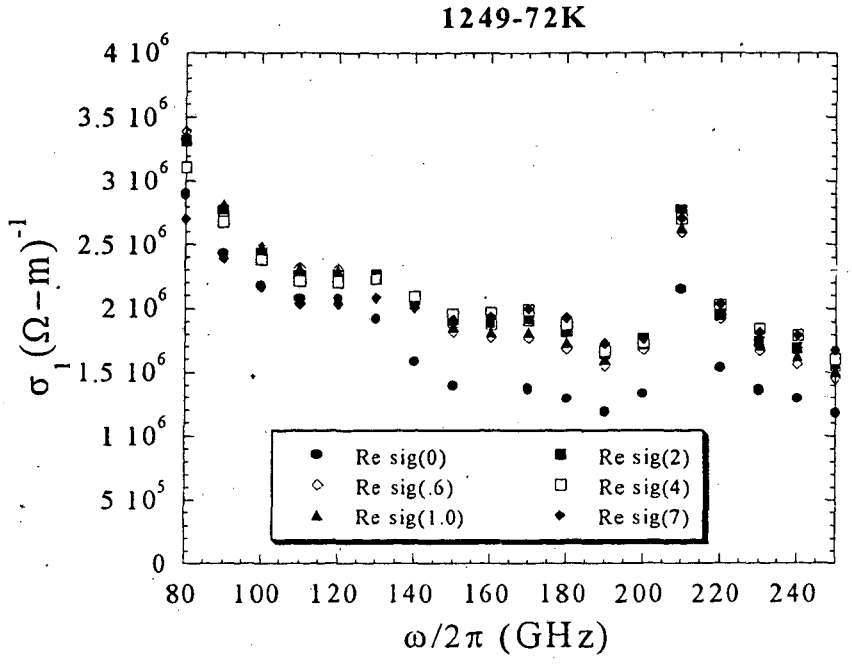
1249-72K
4 10^6
3.5 10^6
3 10^6
2.5 10^6
2 10^6
1.5 10^6
1 10^6
5 10^5
0
σ_1 (Ω-m)^-1
80 100 120 140 160 180 200 220 240
ω/2π (GHz)
Re sig(0)
Re sig(.6)
Re sig(1.0)
Re sig(2)
Re sig(4)
Re sig(7)

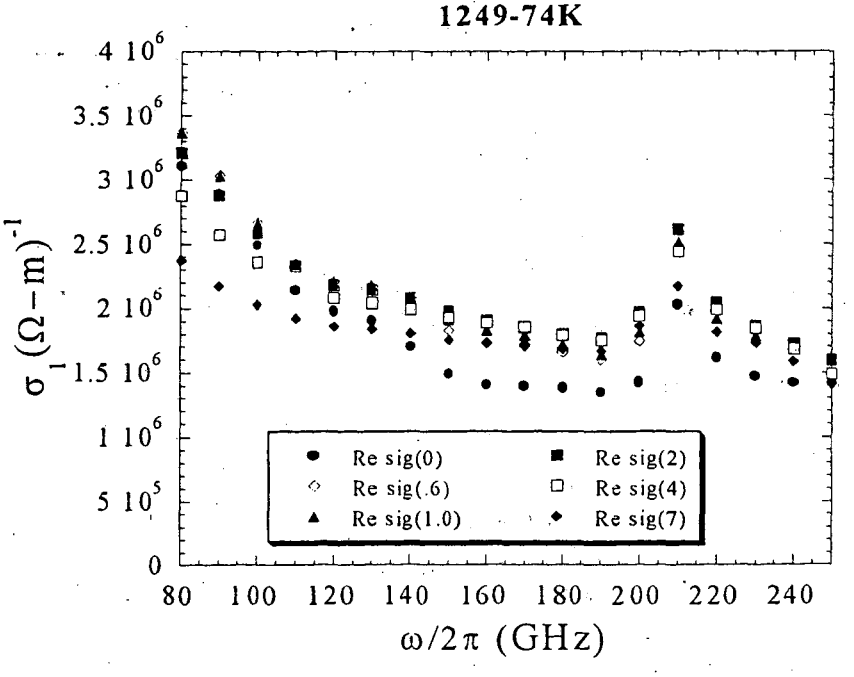
1249-74K
4 10^6
3.5 10^6
3 10^6
2.5 10^6
2 10^6
1.5 10^6
1 10^6
5 10^5
0
σ_1 (Ω-m)^-1
80 100 120 140 160 180 200 220 240
ω/2π (GHz)
Re sig(0)
Re sig(.6)
Re sig(1.0)
Re sig(2)
Re sig(4)
Re sig(7)

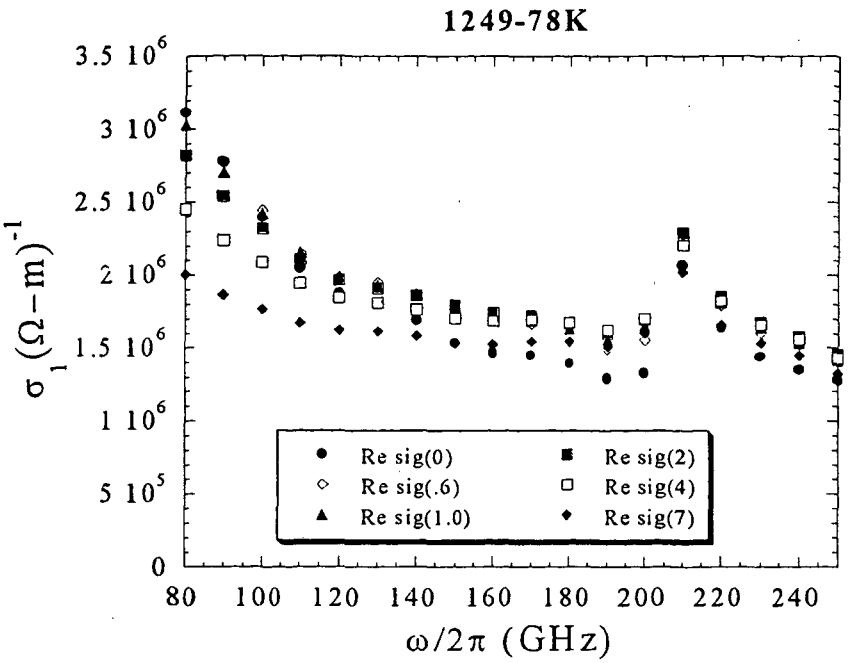
1249-78K
3.5 10^6
3 10^6
2.5 10^6
2 10^6
1.5 10^6
1 10^6
5 10^5
0
σ1 (Ω−m)^-1
80 100 120 140 160 180 200 220 240
ω/2π (GHz)
Re sig(0)
Re sig(.6)
Re sig(1.0)
Re sig(2)
Re sig(4)
Re sig(7)

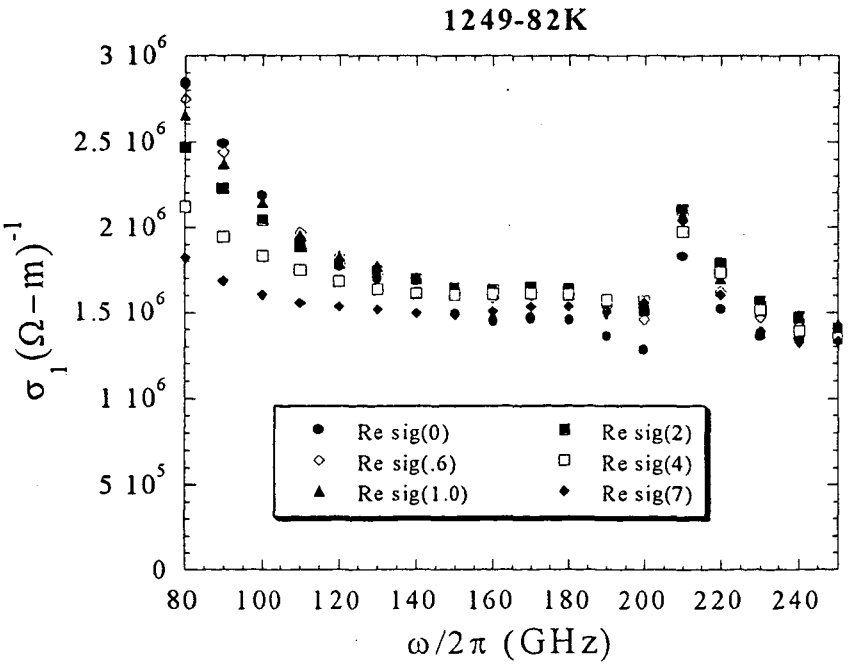
1249-82K
3 10^6
2.5 10^6
2 10^6
1.5 10^6
1 10^6
5 10^5
0
σ1 (Ω−m)^-1
80 100 120 140 160 180 200 220 240
ω/2π (GHz)
Re sig(0)
Re sig(.6)
Re sig(1.0)
Re sig(2)
Re sig(4)
Re sig(7)

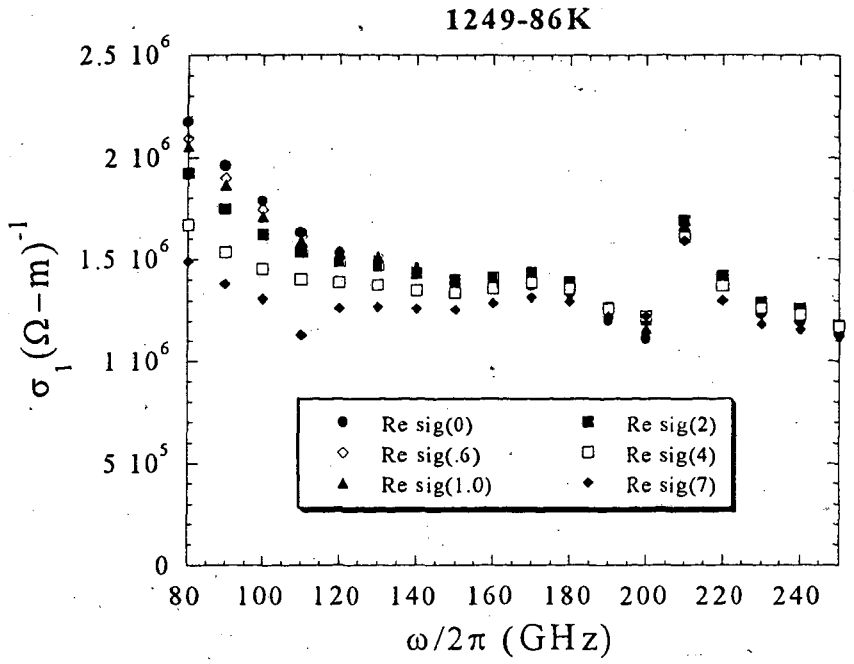
1249-86K
2.5 10^6
2 10^6
1.5 10^6
1 10^6
5 10^5
0
σ1 (Ω−m)^-1
80 100 120 140 160 180 200 220 240
ω/2π (GHz)
Re sig(0)
Re sig(.6)
Re sig(1.0)
Re sig(2)
Re sig(4)
Re sig(7)

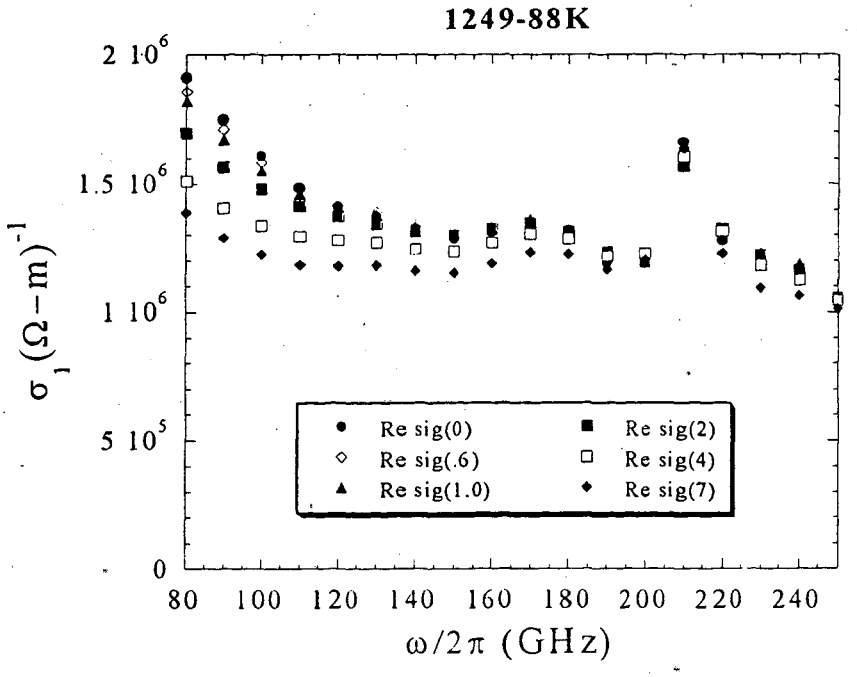
1249-88K
2 10^6
1.5 10^6
1 10^6
5 10^5
0
σ1 (Ω−m)^-1
80 100 120 140 160 180 200 220 240
ω/2π (GHz)
Re sig(0)
Re sig(.6)
Re sig(1.0)
Re sig(2)
Re sig(4)
Re sig(7)

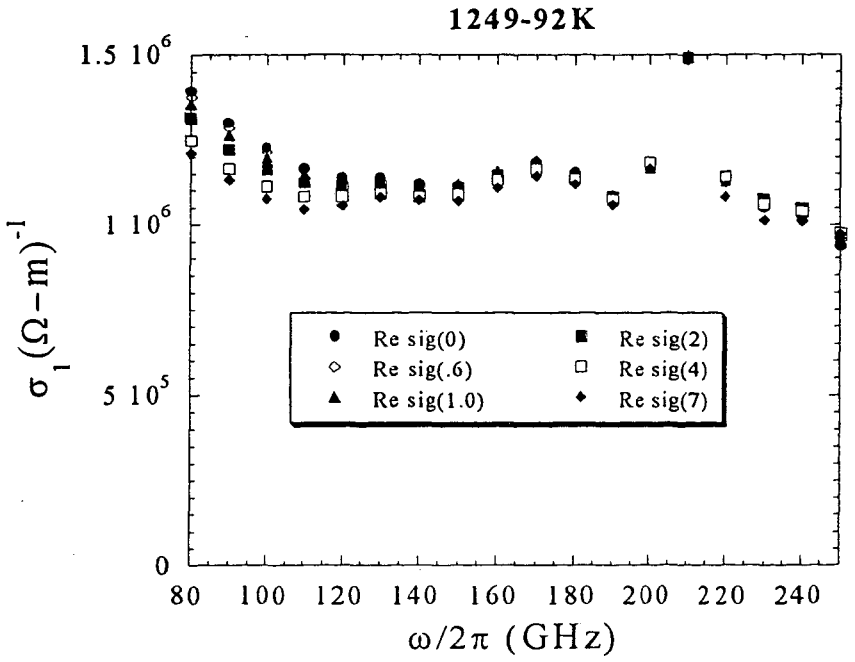
1249-92K
1.5 10^6
1 10^6
5 10^5
0
σ1 (Ω−m)^-1
80 100 120 140 160 180 200 220 240
ω/2π (GHz)
Re sig(0)
Re sig(.6)
Re sig(1.0)
Re sig(2)
Re sig(4)
Re sig(7)

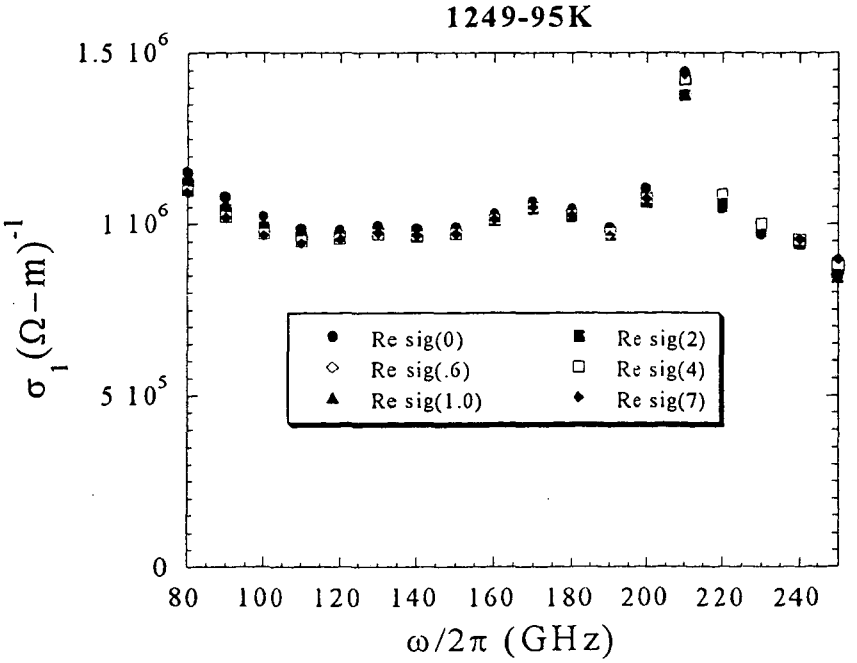
1249-95K
1.5 10^6
1 10^6
5 10^5
0
σ1 (Ω−m)^-1
80 100 120 140 160 180 200 220 240
ω/2π (GHz)
Re sig(0)
Re sig(.6)
Re sig(1.0)
Re sig(2)
Re sig(4)
Re sig(7)

C.3.2 Spectra–imaginary part

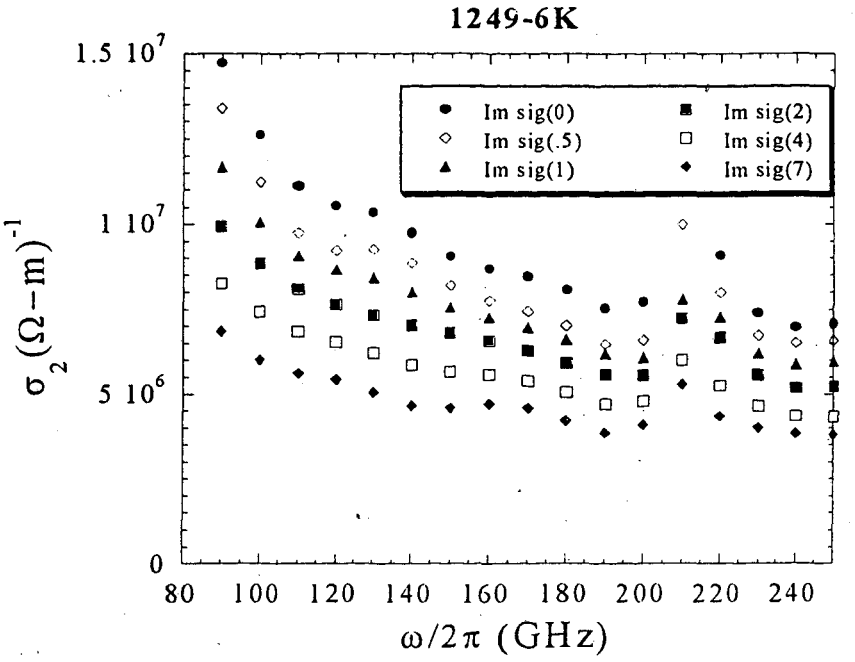

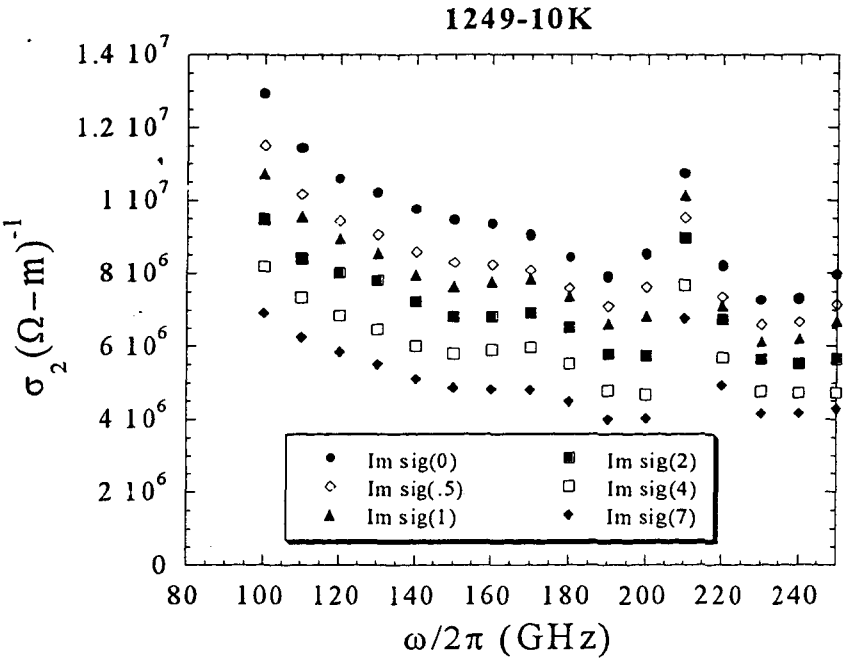
1249-10K
1.4 10^7
1.2 10^7
1 10^7
8 10^6
6 10^6
4 10^6
2 10^6
0
σ2 (Ω−m)^-1
80 100 120 140 160 180 200 220 240
ω/2π (GHz)
Im sig(0)
Im sig(.5)
Im sig(1)
Im sig(2)
Im sig(4)
Im sig(7)

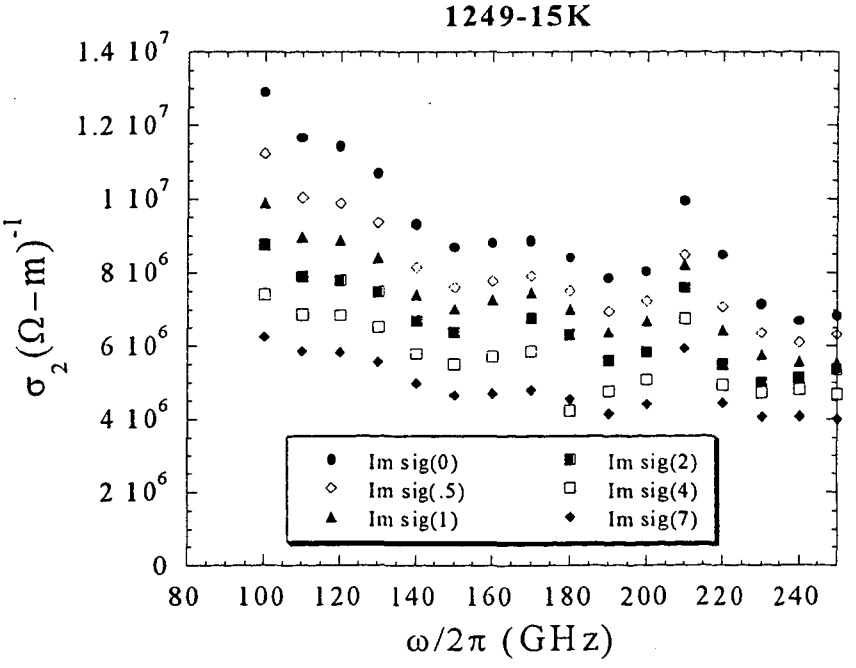
1249-15K
1.4 10^7
1.2 10^7
1 10^7
8 10^6
6 10^6
4 10^6
2 10^6
0
σ2 (Ω−m)^-1
80 100 120 140 160 180 200 220 240
ω/2π (GHz)
Im sig(0)
Im sig(.5)
Im sig(1)
Im sig(2)
Im sig(4)
Im sig(7)

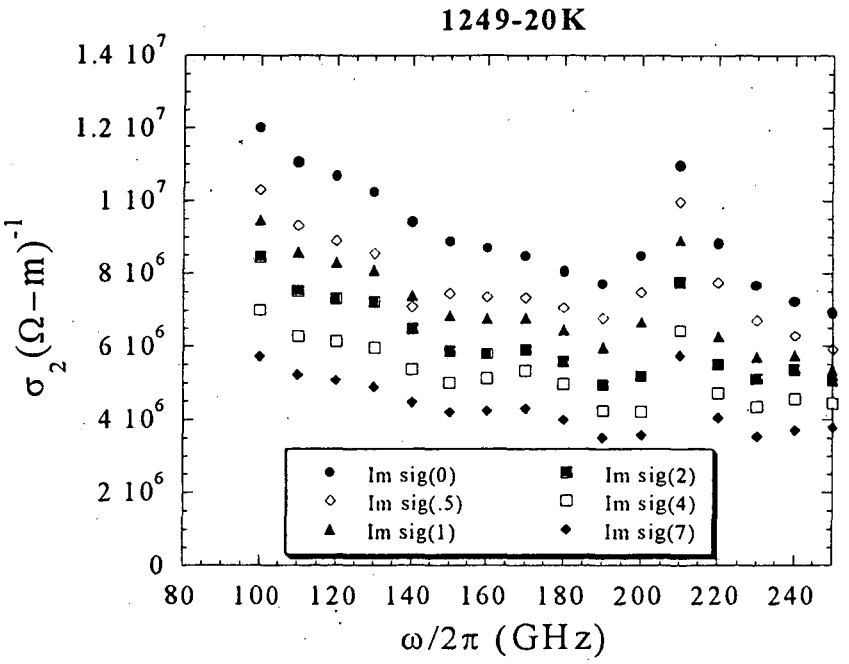
1249-20K
1.4 10^7
1.2 10^7
1 10^7
8 10^6
6 10^6
4 10^6
2 10^6
0
σ2 (Ω−m)^-1
80 100 120 140 160 180 200 220 240
ω/2π (GHz)
Im sig(0)
Im sig(.5)
Im sig(1)
Im sig(2)
Im sig(4)
Im sig(7)

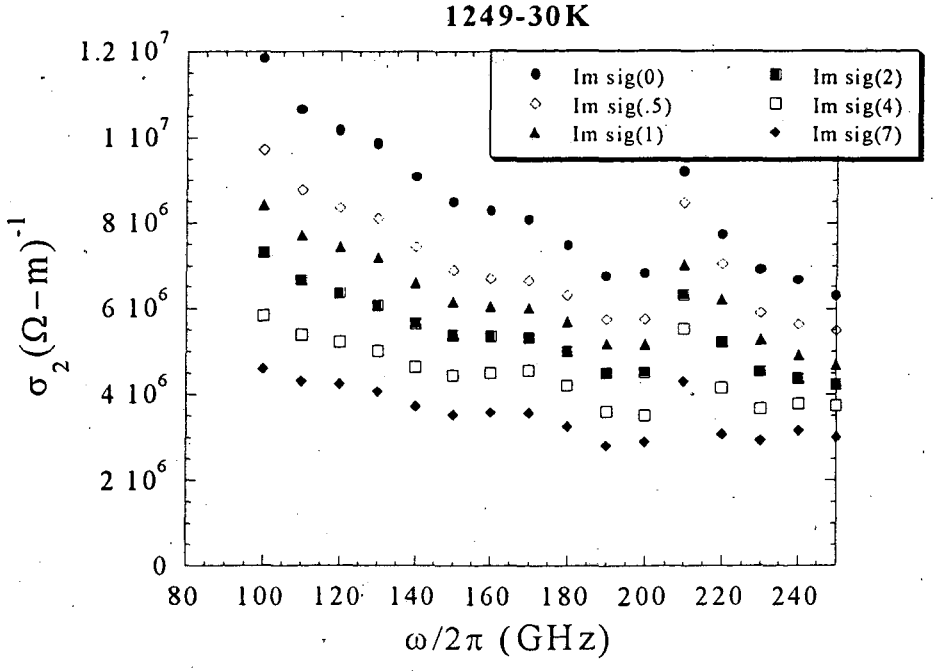
1249-30K
1.2 10^7
1 10^7
8 10^6
6 10^6
4 10^6
2 10^6
0
σ2 (Ω−m)^-1
80 100 120 140 160 180 200 220 240
ω/2π (GHz)
Im sig(0)
Im sig(.5)
Im sig(1)
Im sig(2)
Im sig(4)
Im sig(7)

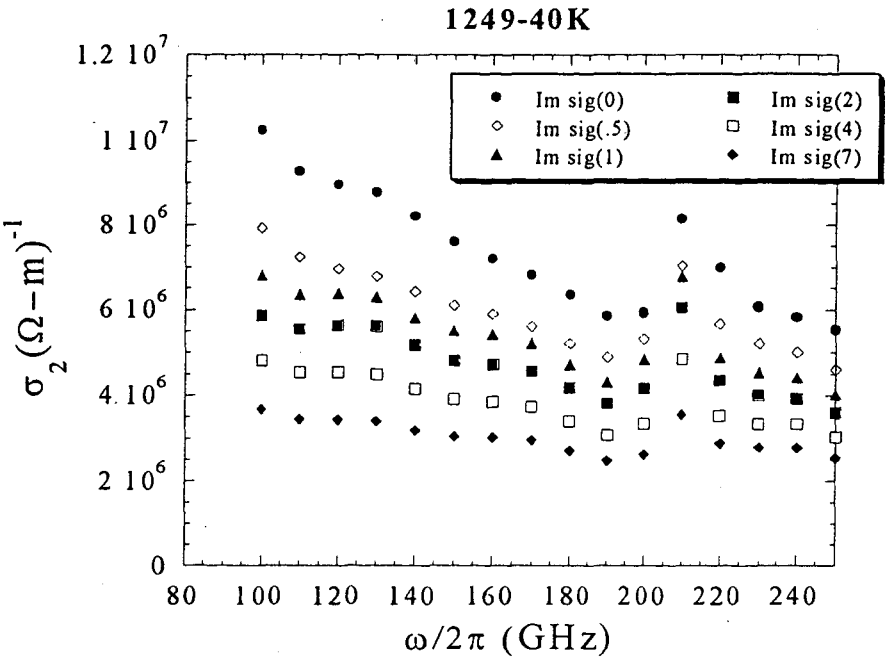
1249-40K
Im sig(0)
Im sig(.5)
Im sig(1)
Im sig(2)
Im sig(4)
Im sig(7)
1.2 10^7
1 10^7
8 10^6
6 10^6
4 10^6
2 10^6
0
80 100 120 140 160 180 200 220 240
ω/2π (GHz)
σ2(Ω−m)^-1

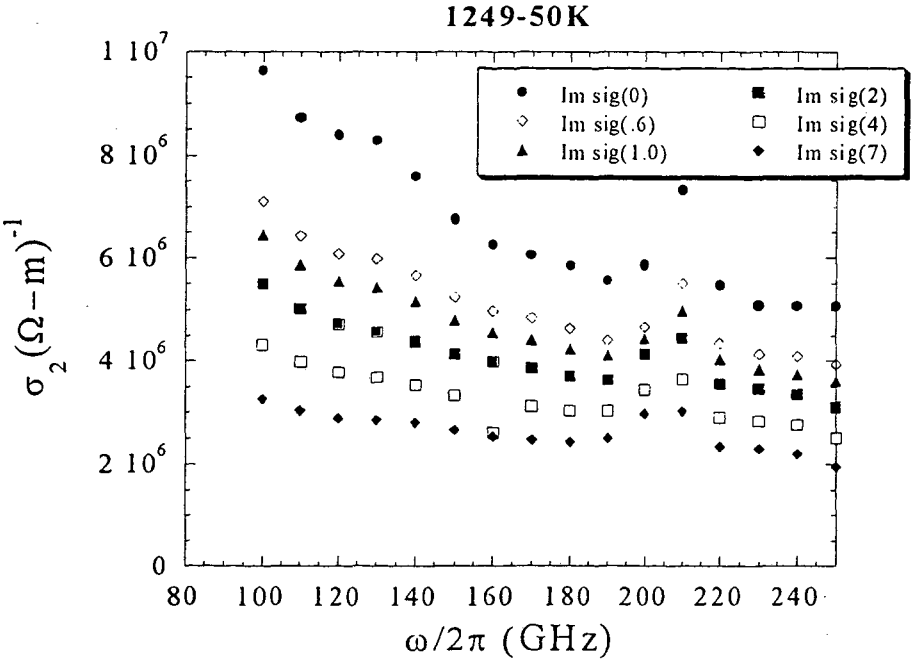
1249-50K
Im sig(0)
Im sig(.6)
Im sig(1.0)
Im sig(2)
Im sig(4)
Im sig(7)
1 10^7
8 10^6
6 10^6
4 10^6
2 10^6
0
80 100 120 140 160 180 200 220 240
ω/2π (GHz)
σ2(Ω−m)^-1

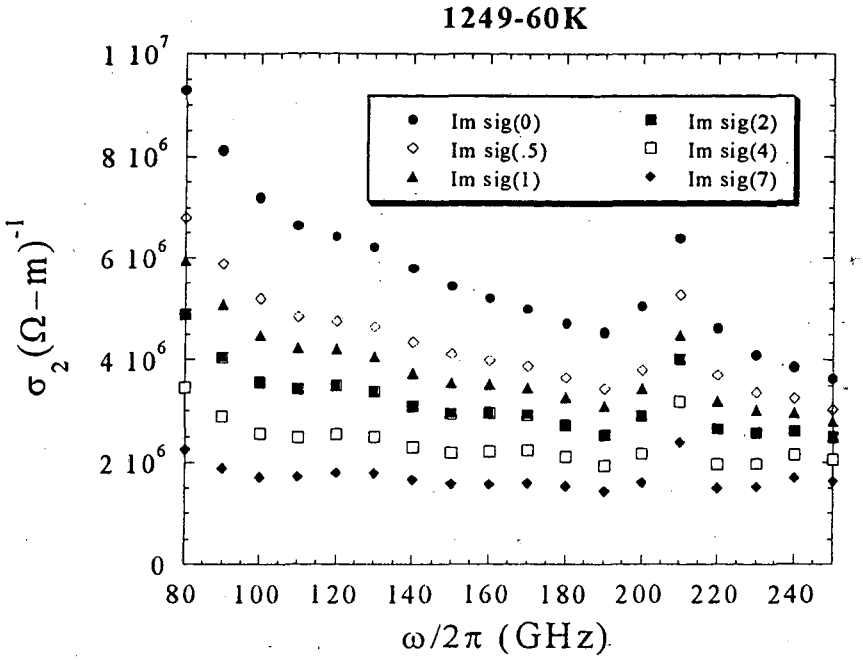
1249-60K
Im sig(0)
Im sig(.5)
Im sig(1)
Im sig(2)
Im sig(4)
Im sig(7)
σ2(Ω−m)-1
ω/2π (GHz)

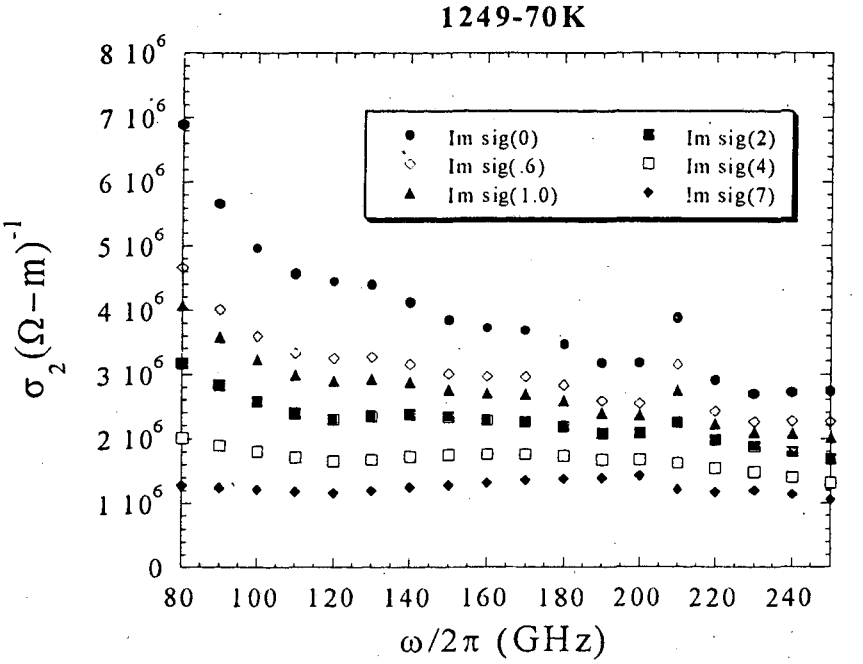
1249-70K
Im sig(0)
Im sig(.6)
Im sig(1.0)
Im sig(2)
Im sig(4)
Im sig(7)
σ2(Ω−m)-1
ω/2π (GHz)

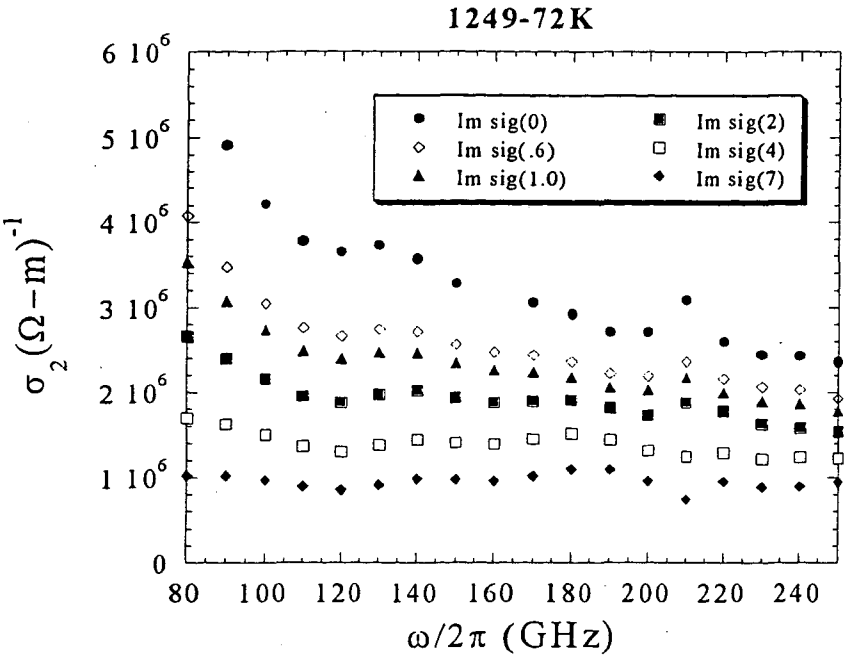
1249-72K
Im sig(0)
Im sig(.6)
Im sig(1.0)
Im sig(2)
Im sig(4)
Im sig(7)
$\sigma_2(\Omega-m)^{-1}$
$\omega/2\pi$ (GHz)

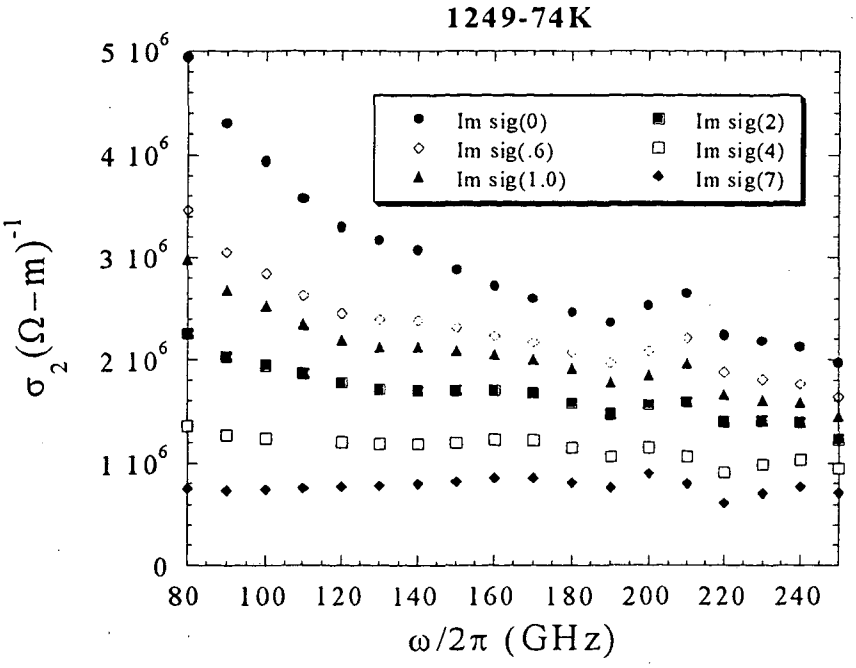
1249-74K
Im sig(0)
Im sig(.6)
Im sig(1.0)
Im sig(2)
Im sig(4)
Im sig(7)
$\sigma_2(\Omega-m)^{-1}$
$\omega/2\pi$ (GHz)

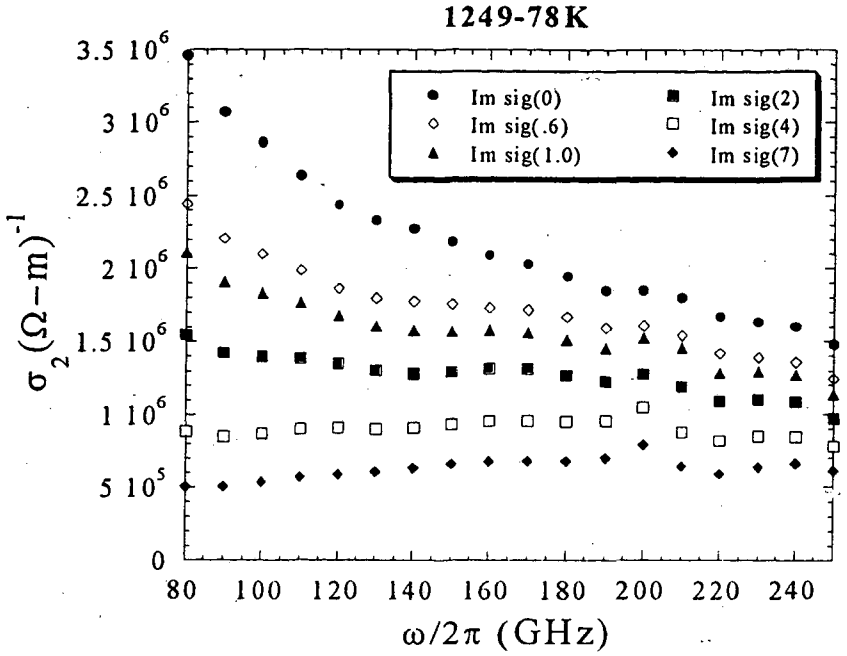
1249-78K
Im sig(0)
Im sig(.6)
Im sig(1.0)
Im sig(2)
Im sig(4)
Im sig(7)
σ2 (Ω−m)-1
3.5 10^6
3 10^6
2.5 10^6
2 10^6
1.5 10^6
1 10^6
5 10^5
0
80 100 120 140 160 180 200 220 240
ω/2π (GHz)

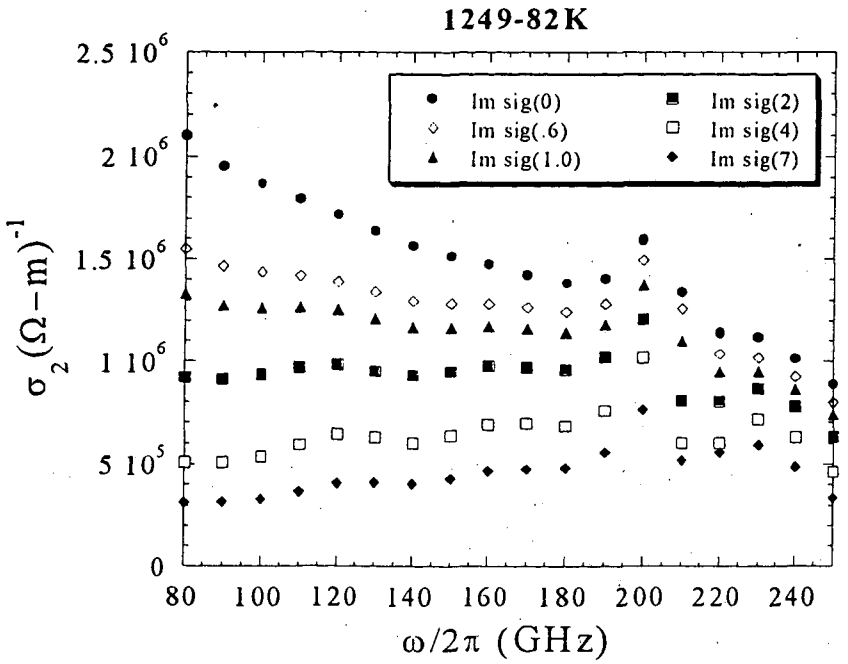
1249-82K
Im sig(0)
Im sig(.6)
Im sig(1.0)
Im sig(2)
Im sig(4)
Im sig(7)
σ2 (Ω−m)-1
2.5 10^6
2 10^6
1.5 10^6
1 10^6
5 10^5
0
80 100 120 140 160 180 200 220 240
ω/2π (GHz)

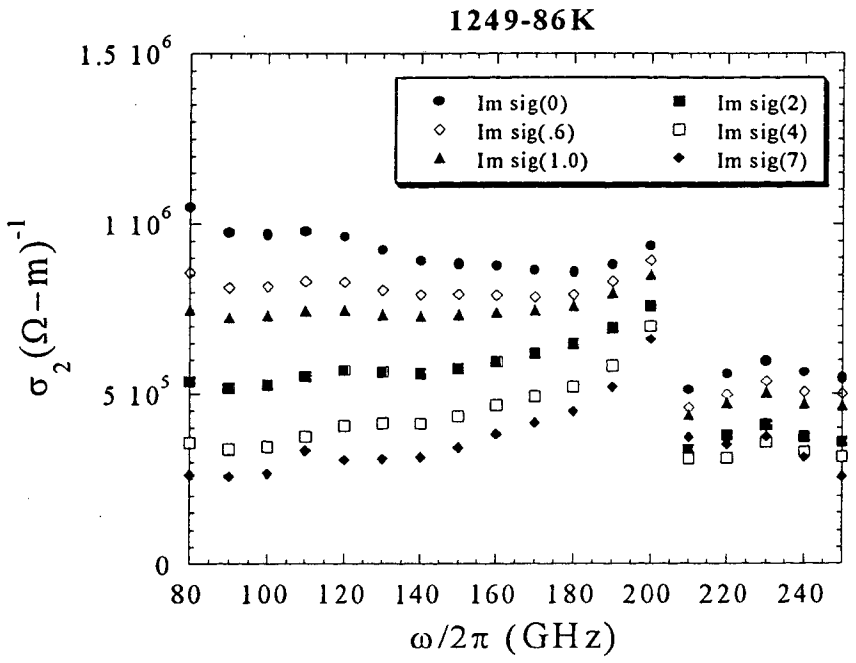
1249-86K
1.5 10^6
1 10^6
5 10^5
0
σ2(Ω−m)^-1
Im sig(0)
Im sig(.6)
Im sig(1.0)
Im sig(2)
Im sig(4)
Im sig(7)
80 100 120 140 160 180 200 220 240
ω/2π (GHz)

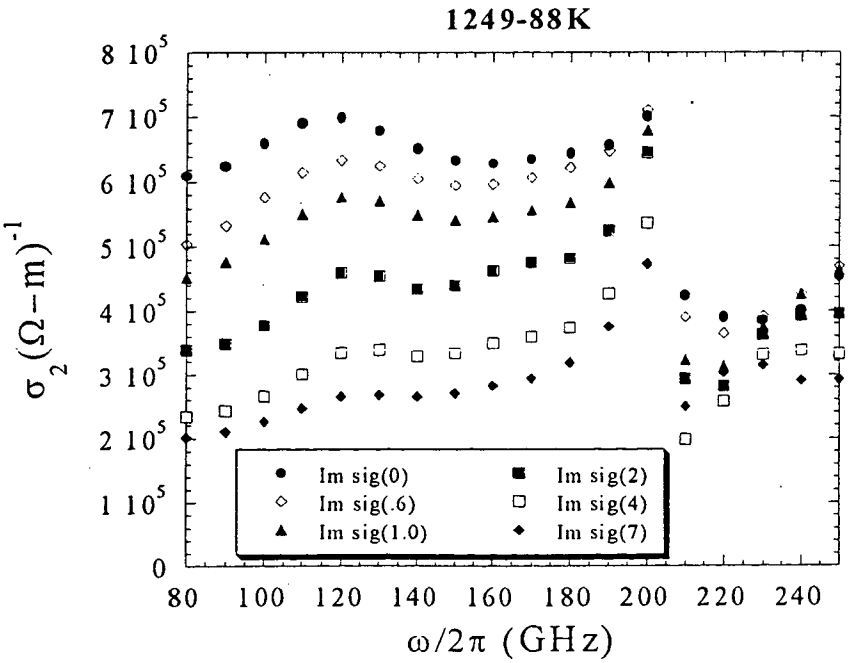
1249-88K
8 10^5
7 10^5
6 10^5
5 10^5
4 10^5
3 10^5
2 10^5
1 10^5
0
σ2(Ω−m)^-1
Im sig(0)
Im sig(.6)
Im sig(1.0)
Im sig(2)
Im sig(4)
Im sig(7)
80 100 120 140 160 180 200 220 240
ω/2π (GHz)

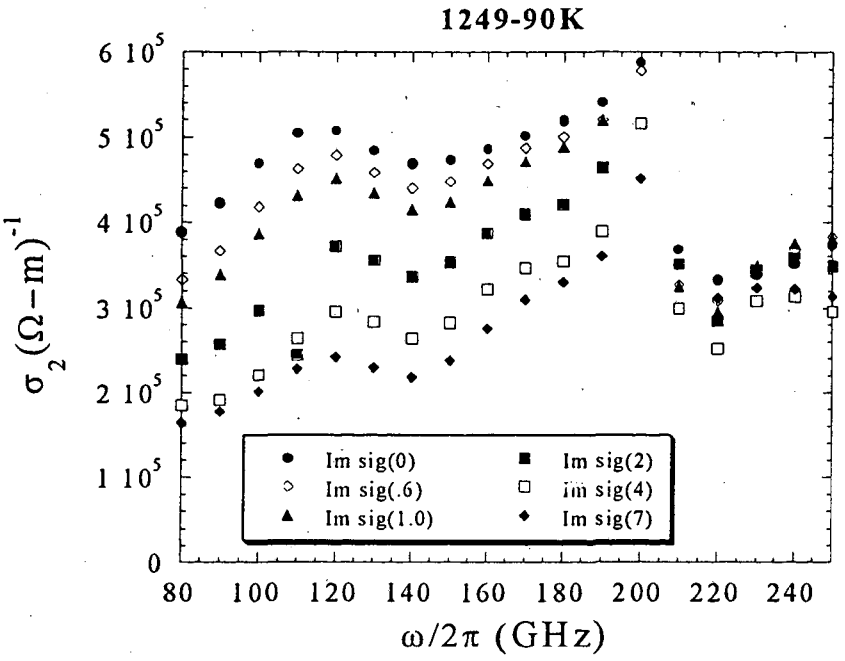
1249-90K
6 10^5
5 10^5
4 10^5
3 10^5
2 10^5
1 10^5
0
σ2 (Ω−m)^-1
80 100 120 140 160 180 200 220 240
ω/2π (GHz)
Im sig(0)
Im sig(.6)
Im sig(1.0)
Im sig(2)
Im sig(4)
Im sig(7)

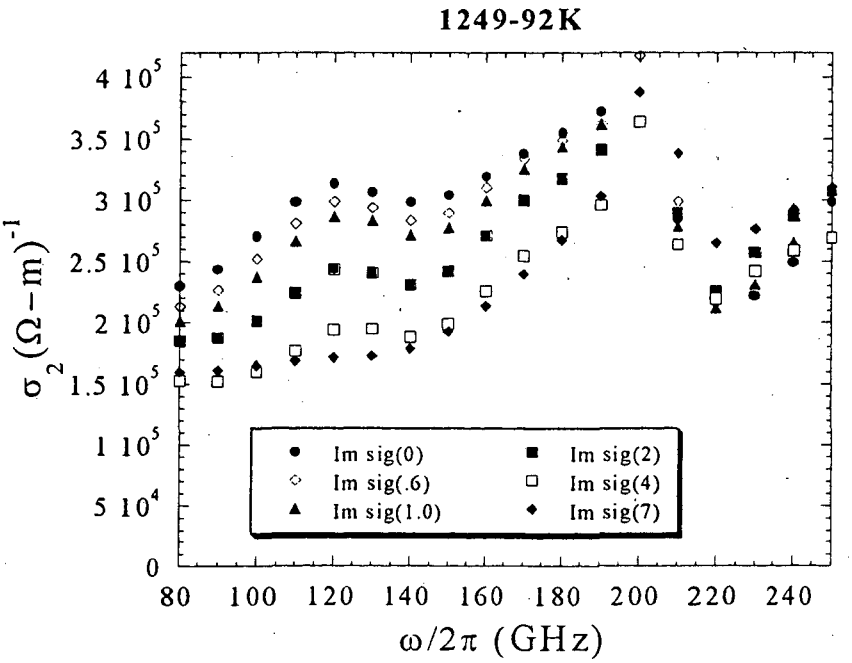
1249-92K
4 10^5
3.5 10^5
3 10^5
2.5 10^5
2 10^5
1.5 10^5
1 10^5
5 10^4
0
σ2 (Ω−m)^-1
80 100 120 140 160 180 200 220 240
ω/2π (GHz)
Im sig(0)
Im sig(.6)
Im sig(1.0)
Im sig(2)
Im sig(4)
Im sig(7)

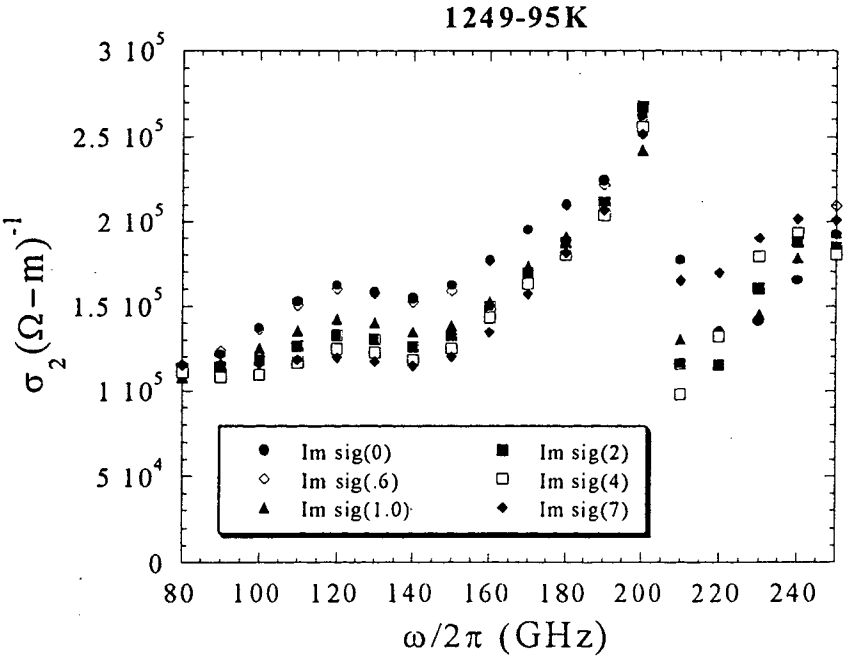
1249-95K
3 10^5
2.5 10^5
2 10^5
1.5 10^5
1 10^5
5 10^4
0
σ2 (Ω-m)^-1
80
100
120
140
160
180
200
220
240
ω/2π (GHz)
Im sig(0)
Im sig(.6)
Im sig(1.0)
Im sig(2)
Im sig(4)
Im sig(7)

C.3.3 σ vs. H

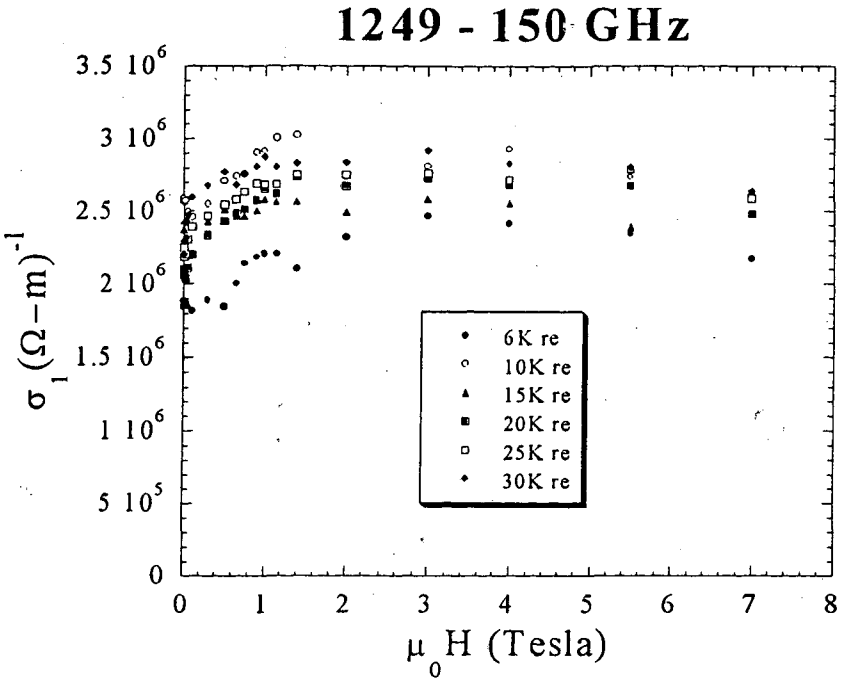

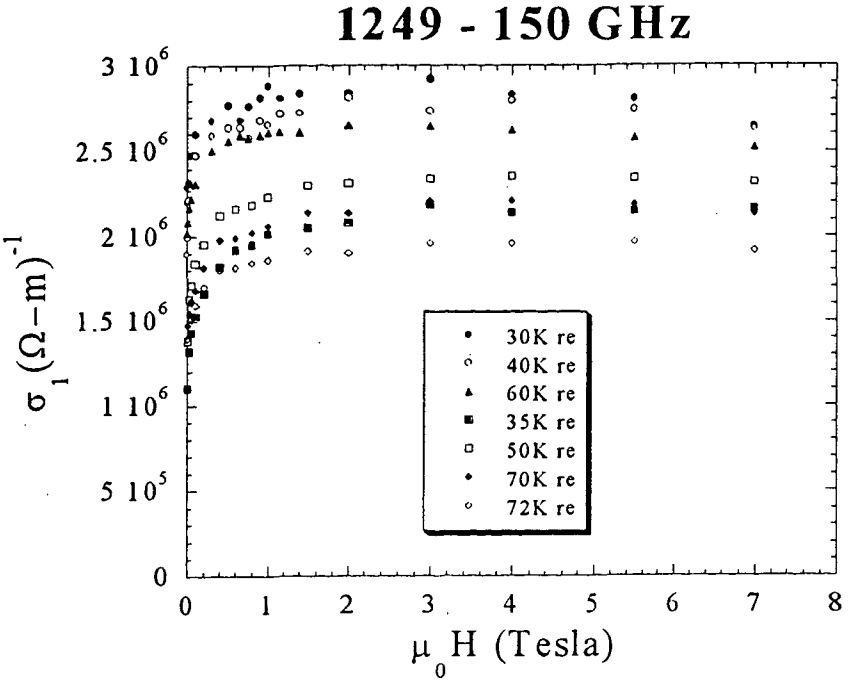
1249 - 150 GHz
3 10^6
2.5 10^6
2 10^6
1.5 10^6
1 10^6
5 10^5
0
σ1 (Ω-m)^-1
0
1
2
3
4
5
6
7
8
μ0 H (Tesla)
30K re
40K re
60K re
35K re
50K re
70K re
72K re

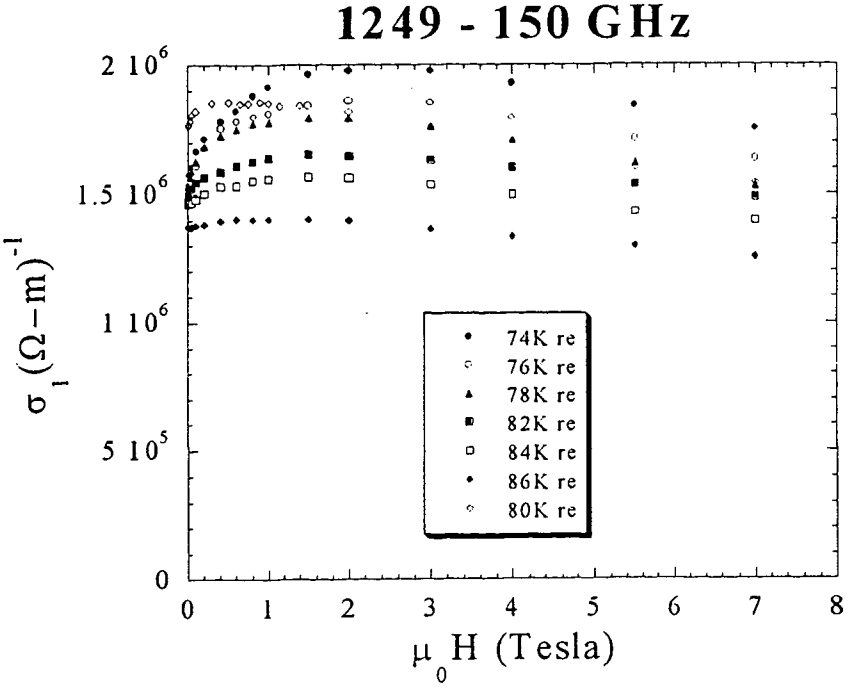
1249 - 150 GHz
2 10^6
1.5 10^6
1 10^6
5 10^5
0
σ1 (Ω-m)^-1
0
1
2
3
4
5
6
7
8
μ0 H (Tesla)
74K re
76K re
78K re
82K re
84K re
86K re
80K re

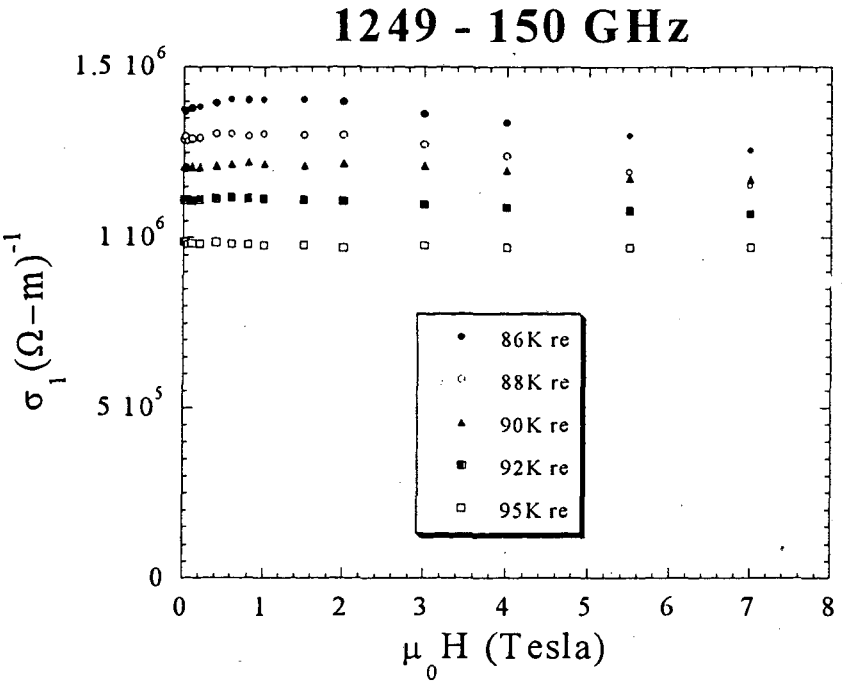
1249 - 150 GHz
1.5 10^6
1 10^6
5 10^5
0
σ1 (Ω-m)^-1
0
1
2
3
4
5
6
7
8
μ0 H (Tesla)
86K re
88K re
90K re
92K re
95K re

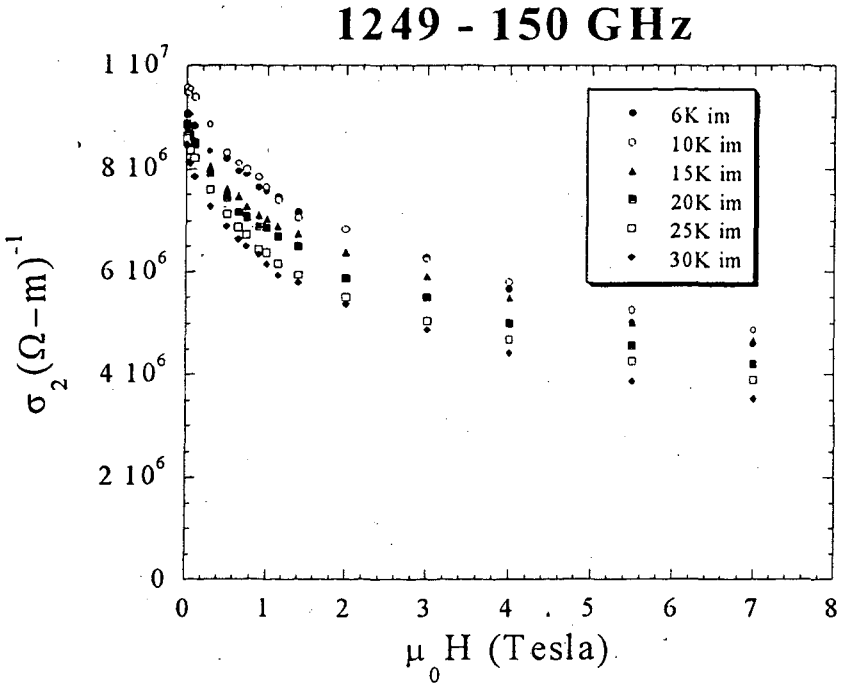
1249 - 150 GHz
1 10^7
8 10^6
6 10^6
4 10^6
2 10^6
0
σ2 (Ω-m)^-1
0
1
2
3
4
5
6
7
8
μ0 H (Tesla)
6K im
10K im
15K im
20K im
25K im
30K im

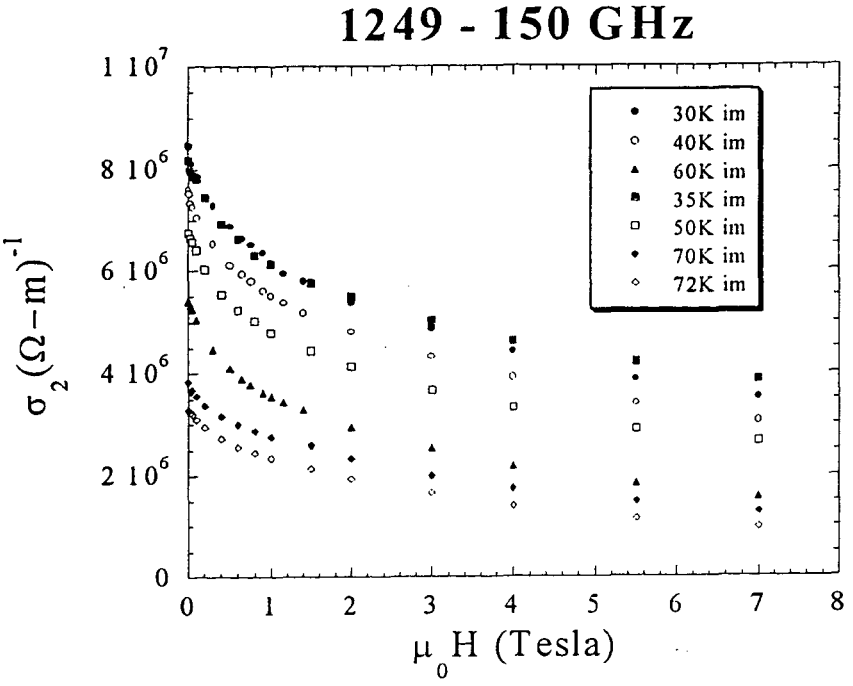
1249 - 150 GHz
1 10^7
8 10^6
6 10^6
4 10^6
2 10^6
0
σ2 (Ω−m)^-1
0 1 2 3 4 5 6 7 8
μ0 H (Tesla)
30K im
40K im
60K im
35K im
50K im
70K im
72K im

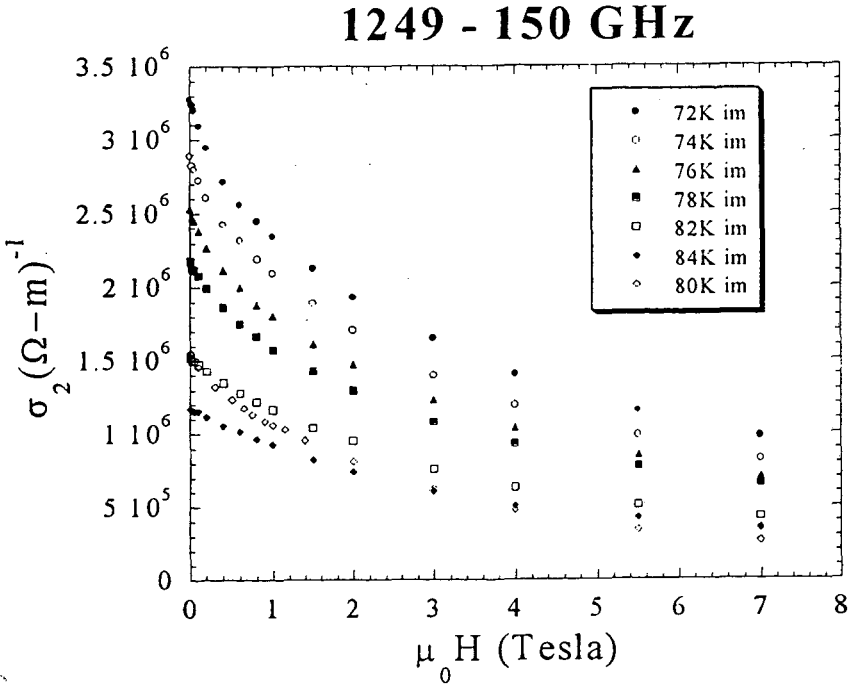
1249 - 150 GHz
3.5 10^6
3 10^6
2.5 10^6
2 10^6
1.5 10^6
1 10^6
5 10^5
0
σ2 (Ω−m)^-1
0 1 2 3 4 5 6 7 8
μ0 H (Tesla)
72K im
74K im
76K im
78K im
82K im
84K im
80K im

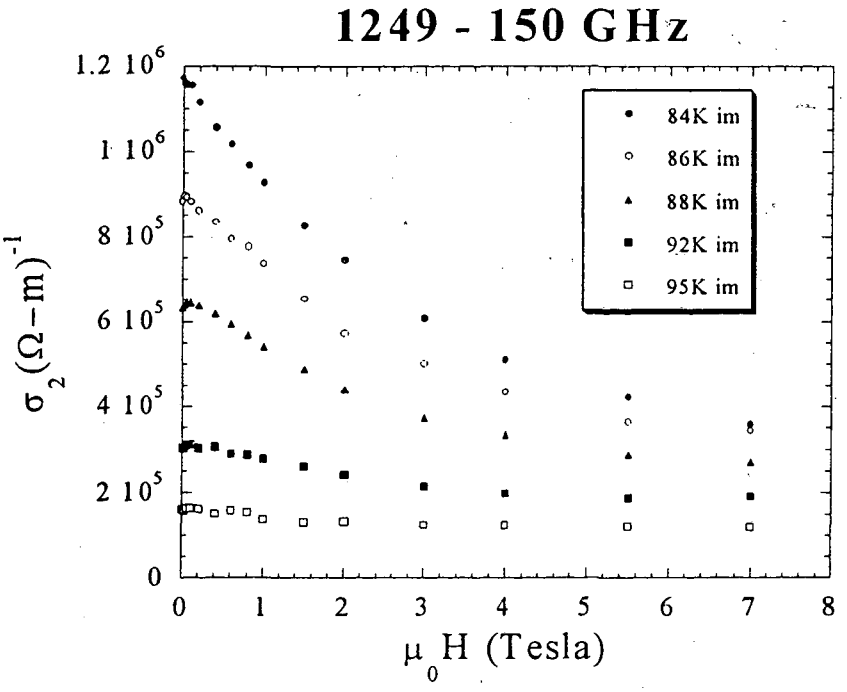
1249 - 150 GHz
1.2 10^6
1 10^6
8 10^5
6 10^5
4 10^5
2 10^5
0
σ2 (Ω-m)^-1
0
1
2
3
4
5
6
7
8
μ0 H (Tesla)
84K im
86K im
88K im
92K im
95K im

C.3.4 $\Delta\sigma$ vs. H

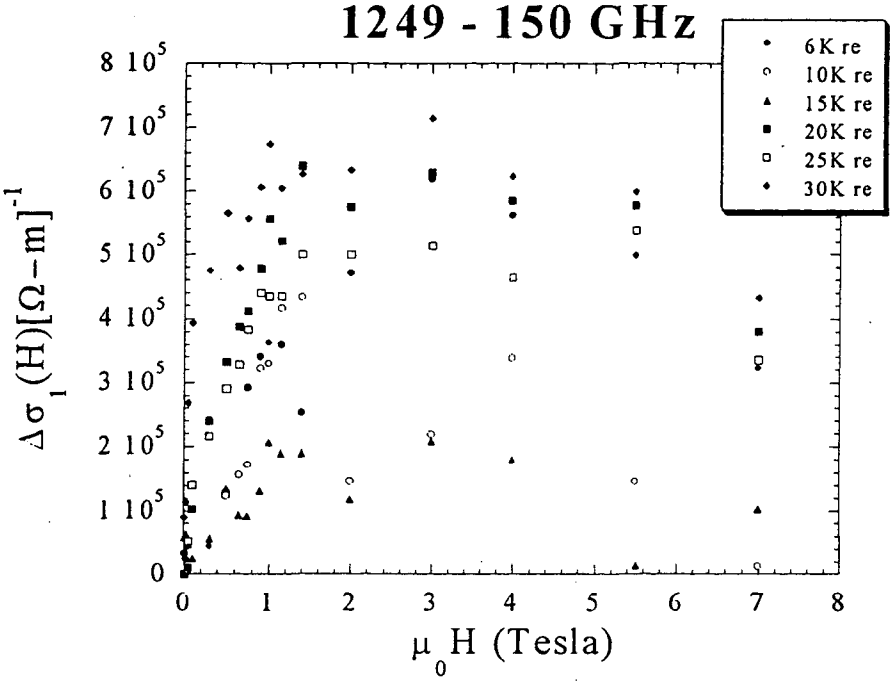

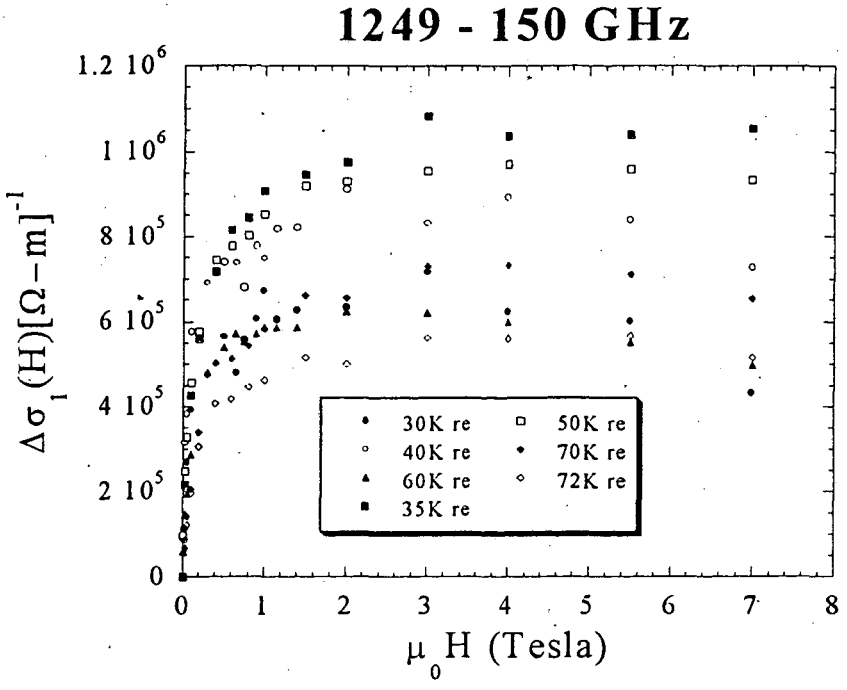
1249 - 150 GHz
1.2 10^6
1 10^6
8 10^5
6 10^5
4 10^5
2 10^5
0
Δσ1(H)[Ω−m]^-1
0
1
2
3
4
5
6
7
8
μ0H (Tesla)
30K re
40K re
60K re
35K re
50K re
70K re
72K re

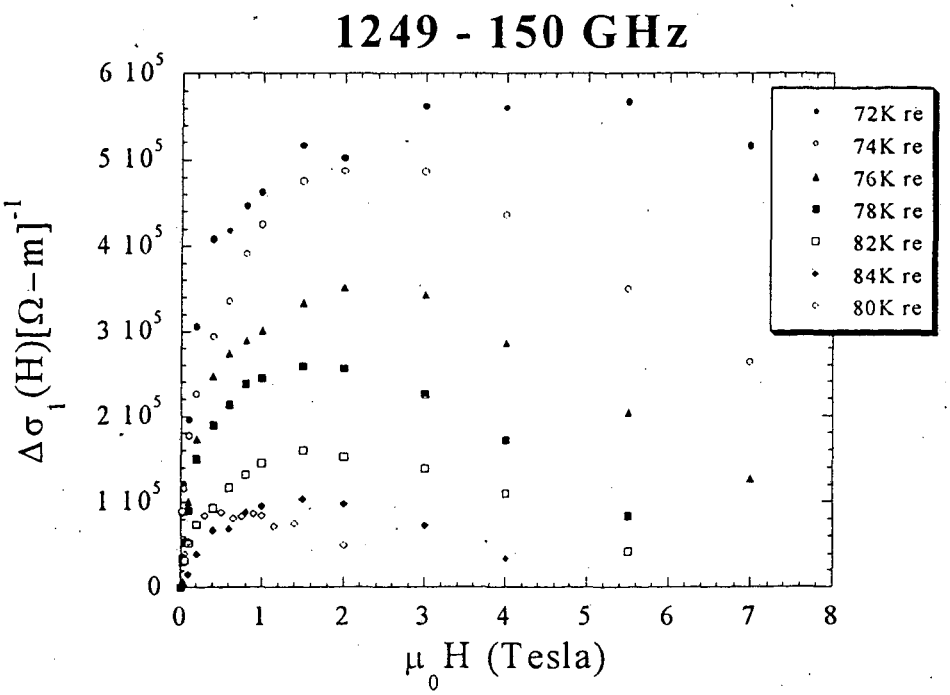
1249 - 150 GHz
6 10^5
5 10^5
4 10^5
3 10^5
2 10^5
1 10^5
0
Δσ1(H)[Ω−m]^-1
0
1
2
3
4
5
6
7
8
μ0H (Tesla)
72K re
74K re
76K re
78K re
82K re
84K re
80K re

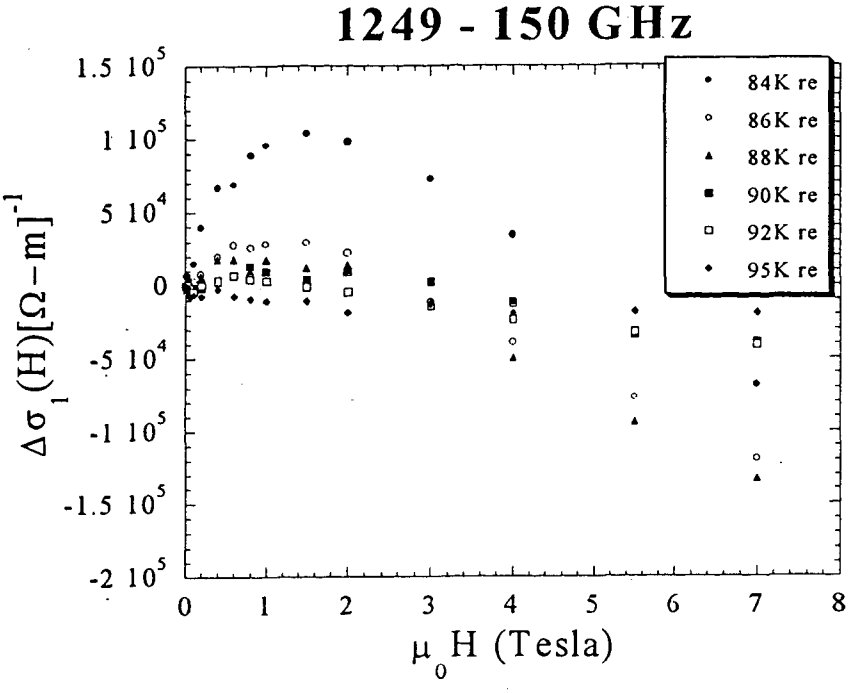
1249 - 150 GHz
1.5 10^5
1 10^5
5 10^4
0
-5 10^4
-1 10^5
-1.5 10^5
-2 10^5
Δσ_1(H)[Ω-m]^-1
0
1
2
3
4
5
6
7
8
μ_0H (Tesla)
84K re
86K re
88K re
90K re
92K re
95K re

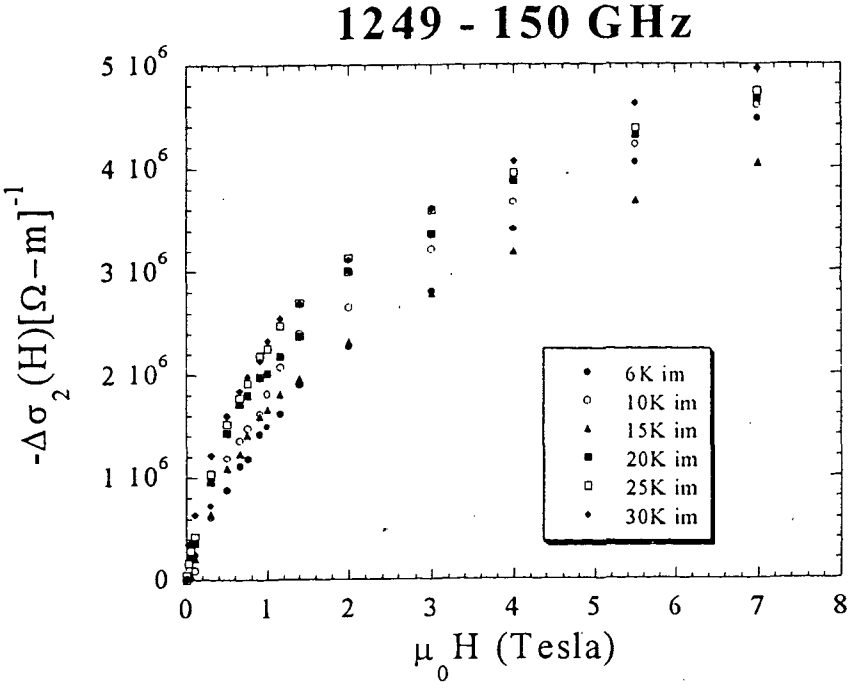
1249 - 150 GHz
5 10^6
4 10^6
3 10^6
2 10^6
1 10^6
0
-Δσ_2(H)[Ω-m]^-1
0
1
2
3
4
5
6
7
8
μ_0H (Tesla)
6K im
10K im
15K im
20K im
25K im
30K im

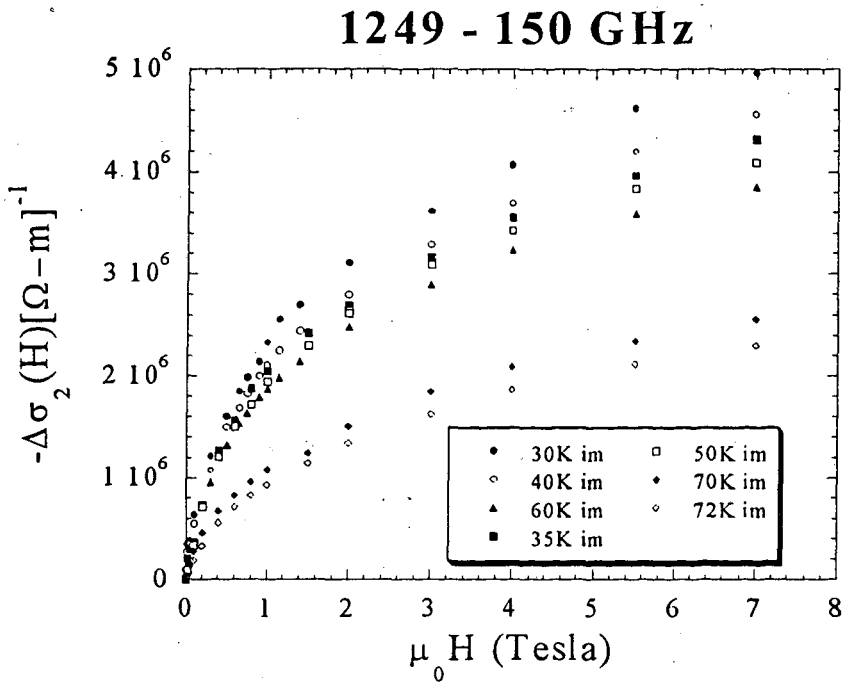
1249 - 150 GHz
5 10^6
4 10^6
3 10^6
2 10^6
1 10^6
0
-Δσ2(H)[Ω-m]^-1
0
1
2
3
4
5
6
7
8
μ0H (Tesla)
30K im
40K im
60K im
35K im
50K im
70K im
72K im

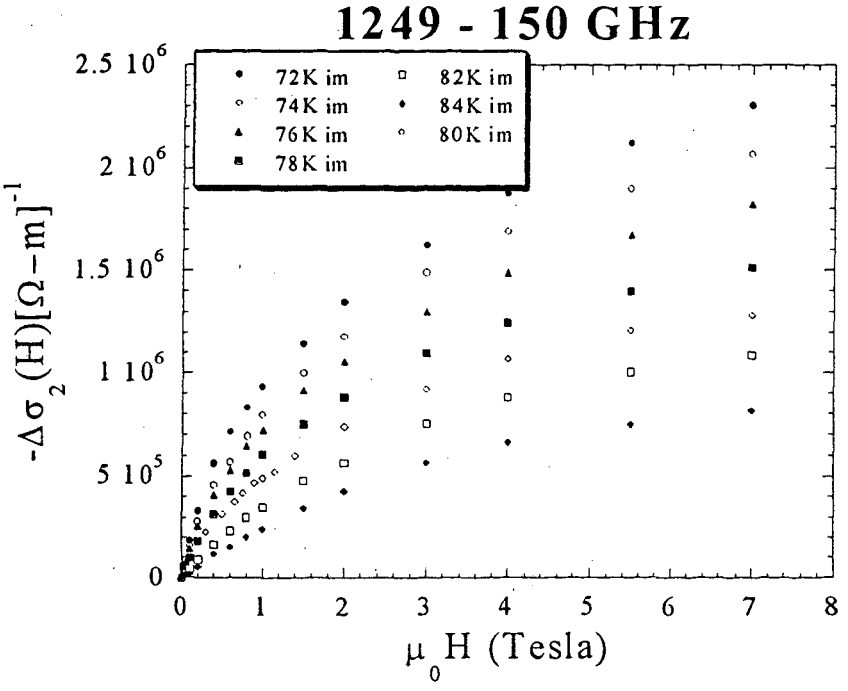
1249 - 150 GHz
2.5 10^6
2 10^6
1.5 10^6
1 10^6
5 10^5
0
-Δσ2(H)[Ω-m]^-1
0
1
2
3
4
5
6
7
8
μ0H (Tesla)
72K im
74K im
76K im
78K im
82K im
84K im
80K im

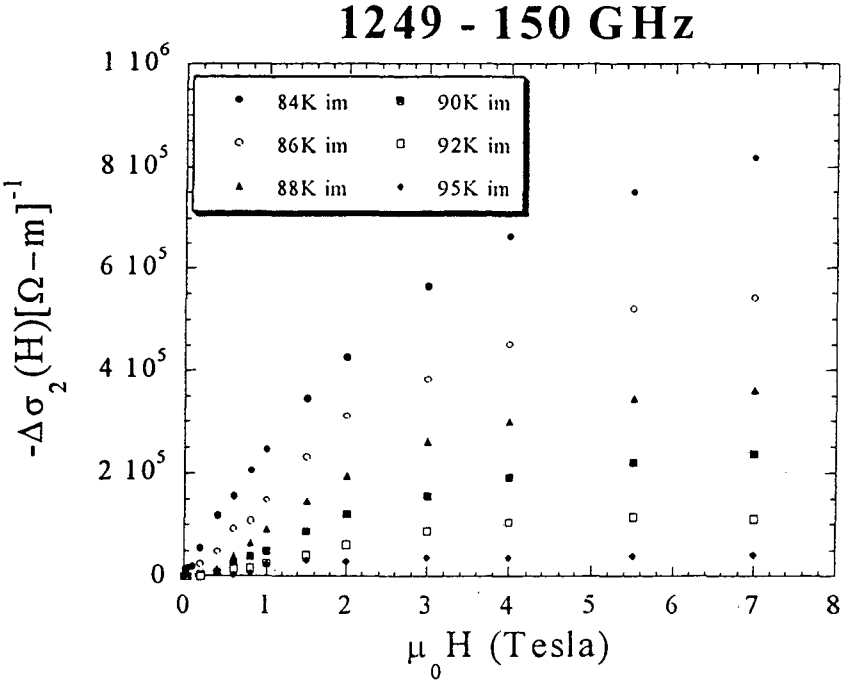
1249 - 150 GHz
84K im
86K im
88K im
90K im
92K im
95K im
$-\Delta\sigma_2(H)[\Omega-m]^{-1}$
$\mu_0 H$ (Tesla)
0
2 10^5
4 10^5
6 10^5
8 10^5
1 10^6
0
1
2
3
4
5
6
7
8

Ernest Orlando Lawrence Berkeley National Laboratory
One Cyclotron Road | Berkeley, California 94720

Prepared for the U.S. Department of Energy under Contract No. DE-AC03-76SF00098